

**CHEMICAL VAPOR DEPOSITION AND CHARACTERIZATION OF  
ZIRCONIA FILMS FOR HIGH-K DIELECTRIC APPLICATIONS**

by

Zhe Song

Dissertation

Submitted to the Faculty of the  
Graduate School of Vanderbilt University  
in partial fulfillment of the requirements  
for the degree of

**DOCTOR OF PHILOSOPHY**

in

Chemical Engineering

May, 2005

Nashville, Tennessee

Approved:

Prof. Bridget R. Rogers

Prof. M. Douglas LeVan

Prof. John A. Roth

Prof. G. Kane Jennings

Prof. David M. Hercules

Pro. Timothy P. Hanusa

Prof. Robert A. Weller

Dedicated

To

My Parents

Zhifeng Song and Junju Yuan

## ACKNOWLEDGEMENT

I would first like to thank my dissertation advisor, Dr. Bridget R. Rogers for her direction, support, patience, and friendship. I am lucky to be her first PhD student. I have learned a lot beyond my research projects. I wish her all the best in her future career.

I am grateful to my outstanding dissertation committee chaired by Dr. Bridget R. Rogers consisting of Dr. M. Douglas LeVan, Dr. John A. Roth, Dr. G. Kane Jennings, Dr. David M. Hercules, Dr. Timothy P. Hanusa, and Dr. Robert A. Waller. When I needed their help Dr. G. Kane Jennings, Dr. David M. Hercules and Dr. Timothy P. Hanusa were very gracious in allowing me to use equipment in their labs, and helped me set up collaborations with their students to investigate details.

I am grateful to my collaborators in industry, Dr. N. David Theodore, Dr. Michael L. Kottke, and Dr. Stefan Zollner at Freescale Semiconductor, Inc., and Dr. Paul Mack and Dr. Bill Chauvin at Thermo Electron, Co. I am very grateful for their spending time to help me in addition to their already very busy day-to-day schedule.

I would like to thank the faculty and staff in the Department of Chemical Engineering at Vanderbilt University for teaching, training, help, and support. Mr. Mark Holmes provided much assistance in setting up our laboratory. I would like to thank Dr. Charles M. Lukehart for allowing me to use the XRD, Dr. Leonard C. Feldman for allowing me to access the AFM, and Dr. James E. Wittig for allowing me to use the SEM.

I would like to thank my fellow graduate students and undergraduate students, Robert D. Geil, Vivek D. Pawar, Virginia Wahlig, Christy A. Hales, for their

collaboration and support. I'd like to thank Matthew J. Vergne, Lisa M. Sullivan, Yang Fu, Lacey S. Fitts, for teaching me to use XPS, XRD, SEM and TEM, and helping me run chemical experiments in a dry box. I thank Wenfeng Guo for her suggestions and support through the years at Vanderbilt University.

In addition, I am grateful for the financial support from National Science Foundation (# CTS-0092792).

Finally, I would like to thank my parents Zhifeng Song and Junju Yuan for their unconditional love and support. They have been the source of my strength and persistence.

## TABLE OF CONTENTS

	Page
DEDICATION .....	ii
ACKNOWLEDGMENT.....	iii
LIST OF TABLES .....	viii
LIST OF FIGURES .....	ix
Chapter	
I. INTRODUCTION .....	1
II. BACKGROUND .....	6
2.1 HIGH-K MATERIAL PROPERTY REQUIREMENTS .....	6
2.1.1 Dielectric Constant and Band Offsets.....	6
2.1.2 Thermal Stability .....	9
2.1.3 Interfacial Quality .....	11
2.1.4 Morphology.....	13
2.2 ZRO <sub>2</sub> PROPERTIES AND DEPOSITION .....	15
2.2.1 Outline of ZrO <sub>2</sub> Properties .....	15
2.2.2 Outline of Challenges in Deposition Processes .....	16
2.2.3 Atomic Layer Chemical Vapor Deposition (ALCVD) .....	18
2.2.4 Molecular Beam Epitaxy (MBE) .....	24
2.2.5 Metal Organic Chemical Vapor Deposition (MOCVD) .....	26
III. SPECTROSCOPIC ELLIPSOMETRY CHARACTERIZATION OF ZIRCONIA FILMS ON SI(100) DEPOSITED BY HV-CVD.....	31
3.1 BACKGROUND .....	31
3.2 EXPERIMENTAL DETAILS .....	33

3.2.1	High Vacuum Chemical Vapor Deposition System .....	33
3.2.2	Sample Preparation .....	34
3.2.3	Ex-situ Spectroscopic Ellipsometry (SE).....	35
3.2.4	Film Topology .....	37
3.2.5	Transmission Electron Microscopy (TEM) .....	37
3.3	AFM AND TEM RESULTS .....	37
3.4	ELLIPSOMETRY DATA ANALYSIS RESULTS .....	40
3.4.1	Data of Silicon Oxide to Simulate the Interfacial Layers .....	43
3.4.2	The EMA Model to Simulate the Interfacial Layers .....	44
3.4.3	Dispersion Models to Simulate the Interfacial Layers.....	48
3.5	DISCUSSION.....	50
3.6	CONCLUSIONS.....	56
<b>IV.</b>	<b>IN-SITU ELLIPSOMETRY STUDY OF THE INITIAL STAGE DEPOSITION OF ZIRCONIA ON DIFFERENT SURFACES .....</b>	<b>58</b>
4.1	BACKGROUND .....	58
4.2	EXPERIMENTAL DETAILS .....	60
4.3	RESULTS AND DISCUSSION .....	61
4.3.1	XRD Results of 200 Å Samples.....	62
4.3.2	Film Topology .....	64
4.3.3	Extraction of Refractive Indexes of $ZrO_2$ .....	67
4.3.4	SE Modeling of the Initial-stage Deposition of $ZrO_2$ .....	73
4.3.4.1	Two-layer SE Model (Model B).....	73
4.3.4.2	One-layer SE Model (Model C).....	78
4.3.5	Initial-stage Deposition Profile and Void Fraction Evolution .....	79
4.4	A DISCUSSION ON THE INITIAL-STAGE DEPOSITION OF $ZrO_2$ .....	83
4.4.1	Initial-stage Deposition of $ZrO_2$ on H-Si .....	83
4.4.2	Initial-stage Deposition of $ZrO_2$ on Native Silicon Oxide Surfaces.....	86
4.5	CONCLUSIONS.....	88

V.	INITIAL-STAGE DEPOSITION OF ZRO <sub>2</sub> ON H-TERMINATED SI(100) AND NATIVE SILICON OXIDE SURFACES .....	90
5.1	BACKGROUND .....	90
5.2	EXPERIMENTAL DETAILS .....	91
5.3	RESULTS .....	94
5.3.1	In-situ SE .....	94
5.3.2	AFM.....	96
5.3.3	TEM .....	99
5.3.4	ToF MEBS .....	103
5.3.5	ARXPS.....	105
5.3.6	Ex-situ SE .....	111
5.4	DISCUSSION .....	113
5.4.1	Nucleation and Coalescence on H-Si Surfaces .....	114
5.4.2	Nucleation and Coalescence on Native Silicon Oxide Surfaces.....	115
5.4.3	Formation of the Interfacial Layer.....	117
5.4.4	Discussion of Characterization Methods .....	119
5.5	CONCLUSIONS.....	121
VI.	CONLCUSIONS AND RECOMMENDATIONS .....	122
	REFERNCES.....	127

## LIST OF TABLES

Table	Page
1      The scaling of MOSFET devices.....	4
2      Combined thickness results from AFM and TEM.....	40
3      Extracted optical constant parameters for the interfacial layer and the ZrO <sub>2</sub> layer by using dispersion model to simulate the interfacial layer.....	51
4      Thicknesses of some samples measured by different methods.....	98
5      Atomic concentration of elements at different chemical states .....	111

## LIST OF FIGURES

Figure	Page
1. MOSFET structure.....	2
2. The band diagram for MIS diodes for n-type and p-type silicon substrate .....	7
3. Plot of the optical band gaps and dielectric constants of some potential high-k gate dielectric materials.....	9
4. A schematic of high vacuum chemical vapor deposition system .....	34
5. Average refractive indexes and standard deviations of ZrO <sub>2</sub> samples deposited at different temperatures.....	36
6. A 2.5 μm × 2.5 μm top view AFM image of Sample S07-07 .....	39
7. The definitions of RMS and the surface roughness layer thickness .....	39
8. Cross sectional TEM images of Sample S07-08 at different magnifications .....	40
9. Models for MS-VASE data analysis.....	41
10. The extracted optical constants of the ZrO <sub>2</sub> layer when silicon oxides were used to simulate the interfacial layer.....	45
11. SE thickness results compared with AFM-TEM results, when SiO <sub>x</sub> , SiO <sub>2</sub> , NO-1, and NO-2 were used to simulate the interfacial layer.....	46
12. The optical constants of the interfacial layer extracted from different EMA models .....	47
13. The extracted optical constants of ZrO <sub>2</sub> layer when different EMA layers were used to simulate the interfacial layer .....	48
14. SE thickness results compared with AFM-TEM results, when EMA(Si-ZrO <sub>2</sub> ), EMA(SiO <sub>x</sub> -ZrO <sub>2</sub> ), and EMA(SiO <sub>2</sub> -ZrO <sub>2</sub> ) were used to simulate the interfacial layer.....	47
15. The optical constants of ZrO <sub>2</sub> when dispersion models were used to simulate the interfacial layer.....	51
16. The optical constants of the interfacial layer extracted from different dispersion models.....	52

17.	SE thickness results compared with AFM-TEM results, when TL, single Lorentz oscillator, dual Lorentz oscillator, and the Sellmeier model were used to simulate the interfacial layer.....	52
18.	X-ray diffraction spectra of 200 Å ZrO <sub>2</sub> deposited on H-Si .....	62
19.	X-ray diffraction pattern of 200 Å ZrO <sub>2</sub> deposited on native silicon oxide .....	63
20.	2μm × 2μm AFM images of 30 Å and 60 Å ZrO <sub>2</sub> films deposited on H-Si surfaces at 350 °C.....	65
21.	Surface roughness of ZrO <sub>2</sub> films deposited on different surfaces and at different temperatures and thicknesses .....	65
22.	2μm × 2μm AFM images of 15 Å, 30 Å, 50 Å, and 100 Å ZrO <sub>2</sub> films deposited on native silicon oxide at 300 °C.....	66
23.	Surface roughness measured by AFM and void fractions measured by spectroscopic ellipsometry of ZrO <sub>2</sub> films deposited on native silicon oxide surfaces at 300 °C and different thicknesses .....	67
24.	A schematics of deposition stages .....	68
25.	Spectroscopic ellipsometry models for data analysis .....	70
26.	The refractive indexes of ZrO <sub>2</sub> films deposited on native silicon oxide and hydrogen terminated silicon surfaces at different temperatures extracted by the Tauc-Lorentz model .....	70
27.	Two-layer model static mode data analysis results.....	72
28.	Optical constant of ZrO <sub>2</sub> .....	73
29.	Thickness-time profiles of depositions on native silicon oxide surfaces at different temperatures .....	74
30.	Thickness-time profiles of depositions on H-Si surfaces at different temperatures .....	75
31.	Thickness-time profile of ZrO <sub>2</sub> initial-stage deposition on H-Si surfaces.....	80
32.	Thickness-time profiles of initial stage ZrO <sub>2</sub> deposition on native silicon oxide surfaces.....	80
33.	Void fraction evolution during initial-stage deposition .....	81
34.	A schematic of the film formation mechanism of ZrO <sub>2</sub> on H-Si surfaces.....	85

35.	A schematic of the film formation mechanism of ZrO <sub>2</sub> on native silicon oxide surfaces.....	87
36.	Void fraction evolution during ZrO <sub>2</sub> initial-stage deposition on H-Si surfaces .....	95
37.	Void fraction evolution during ZrO <sub>2</sub> initial-stage deposition on native silicon oxide surfaces.....	96
38.	2μm × 2μm AFM images 30 Å and 60 Å ZrO <sub>2</sub> films deposited at 350 °C on H-Si surfaces and native silicon oxide surfaces .....	97
39.	The surface roughness of 30 and 60 Å ZrO <sub>2</sub> films deposited on H-Si and native silicon oxide surfaces .....	98
40.	Cross sectional TEM images of 30 Å ZrO <sub>2</sub> films deposited at 350 °C and 450 °C on H-Si surfaces and native silicon oxide surfaces.....	100
41.	Plan view TEM images of 30 Å ZrO <sub>2</sub> films deposited at 350 °C and 450 °C on H-Si surfaces and native silicon oxide surfaces .....	101
42.	Plan view TEM images of 60 Å ZrO <sub>2</sub> films deposited at 350 °C and 450 °C on H-Si surfaces and native silicon oxide surfaces .....	102
43.	TOF-MEBS backscattering spectra of 30 Å ZrO <sub>2</sub> deposited at 450 °C on native silicon oxide and H-Si .....	103
44.	TOF-MEBS He <sup>+</sup> backscattering spectrum and simulation of 30 Å ZrO <sub>2</sub> deposited on native silicon oxide at 450° C. The solid line shows the simulation.....	104
45.	Interfacial layer zirconium atomic ratio of 30 and 60 Å ZrO <sub>2</sub> films deposited on H-Si and native silicon oxide surfaces at different temperatures .....	105
46.	ARXPS of Zr 3d, O 1s, and Si 2p spectra of 30 Å ZrO <sub>2</sub> deposited on H-Si surfaces at 350 °C .....	107
47.	ARXPS of Zr 3d, O 1s, and Si 2p spectra of 30 Å ZrO <sub>2</sub> deposited on native silicon oxide surfaces at 350 °C .....	108
48.	Elemental depth profile of a 30 Å ZrO <sub>2</sub> film deposited on H-Si surfaces at 350 °C .....	109
49.	Elemental depth profile of a 30 Å ZrO <sub>2</sub> film deposited on native silicon oxide surfaces at 350 °C .....	110

50. Ex-situ SE results of surface roughness layer, ZrO <sub>2</sub> layer, and interfacial layer thicknesses of 30 and 60 Å ZrO <sub>2</sub> samples deposited on different surfaces and at different temperatures .....	112
--	-----

## CHAPTER I

### INTRODUCTION

In contrast to the historically unprecedented progress in productivity and performance in the semiconductor industry, the basic device structure of integrated circuits (ICs), the metal-oxide-semiconductor-field-effect-transistor (MOSFET), has changed very little since it became the predominant design in the 1970s<sup>1</sup>. In the last three decades, the primary attention was put on gate length scaling, so dynamic-random-access-memory (DRAM) half pitch was used to name technology generations. The progress of the semiconductor industry to move from one technology generation to another was primarily based on the development of new lithography tools, masks, photoresist materials, and critical dimension etch processes<sup>2</sup>.

Continued scaling requires the introduction of new materials to sustain further progress. In the past few years people have identified more challenges due to the physical limits of materials used to fabricate MOSFET devices<sup>3</sup>. The semiconductor industry has entered “the era of material limited device scaling”<sup>3</sup>. Various designs and plans to substitute the current materials used in ICs have been proposed, such as low-k dielectrics<sup>4</sup>, high-k dielectrics<sup>5</sup>, carbon nanotubes<sup>6,7</sup>, and various modified MOSFET structures<sup>8</sup>.

Figure 1 shows the basic structure of a n-channel MOSFET transistor. The base of the device is p-type silicon. Two n<sup>+</sup> areas, the source and the drain, are formed by adding donor atoms, such as phosphorus, into the silicon lattice. Above the silicon substrate between the source and drain is a thin silicon dioxide layer called the gate dielectric layer.

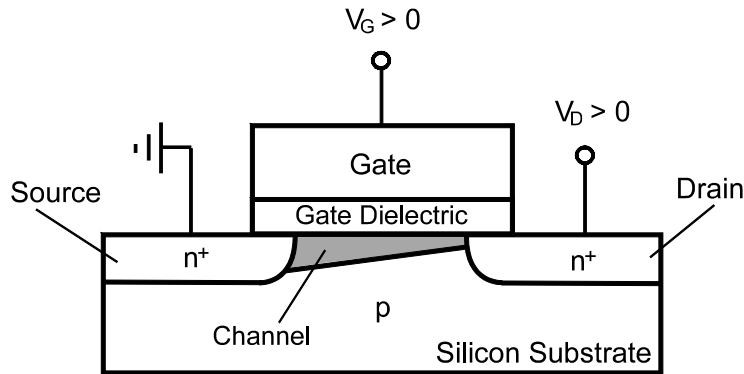


Figure 1: MOSFET structure

The conductive gate on the top of the silicon dioxide layer completes the structure.

MOSFET transistors act as switches in ICs, turning on and off the current between the drain and the source. A potential difference is applied between the drain and the source ( $V_{DS}$ ). When the gate voltage ( $V_G$ ) is lower than the threshold voltage ( $V_t$ ) of the MOSFET device, the potential drop  $V_{DS}$  is held by the pn junctions between the source and the substrate. No current can flow from the drain to the source, and the MOSFET device is in the off condition. When  $V_G$  is larger than the threshold voltage of the device, a potential drop is sustained across the silicon dioxide layer. Holes under the gate dielectric are pushed away, creating a conductive inversion layer of electrons underneath the silicon dioxide. This conductive layer is called the channel. Current can flow from the drain through this conductive channel to the source, and the MOSFET device is turned on.

The dimensions of the MOSFET have steadily been decreased to increase the degree of integration and promote functionality of the circuit. The constant-field scaling

method has been used widely as the rule for designing the scaled-down MOSFET devices<sup>1</sup>. Constant field scaling laws require the decrease of both the vertical and lateral dimensions of the devices by a factor  $\kappa$ , while increasing the doping concentration by the same factor  $\kappa$ . Table 1 summarizes the constant field scaling laws and their effects on device operations<sup>9</sup>. We can see that by scaling the dimensions of the MOSFET devices, the time to switch the MOSFET devices on or off (gate delay) is decreased by the same factor  $\kappa$ . Therefore, the calculation speed can be increased by a factor  $\kappa$ . At the same time, the lateral dimensions are decreased by  $\kappa$  times, so the surface area of MOSFET devices decreases by a factor of  $\kappa^2$ . More functionality can be integrated on the same surface area. MOSFET scaling well satisfied customer's demands on high-speed calculation and complex functionalities. Consequently, it has been the primary means for the semiconductor industry to move forward.

The semiconductor industry has been well known for its fast paced progress. Moore's law quantitatively predicted that the logic circuit density on a single chip and its performance would continue to double every two to three years, while the memory capacity would quadruple in the same period of time<sup>10</sup>. In order to keep pace with the Moore's law, the semiconductor industry has been aggressively making progresses in MOSFET scaling and technology development. The physical gate length of MOSFET devices has been decreased by more than 80 times from  $\sim 5\mu\text{m}$  in 1974<sup>1</sup> to  $\sim 60\text{ nm}$  in 2004<sup>11</sup>, while the gate dielectric layer thickness has been decreased from 100 nm in 1974<sup>1</sup> to 1.2 nm in 2004<sup>11</sup>. It needs to be pointed out that the 1.2 nm gate dielectric thickness is the equivalent physical gate dielectric layer thickness (EOT), which refers to the equivalent thickness of the gate dielectric layer if  $\text{SiO}_2$  is used.

Table 1.1: The scaling of MOSFET devices<sup>9</sup>

Scaling factors:	
Surface dimensions	1/ $\kappa$
Vertical dimensions	1/ $\kappa$
Doping concentration	$\kappa$
Influenced parameters:	
Currents, Voltages ( $V_G$ , $V_{DS}$ )	1/ $\kappa$
Current density	$\kappa$
Capacitance per unit area	$\kappa$
Gate delay	1/ $\kappa$
Power dissipation $I_{ds}D_{ds}$	1/ $\kappa^2$
Power-delay product	1/ $\kappa^3$

After decades of unabated efforts in device scaling, the semiconductor industry has pushed the gate silicon dioxide layer to its physical limit. Many research results have shown that using a silicon dioxide dielectric layer thinner than 1.5 nm will result in high tunneling currents from the gate to the substrate<sup>12-14</sup>. Low-level leakage current will directly increase power consumption. Moreover, if the leakage current is significant compared with the channel current, MOSFET devices cannot be turned on and off effectively, and hence will fail to function properly.

Research results have also shown that the leakage current increases exponentially with decreasing dielectric film thickness<sup>12,13</sup>. Therefore, using a thicker film is an effective method to block these leakage currents. At the same time, in order to maintain the gate capacitance across the dielectric films, a material of a higher dielectric constant than  $\text{SiO}_2$  needs to be used, as shown by

$$C_{ox} = \frac{\epsilon_0 k_{\text{SiO}_2}}{d_{\text{SiO}_2}} = \frac{\epsilon_0 k_{\text{high-}k}}{d_{\text{high-}k}} \quad (1.1)$$

It is widely accepted that high-k dielectric materials will be integrated into ICs in the near future<sup>5,12,15-17</sup>. Investigations of materials of higher  $k$  values, such as  $\text{Ta}_2\text{O}_5$ <sup>18</sup>,  $\text{TiO}_2$ <sup>19</sup>,

$\text{Y}_2\text{O}_3$ <sup>20</sup>,  $\text{Al}_2\text{O}_3$ <sup>21,22</sup>,  $\text{ZrO}_2$ <sup>20,23-25</sup>,  $\text{ZrSi}_x\text{O}_y$ <sup>26,27</sup>,  $\text{HfSi}_x\text{O}_y$ <sup>27,28</sup>, and  $\text{SrTiO}_3$ <sup>29</sup>, are currently underway.

In this work, we investigate the issues related to the high vacuum metal organic chemical vapor deposition (HV-MOCVD) and characterization of  $\text{ZrO}_2$  for high-k gate dielectric applications. In Chapter II, we will discuss the requirements of high-k materials, the properties of  $\text{ZrO}_2$ , and the deposition processes of  $\text{ZrO}_2$  thin films. In Chapter III, we will address ex-situ spectroscopic ellipsometry (SE) characterization of  $\text{ZrO}_2$  samples. In Chapter IV, we will address in-situ SE monitoring of the deposition process of  $\text{ZrO}_2$  during HV-CVD, and develop a model to describe the deposition process. In Chapter V, we will show comprehensive analysis results of  $\text{ZrO}_2$  samples deposited during HV-CVD, and confirm the model developed in Chapter IV. In Chapter VI, we will summarize the results obtained in this work, and make recommendations for future work.

## CHAPTER II

### BACKGROUND

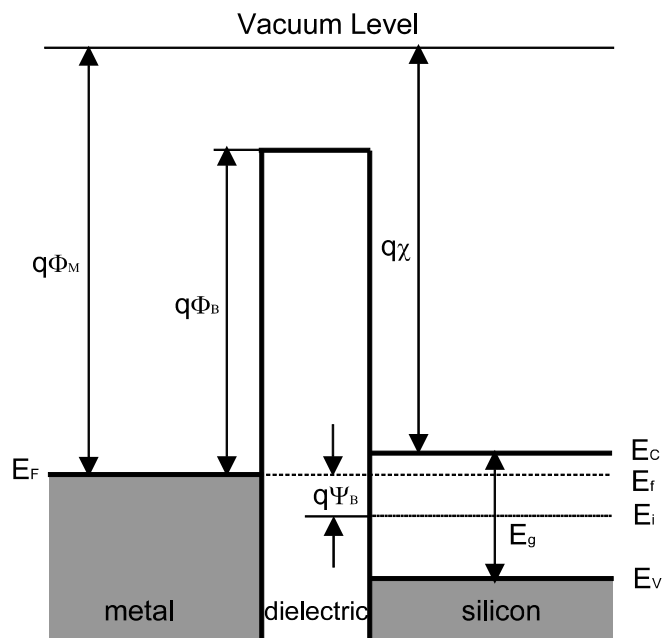
#### 2.1 High-k Material Property Requirements

High-k materials must meet a set of requirements to be a successful gate dielectric material. These requirements have been reviewed in detail<sup>5,12,22,30-36</sup>. We will summarize the property requirements on high-k materials, and will discuss more details on the deposition processes and properties of deposited ZrO<sub>2</sub> films in this chapter.

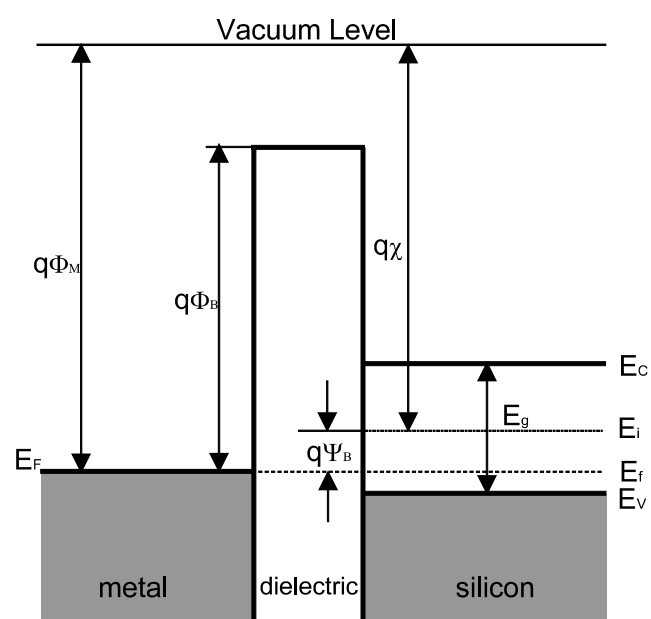
##### 2.1.1 Dielectric Constant and Band Offsets

Using a thicker dielectric material to replace silicon dioxide as the gate dielectric layer requires the dielectric material to have a higher dielectric constant than silicon dioxide ( $k_{\text{SiO}_2} = 3.9$ ). In addition to having a higher dielectric constant than silicon dioxide, the material must have a sufficient energy barrier height because the leakage current increases exponentially with decreasing energy barrier height<sup>5</sup>.

Figure 2 shows the energy band diagram of metal-dielectric-silicon stack structure at the flat-band condition, where  $\Phi_M$  is the work function of the metal,  $\chi$  is the semiconductor electron affinity,  $E_g$  is the semiconductor band gap,  $E_C$  is the conduction band,  $E_V$  is the valence band,  $E_F$  is the Fermi level,  $E_i$  is the intrinsic Fermi level of silicon, and  $\psi_B$  is the difference between the Fermi level and the intrinsic Fermi level of silicon. Electrons must overcome an energy barrier to create direct tunneling currents flowing between the silicon substrate and the gate. When the substrate is p-type silicon (Figure 2.a) the gate is typically positively biased, so electrons tend to travel from the



(a)



(b)

Figure 2: The band diagram for MIS diodes for (a) n-type and (b) p-type silicon substrate

silicon substrate to the gate. The energy barrier of this movement is the conduction band offset,

$$\Delta E_C = q[\chi - (\Phi_M - \Phi_B)] \quad (2.1)$$

When the substrate is n-type silicon (Figure 2.b), the gate is typically negatively biased, so electrons tend to travel from the gate to the silicon substrate. The energy barrier is

$$\Delta E_V = q\Phi_B \quad (2.2)$$

The conduction band offsets for high-k materials currently under investigation, are much lower than that of silicon dioxide (3.5 eV)<sup>35</sup>. This has become a disadvantage for high-k materials. Additionally, as shown in Figure 2, the barrier height is closely related to  $\Phi_B$ , which is often taken as half of  $E_g$  for the gate dielectrics<sup>35,9</sup>. Therefore, high-k materials of high band gap and band offset are most desirable.

Dielectric constants measured from thin film samples, especially the ultra thin films for gate dielectric applications, are seldom available. Typically dielectric constants measured from bulk materials are used in material selection. Figure 3 plots band gaps against dielectric constants of several materials currently under investigation. Although a conclusive quantitative relationship between band gaps and dielectric constant is not available, Figure 3 shows a trend that materials with higher dielectric constants tend to have lower band gaps. Among materials under investigation, ZrO<sub>2</sub>, HfO<sub>2</sub>, Y<sub>2</sub>O<sub>3</sub>, Al<sub>2</sub>O<sub>3</sub> show potential use for gate dielectrics. They have relatively high dielectric constants and high band offsets. Note that the dielectric constants measured from bulk materials are not the same as those measured from films. The crystallinity and structure more strongly affect the dielectric constants of thin film samples than bulk materials. Additionally, as we will discuss in Section 2.2, it is difficult to deposit high-k films on silicon without any

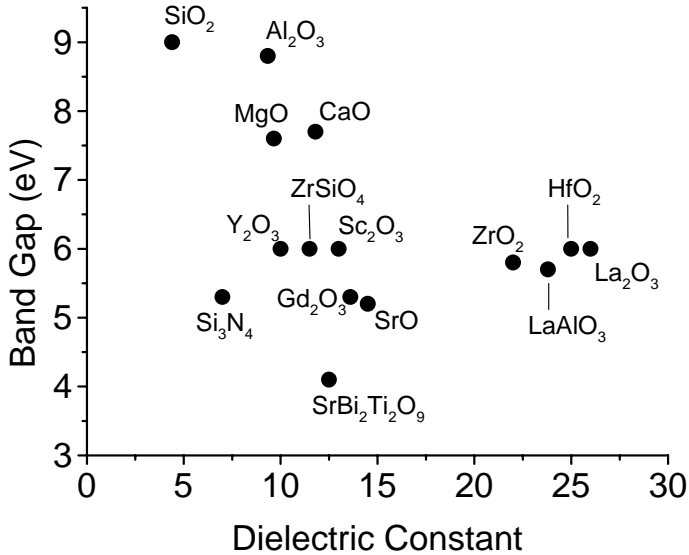


Figure 3: Plot of the optical band gaps and dielectric constants of some potential high-k gate dielectric materials<sup>30,32,37,38</sup>

interfacial layers. Measurements on thin film samples often obtain an effective dielectric constant, which includes the contribution from the whole dielectric-interfacial layer-silicon stack structure. These results are often lower than values measured from bulk materials.

### 2.1.2 Thermal Stability

The integration of high-k materials into MOSFET devices involves more than a physical replacement of the silicon dioxide layer by using high-k materials. The controllable abrupt low defect interface between silicon dioxide and silicon was one of the key factors to the success of the SiO<sub>2</sub>/Si material system in the semiconductor industry<sup>5</sup>. We have been discussing electrical property requirements on high-k material itself. We will discuss more details on the integration of high-k materials into MOSFET

structure and the requirements necessary to facilitate the proper operation of MOSFET devices.

Successful high-k materials need to be thermodynamically stable with the gate metal and silicon substrate. If the dielectric material reacts with the silicon substrate during deposition or in the subsequent IC fabrication processes, an interfacial layer will form. The interfacial layer could be composed of silicon dioxide, silicide, silicates, or an alloy of high-k material and silicon dioxide. The dielectric-interfacial layer-silicon stack structure behave as two capacitors in series, and the effective dielectric constant of the gate dielectric structure is

$$\frac{d_e}{k_e} = \frac{d_{high-k}}{k_{high-k}} + \frac{d_{interface}}{k_{interface}} \quad (2.3)$$

Since the dielectric constants of these interfacial materials are lower than high-k materials, the effective dielectric constant of the gate dielectric structure is significantly reduced. This further reduces the ultimate equivalent oxide thickness that can be achieved by using high-k materials

$$d_e = d_{interface} + (k_{interface}/k_{high-k})d_{high-k} \quad (2.4)$$

The formation of interfacial layers between high-k materials and the silicon substrate should either be prevented or minimized.

Systematic thermodynamic stability studies of metal oxides and metal nitrides have shown that only a limited number of materials have sufficient thermodynamic stability with silicon<sup>32,39</sup>. Both calculation and experimental results have shown that BeO, MgO, Al<sub>2</sub>O<sub>3</sub>, ZrO<sub>2</sub>, Be<sub>3</sub>N<sub>2</sub>, BN, AlN, Si<sub>3</sub>N<sub>4</sub>, Ti<sub>3</sub>N<sub>4</sub>, Zr<sub>3</sub>N<sub>4</sub> are stable with silicon at CMOS processing conditions<sup>32</sup>. However, we need to keep in mind that the formation of interfacial layers is strongly affected by the deposition process as well. Both reactants and

deposition intermediates can potentially react with the silicon substrate and form interfacial layers. To control the formation of an interfacial layer and minimize the interfacial layer thickness is the major goal of many studies. We will discuss these issues in detail in Section 2.2.

### 2.1.3 Interfacial Quality

A high-k film and the underneath silicon substrate form a heterogeneous interface. Materials on the two sides of the interface are composed of different atoms. The size and the coordination number of these atoms, the bond angles, and the bond strengths, are different. These differences cause lattice mismatch at the interface, creating dangling bonds and introducing defects. This will degrade carrier mobility and cause leakage current. Significant carrier mobility degradation will nullify the effort to promote performances by channel length scaling. The time to switch the MOSFET device may not be decreased even though the channel length has been shortened.

Recent theories on bonding constraints have been used to evaluate the issues related to the interface between the silicon substrate and high-k films<sup>40</sup>. Constraint theory is based on the idea that the bonding forces can be arranged in a hierarchy of different strength in a covalently bonded network. Bonding constraints are a linear function of the difference between the average coordination numbers at the interface, and the optimal coordination number is 2.4. If the average number of bonds per atom is larger than 3, the interfacial defect density increases proportionally<sup>40</sup>. The Si/SiO<sub>2</sub> interface has very low interfacial bonding misfit, and a very low average coordination number 2.67. Consequently, the Si/SiO<sub>2</sub> system has a midgap interface state density  $D_{it} \sim 2 \times 10^{10}$

states/cm<sup>2</sup>, which is ideal for gate dielectric application. Compared with the Si/SiO<sub>2</sub> system, Si/metal oxide systems have higher average coordination numbers, for example, 4.0 for Si/TiO<sub>2</sub>, 3.5 for Si/Ta<sub>2</sub>O<sub>5</sub>, and 3.6 for Si/Al<sub>2</sub>O<sub>3</sub><sup>40</sup>. In accordance with these bonding constraints results, most of recently reported high-k material/Si interfaces have a high midgap state density of 10<sup>11</sup> – 10<sup>12</sup> states/cm<sup>2</sup>, and a high flat-band voltage shift of more than 300 mV. Compared to the Si/SiO<sub>2</sub> interface, the bonding constrain problem is a very important issue for Si/high-k dielectric material system<sup>40-42</sup>.

Bonding constraint theory suggests surface engineering procedures before high-k dielectric deposition may help decrease the bonding constraints on high-k film/Si interface. A typical example of the application of bonding constraint theory is Si<sub>3</sub>N<sub>4</sub>. Si<sub>3</sub>N<sub>4</sub> is a good dielectric material, with a higher dielectric constant ( $k=7$ ) and the ability to effectively decrease tunneling current. However, the average coordination number of Si<sub>3</sub>N<sub>4</sub> is 3.43. The high interfacial bonding constraint makes it a bad candidate as a gate dielectric material<sup>43</sup>. Some researchers, however, have deposited silicon oxide/nitride onto silicon to form a Si-N-SiO<sub>2</sub> structure, dropping the coordination number to 2.8. Good results in lowering tunneling current have been obtained with this material system<sup>18,20,44-47</sup>. A similar result was reported recently on the property modification of Ta<sub>2</sub>O<sub>5</sub> films using N-doping methods<sup>48</sup>.

Other than N-doping methods, which involve foreign elements, silicate compounds have attracted much interest in high-k dielectric research. Due to the structural similarity between silicate and silicon oxide, both reduced tunneling current and reduced interfacial energy state densities were obtained in research<sup>27,28</sup>. Similarly, a recent report showed that the leakage current of Ta<sub>2</sub>O<sub>5</sub> film could be decreased by 10<sup>-4</sup>

$\text{A}/\text{cm}^2$  by carbon doping<sup>49</sup>. In a summary of the bonding constraint theory<sup>42</sup>, Lucovsky explained the necessity of the interfacial ultra-thin transition silicon oxide or silicate layer, and concluded that the  $\text{Zr}(\text{Hf})\text{O}_2\text{-SiO}_2$  and doped  $\text{Al}_2\text{O}_3$  interfaces will show the least interfacial constraint among the metal oxide type high-k dielectric candidates. At the same time, a ternary oxide stack structure, such as  $\text{SiO}_2/\text{ZrO}_2/\text{Y}_2\text{O}_3$ , was suggested for gate dielectric layers.

In addition to bonding constraints and dangling bonds on the interface, fixed charges on interface and in the high-k films is another factor that affects MOSFET operation. Their direct influence is on the shift of the flat-band voltage, which could further influence the threshold voltage of MOSFET devices<sup>9</sup>. Fixed interfacial charges can also affect the mobility in the channel through Coulomb scattering<sup>50</sup>. Fixed charges are often introduced during wet etching process before thermal oxidation in the traditional  $\text{SiO}_2/\text{Si}$  material system. Contamination control is the key to minimizing fixed charges. For a high-k/Si materials system, the problem of fixed charge is comparatively less critical because high-k films themselves will bring more metal ions on to the interface<sup>51</sup>.

#### 2.1.4 Morphology

Film morphology needs to be considered in high-k dielectric material selection. Most of the high-k dielectric films currently under investigation are polycrystalline or single crystalline, except for  $\text{Al}_2\text{O}_3$  films, which are amorphous<sup>5</sup>. Amorphous films have advantages over single crystalline and polycrystalline films. The potential problems of the single crystalline materials lie in possible anisotropic film properties. Also, the strict

process requirements are necessary to form these single crystalline films, e.g. molecular beam epitaxy, may lead to an industrially implausible process<sup>52-54</sup>. Polycrystalline films may be problematic due to high-leakage paths on the grain boundaries, while grain size and orientation variation in the polycrystalline films may cause significant variation in dielectric constants, possibly making the results irreproducible<sup>24,55</sup>. Amorphous materials eliminate the disadvantages discussed above. However, only a few amorphous material systems have been proven to be plausible as high-k dielectric materials, including Al<sub>2</sub>O<sub>3</sub> films<sup>5</sup> and Al<sub>2</sub>O<sub>3</sub>-ZrO<sub>2</sub> alloy systems<sup>56,57</sup>. Dielectric constants of these amorphous materials are significantly lower than polycrystalline materials.

Although the consideration of film morphology is reasonable for selecting high-k materials, the results are not conclusive. Polycrystalline ZrO<sub>2</sub> thin films deposited on an amorphous layer of SiO<sub>2</sub> have been shown to have excellent electric properties<sup>25</sup>. The dielectric constant for the ZrO<sub>2</sub> layer is between 25 and 35, while the interfacial silicate layer has a dielectric constant of 6-7. The D<sub>it</sub>,  $\sim 3.1 \times 10^{11}$  states/cm<sup>2</sup>, is in the lower end of D<sub>it</sub> values for high-k films. The properties can be further modified by alloying with HfO<sub>2</sub>. These results show that both the interfacial properties and the morphology have an impact on the electrical properties of high-k/interfacial layered stack structure. An amorphous high-k film is not the only possible solution to high-k applications.

In summary, the primary benefit for integrating high-k dielectrics is to block leakage currents so that smaller and faster devices can be made. However, in the reports published to date, the silicon/high-k dielectric interface has higher interfacial state densities compared to the Si/SiO<sub>2</sub> interface. A high interfacial state density directly degrades electron mobility in the channel. Electrons will need a longer time to travel

through a channel of the same length, so the switching rate of a MOSFET device can become even longer. Therefore, carrier mobility degradation due to high interfacial state density will nullify the benefit of further MOSFET scaling. For example, if the interfacial charge density increases from  $10^{10}$  to  $10^{11} \text{ cm}^{-2}$  after the integration of high-k dielectrics the electron mobility will be decreased by a factor of 2. Therefore, according to the constant field scaling laws, a scaling factor of more than 2 is necessary to offset this disadvantage. Additionally, low band offset values are potential problems for high-k dielectrics. The bonding constraint theory suggests that carefully deposited interfaces with submonolayer control of composition can help in obtaining a low defect interface. Therefore, both the properties of the high-k films and the properties of the interface or the interfacial layer between the high-k dielectric film and the silicon substrate are equally important for high-k dielectric applications.

The major goal of this work was to investigate the formation and the properties of  $\text{ZrO}_2$  film and the interfacial layers between  $\text{ZrO}_2$  and silicon. Before we discuss details of this work, we review the properties of  $\text{ZrO}_2$  and research reports related to  $\text{ZrO}_2$  deposition.

## 2.2 $\text{ZrO}_2$ Properties and Deposition

### 2.2.1 Outline of $\text{ZrO}_2$ Properties

$\text{ZrO}_2$  has several outstanding properties making it a leading high-k gate dielectric candidate material.  $\text{ZrO}_2$  has a large band gap ( $5.0\text{-}5.8 \text{ eV}^{35,58}$ ) and a relatively high conduction band offset (1.4 eV) among dielectric materials having similar dielectric constants<sup>35</sup>. The dielectric constant of  $\text{ZrO}_2$  is in the range of  $25\text{-}35^{25}$ . Thermodynamic

data have shown that pure ZrO<sub>2</sub> in contact with Si is stable at temperatures up to 1000 °C<sup>39</sup>. However, experimental results have shown that a zirconium silicide layer is formed on the interface when ZrO<sub>2</sub>/Si is annealed in high vacuum at temperatures higher than 900 °C<sup>59</sup>. Additionally, most research reports show an interfacial layer between ZrO<sub>2</sub> film and the silicon<sup>60-63</sup>. Since the interfacial layer is often composed of SiO<sub>2</sub> ( $k=3.9$ ) or silicate ( $k= 12.7$  as ZrSiO<sub>4</sub>), the effective dielectric constant of the gate dielectric structure is significantly degraded.

The disadvantage of ZrO<sub>2</sub> is its crystallinity. Amorphous ZrO<sub>2</sub> is not thermodynamically stable at room temperature<sup>64</sup>. Most research reports have shown that deposited ZrO<sub>2</sub> films are a polycrystalline material consisting of mixtures of the monoclinic, tetragonal, or cubic phases. We have discussed in Section 2.1.4 that polycrystalline films could be potentially problematic for high-k gate dielectric applications if properties of the ZrO<sub>2</sub> or interfacial layer are not well controlled. The nucleation process and the interfacial properties of ZrO<sub>2</sub> films on silicon must be well controlled.

### 2.2.2 Outline of Challenges in Deposition Processes

The deposition process for high-k materials presents a significant challenge. In MOSFET devices the dielectric layer has two critical interfaces, the top interface with the gate electrode material and the bottom interface with the silicon substrate. The major challenges with the top interface are related to compatibility issues between the dielectric and gate materials<sup>34</sup>.

The difficulties in depositing high-k film and forming a desirable bottom interface with the silicon substrate lie in the following three aspects.

First, since the k values of high-k materials of interests are between 10 and 35<sup>32</sup>, the target thickness of high-k gate dielectric layers is on the order of a few nanometers. Topology development during deposition could be large enough to affect the uniformity of high-k film properties. Thinner areas become weak spots for direct tunneling currents. The deposition process will have to be able to controllably deposit very uniform ultra thin films.

Second, unlike silicon dioxide, which is grown into the silicon substrate through thermal oxidation<sup>65</sup>, high-k gate dielectric layers have to be deposited on the silicon substrate. Both predeposition surface preparation and deposition process itself can strongly affect the properties of the interface, such as interfacial state density and fixed charge density, which further affect MOSFET parameters<sup>9</sup>. Hence, the process for forming high-k films must be able to control the formation and the quality of the interface.

Third, the interfacial layer can be both beneficial and detrimental for high-k gate dielectric applications. The interfacial layer helps relax the bonding constraints on the interface. Accordingly, the interfacial layer helps prevent significant carrier mobility degradation and benefits MOSFET operation. At the same time, the interfacial layers are often amorphous. A high quality interfacial barrier layer can help block direct tunneling currents even though the high-k dielectric film itself is polycrystalline. Bonding constraint theory suggests that a 3-6 Å thick interfacial layer is necessary for lowering the

bonding constraints on the interface. However, the thickness of interfacial layers must be minimized to prevent unnecessary effective dielectric constant degradation.

In brief, film property control, such as the control on thickness, composition, and microstructure, is the basic requirement for the deposition process of high-k dielectric films. The gate dielectric application has more requirements related to interfacial property control. The formation of the interface, the thickness of the interfacial layer, uniformity of these ultra thin gate dielectric films are all critical parameters for MOSFET operation. They will affect device parameters such as gate capacitance, the threshold voltage, and the flat-band voltage. Detailed study of the initial-stage deposition and nucleation of high-k dielectric films is critical for solving these technical difficulties.

Before detailing our research work, we will review some deposition processes for high-k gate dielectric films. Since sputtering and plasma enhanced chemical vapor deposition processes can potentially damage the silicon substrate and induce defects, we will limit the discussion to atomic layer chemical vapor deposition (ALCVD), molecular beam epitaxy (MBE), and metal organic chemical vapor deposition (MOCVD). We will show that initial-stage deposition and nucleation control are critical for the deposition process of high-k gate dielectric films. We will also discuss details of the chemistry of the deposition process and its influence on the nucleation behavior and film properties.

### **2.2.3 Atomic Layer Chemical Vapor Deposition (ALCVD)**

ALCVD has attracted the most attention in recent years for depositing high-k dielectric films, including  $\text{ZrO}_2^{25,28,59,66-82}$ . ALCVD processes use serial reactions between two chemicals, typically a precursor containing proper metal elements, such as

metal chloride, and an oxidant, such as water vapor, to deposit films. A typical ALCVD cycle has four steps:

- 1) The substrate is exposed to water and forms an oxidized sub-monolayer or monolayer. The substrate surface is changed into a hydroxyl group terminated surface.
- 2) The deposition chamber is purged with inert gas, such as nitrogen, to clean residual oxidant in the deposition chamber.
- 3) The surface is exposed to metal precursor vapor, such as metal chloride. Since metal chloride can only react with the surface hydroxyl group, a sub-monolayer to a monolayer metal component is deposited. The surface is changed into a metal chloride terminated surface.
- 4) The process is finished with another purging step to clear residual metal precursor.

Therefore, one metal oxide monolayer can be deposited in each deposition cycle. Metal oxide films can be deposited in multiple deposition cycles. In practice, most processes operate in an ALCVD “process window”<sup>83</sup>, typically in the temperature range of 300-350 °C, providing enough thermal energy to allow the chemical reactions to complete quickly. Since at least one reactant is limited by chemical surface adsorption, the deposition proceeds in a layer-by-layer mode. Therefore, the deposition rate does not change with increasing temperatures<sup>81,83</sup>.

ZrO<sub>2</sub> ALCVD is often operated at 300-350 °C by using ZrCl<sub>4</sub>-H<sub>2</sub>O as precursors<sup>25,66-69,72,80,81</sup>. A deposition rate on the magnitude of ~ 1 Å/cycle was reported<sup>81</sup>. Because the process proceeds layer by layer, ZrO<sub>2</sub> of a desired thickness can be

controllably deposited. All the deposited ZrO<sub>2</sub> films are polycrystalline, consisting of both the tetragonal and monoclinic phases. The grains are separated by amorphous ZrO<sub>2</sub><sup>59,66</sup>. However, ZrO<sub>2</sub> films show significantly different properties when different substrates were used. These substrates included hydrogen terminated silicon (100) (H-Si)<sup>59,67,71,84</sup>, native silicon oxide<sup>25,66,68,72</sup>, thermal silicon dioxide<sup>59,67,84</sup>, fused quartz<sup>71</sup>, glasses<sup>69,81</sup>, silicon nitride<sup>25</sup>, and silicon oxynitride<sup>67</sup>. Based on the surface termination of these substrates, the starting surfaces can be classified into three types: hydrogen terminated surfaces (H-Si), hydroxyl group terminated surface (HO-Si), including all the oxidized substrates and glasses, and nitride or oxynitride terminated surfaces.

When H-Si is used as the starting surface, hydrogen termination acts as a passivation layer against the initial surface saturation with water molecules, causing uneven nucleation. The resulting ZrO<sub>2</sub> films consist of ZrO<sub>2</sub> islands<sup>25,59</sup>. High surface roughness and high leakage currents were reported from ZrO<sub>2</sub> films deposited on H-Si. This indicates that ZrO<sub>2</sub> deposited on H-Si is not suitable for gate dielectric applications<sup>25,67,84</sup>. Additionally, although the silicon substrate is not intentionally oxidized before deposition, 10-20 Å thick interfacial layers often exist between ZrO<sub>2</sub> films and the silicon substrate<sup>25,59</sup>. Using H-Si surfaces does not, as expected, minimize the thickness of interfacial layers.

When HO-Si is used as the starting surface, the resulting ZrO<sub>2</sub> films are uniform. Since the silicon substrates are oxidized before deposition, interfacial layers are present. These layers are 12-22 Å thick<sup>59,72</sup>, very close to the silicon oxide layer before deposition. No apparent oxidation of the silicon substrate occurred during deposition<sup>72</sup>. Surface preparation, instead of deposition conditions, is discovered to be the major factor in

determining the interfacial layer thickness<sup>25</sup>. The interdiffusion between ZrO<sub>2</sub> and SiO<sub>2</sub> is very low at deposition temperatures, and the interface between ZrO<sub>2</sub> and the silicon oxide layer is abrupt<sup>72</sup>. However, other reports show that the interfacial layer consisted of zirconium silicate, suggesting possible ZrO<sub>2</sub> and silicon oxide interdiffusion<sup>25</sup>. High temperature annealing results show that the interdiffusion between ZrO<sub>2</sub> and SiO<sub>2</sub> is important, resulting in a zirconium silicate layer<sup>66</sup>. ZrO<sub>2</sub> deposited on OH-Si has superior electrical properties to ZrO<sub>2</sub> films deposited on H-Si. Leakage currents in a ZrO<sub>2</sub>/SiO<sub>2</sub> structure are 4-5 orders of magnitude lower than SiO<sub>2</sub> of equivalent electrical thickness<sup>84</sup>. Low surface state densities on the order of  $10^{11}/\text{cm}^2\text{eV}$  have been reported<sup>25,84</sup>. These properties show that ZrO<sub>2</sub> is potentially suitable for high-k dielectric applications.

ALCVD process using ZrCl<sub>4</sub>-H<sub>2</sub>O relies on careful predeposition surface preparation to obtain a HO-Si starting surface. An interfacial layer must be intentionally introduced before the deposition process can proceed. The thickness of this oxidized layer must be minimized. Therefore, oxynitride and silicon nitride were used as interfacial layers. Oxynitride surfaces and silicon nitride surfaces have higher dielectric constants than silicon dioxide. At the same time, they provide additional protection against silicon oxidation during deposition. The nucleation behavior of ZrO<sub>2</sub> on nitride or oxynitride surfaces is not as problematic as it is for deposition on H-Si. At an EOT value of 13.8 Å, a leakage current of  $10^{-5}\text{ A/cm}^2$  at 1 V below flat-band, and a D<sub>it</sub> of  $\sim 1\times 10^{12}/\text{cm}^2\text{eV}$  have been obtained for ZrO<sub>2</sub> deposited on silicon nitride. These properties are slightly worse than ZrO<sub>2</sub> deposited on HO-Si.

Another shortcoming of ALCVD process using ZrCl<sub>4</sub>-H<sub>2</sub>O is the uneven nucleation on H-Si surfaces. Different precursor combinations were investigated to

improve the nucleation behavior of  $\text{ZrO}_2$  on H-Si surfaces. One of the representative combinations is zirconium t-butoxide (ZTB) and  $\text{H}_2\text{O}^{70,78,79}$ . In ALCVD, the substrate is first exposed to ZTB, instead of water vapor as in ALCVD using  $\text{ZrCl}_4\text{-H}_2\text{O}$ , and then exposed to water vapor<sup>78,79</sup>. Since ZTB decomposes at temperatures higher than 250 °C, ZTB is often used in MOCVD of  $\text{ZrO}_2$  films. To prevent the thermal decomposition of ZTB, ALCVD using ZTB- $\text{H}_2\text{O}$  is operated at temperatures lower than 300 °C. By optimizing the exposure time and pressure range of ZTB and  $\text{H}_2\text{O}$  exposure, a uniform amorphous  $\text{ZrO}_2$  film can be obtained on H-Si surface<sup>78,79</sup>. The amorphous structure is preserved even after 400 °C annealing in  $\text{N}_2^{78,79}$ . It was discovered that both the lowest deposition rate and the lowest surface roughness were achieved using temperatures in the range of 200-250 °C<sup>78,79</sup>. The author postulated that excessive surface adsorption at lower temperatures and excessive decomposition of ZTB at higher temperatures could be the cause of high surface roughness. The relationship between deposition rate and surface roughness was not clearly understood.

Thermal decomposition of ZTB also occurs in the temperature range used for these studies. Therefore, the deposition does not proceed strictly in a layer-by-layer fashion, although a steady deposition rate can be achieved. ALCVD using ZTB- $\text{H}_2\text{O}$  also shows a 12-15 Å thick interfacial layer<sup>78,79</sup>, similar to results of ALCVD using  $\text{ZrCl}_4\text{-H}_2\text{O}$ . Silicon nitride was also used as starting surface for ALCVD of  $\text{ZrO}_2$  from ZTB- $\text{H}_2\text{O}$ . The oxidation of the silicon substrate was effectively suppressed by the silicon nitride interfacial layer. Film electrical properties, such as  $D_{it}$  in the range of  $10^{12}/\text{cm}^2\text{eV}^{78}$ , have been reported from films deposited from  $\text{ZrCl}_4\text{-H}_2\text{O}$ . However, the flat-band voltage was as high as 400-500 mV due to a high density of fixed charges<sup>78</sup>. A

separate report showed that high residual contamination, such as carbon and hydrogen, can be present in  $\text{ZrO}_2$  deposited from ZTB- $\text{H}_2\text{O}$ <sup>70</sup>.

Devices fabricated with  $\text{ZrO}_2$  deposited by ALCVD processes using  $\text{H}_2\text{O}$  exhibit high flat-band voltage shift (up to 0.9 mV<sup>72,74,79,84</sup>) and high hysteresis (up to 250 mV<sup>25,74</sup>). After annealing, devices fabricated using  $\text{ZrO}_2$  deposited by ALCVD from  $\text{Cp}_2\text{Zr}(\text{CH}_3)_2$  (where Cp=cyclopentadienyl,  $\text{C}_5\text{H}_5$ ) and  $\text{O}_3$  have demonstrated almost no flat-band voltage shift, and significantly reduced hysteresis<sup>74</sup>. However, the reactive  $\text{O}_3$  oxidized the silicon substrate, resulting in a 19 Å thick interfacial layer<sup>74</sup>.

At the processing conditions stated above, oxygen or water can react with zirconium precursor or the silicon substrate, forming an interfacial layer between the silicon and the substrate. An alternate ALCVD process, rapid thermal chemical vapor deposition (RTCVD), using ZTB and  $\text{O}_2$  has been developed. In RTCVD, the reactivity of  $\text{O}_2$  is lowered by changing the substrate temperature during oxygen exposure<sup>60,61,85</sup>. Results show that the interfacial layer, a silicate formed during deposition, can be reduced to less than 10 Å. As in ALCVD using  $\text{ZrCl}_4$  and  $\text{H}_2\text{O}$ , RTCVD  $\text{ZrO}_2$  nucleates differently on H-Si and HO-Si surfaces, leading to distinct film property differences<sup>85</sup>.

In summary, the major advantage of ALCVD of  $\text{ZrO}_2$  is its layer-by-layer deposition, allowing films of desired thickness to be controllably deposited. However, when the starting surface is H-Si, layer-by-layer deposition cannot be achieved using  $\text{ZrCl}_4$  and  $\text{H}_2\text{O}$  due to the lack of reactive sites. This results in a non-uniform, leaky  $\text{ZrO}_2$  film. Uniform deposition can be achieved by using either a HO-Si surface or a different precursor combination, such as ZTB- $\text{H}_2\text{O}$ . When ZTB and  $\text{H}_2\text{O}$  are used as precursors, the silicon surface was first exposed to ZTB at a temperature that ZTB can thermally

decompose. Consequently, the first layer is at least partially formed by the thermal decomposition of ZTB. Therefore, although ALCVD process can theoretically deposit metal oxides layer-by-layer, the properties of deposited films are determined by factors other than the ALCVD process itself. H<sub>2</sub>O used in ALCVD also introduces more fixed charges in the film and high level of unsaturated bonds, resulting in high hysteresis and high flat-band voltage shift in devices fabricated with these films. A transition period, at the very beginning of deposition process, has been reported for ALCVD on both H-Si and HO-Si surfaces<sup>67</sup>. In this transition period, the deposition rate increases with deposition time. This phenomenon has not been well understood though the properties of the starting surface were shown to be most influential. Details on initial-stage deposition, especially the formation of the first uniform layer and its impact on the properties of later deposited film, still need further investigation.

#### **2.2.4 Molecular Beam Epitaxy (MBE)**

Molecular beam epitaxy (MBE) is a method to deposit ultra thin films. While the name MBE refers to the deposition of an epitaxial film, it can also be used to deposit other types of films. In ZrO<sub>2</sub> MBE, a zirconium atom beam flows through an oxygen ambient towards a silicon substrate<sup>86,87</sup>. Wang reported that yttrium stabilized ZrO<sub>2</sub> on silicon without an interfacial layer can be formed at 730 °C and 10<sup>-5</sup> mbar ambient oxygen, even with a native silicon oxide starting surface<sup>86</sup>. This was explained by the reaction between Zr atoms and silicon dioxide,



A low  $D_{it}$  of  $2 \times 10^{11}/\text{cm}^2\text{eV}$  and a low leakage current of  $1.1 \times 10^{-3} \text{ A/cm}^2$  at 1.0 V bias were reported for devices made from the resulting film. However, at higher ambient oxygen pressures,  $> 1.5 \times 10^{-5}$  Torr, silicon substrate oxidation occurs at a temperature as low as 300 °C, resulting in the formation of an interfacial silicon dioxide<sup>87</sup>. By controlling the oxygen partial pressure during heat treatment, a ZrO<sub>2</sub> layer without interfacial layer can be produced by MBE<sup>87</sup>. In a separate report, ZrO<sub>2</sub> with a band gap of 5.5 eV, a valence band offset of 3.35 eV, and a midgap state density,  $D_{it}$ , in the range of  $10^{10}$ - $10^{12}/\text{cm}^2\text{eV}$  have been produced by MBE<sup>88</sup>. Details on the nucleation of ZrO<sub>2</sub> on H-Si surface during MBE were not reported, while the ZrO<sub>2</sub> layer on HO-Si surface has been shown to be atomically flat<sup>86</sup>. This is similar to the case of ZrO<sub>2</sub> ALCVD on HO-Si.

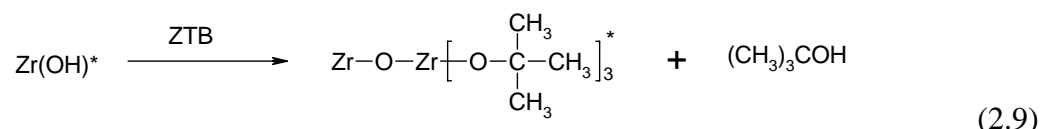
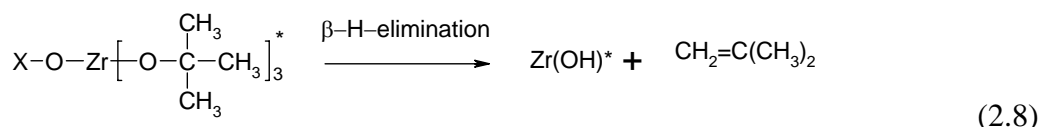
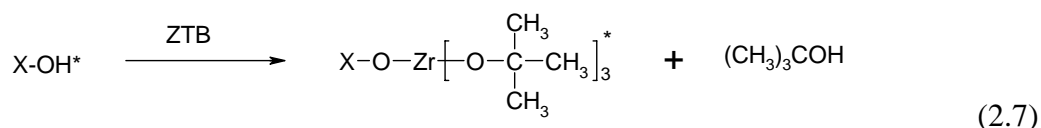
In an MBE process operated at  $\sim 10^{-7}$  Torr, ZTB was used as the zirconium source<sup>89</sup>. Both the oxidation and the decomposition of ZTB itself occurred on H-Si surface, resulting in a 14 Å thick interfacial layer. Additionally, a nucleation behavior similar to the nucleation of ZrO<sub>2</sub> on H-Si during ALCVD was reported. Devices made from the resulting film had high leakage current densities,  $10^{-2}$ - $10^{-3} \text{ A/cm}^2$  at  $\pm 1.5$  eV bias<sup>89</sup>.

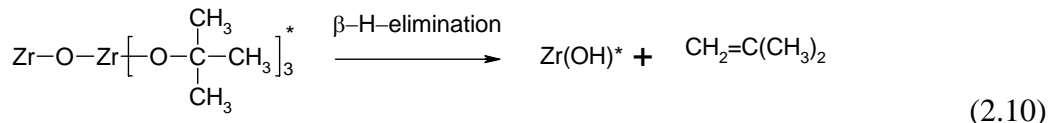
In the above MBE process, oxygen is required to oxidize zirconium atoms or ZTB molecules. However, excessive oxygen will directly lead to the formation of interfacial layers due to substrate oxidation. The partial pressure and the substrate temperature must be carefully controlled. Low deposition rates, a few Å/min, and expensive, complicated MBE reactors make MBE an unfavorable process for high volume manufacturing. More importantly, these results have shown that a ZrO<sub>2</sub> film without an interfacial layer can be formed at appropriate conditions, and desirable electrical properties can be obtained.

## 2.2.5 Metal Organic Chemical Vapor Deposition (MOCVD)

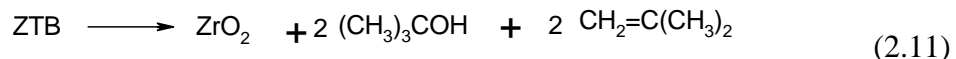
MOCVD is a common method to deposit thick ZrO<sub>2</sub> films. Two major types of metal organic precursors have been used in these processes: zirconium alkoxides<sup>23,90-93</sup> and zirconium  $\beta$ -diketonates<sup>94-96</sup>. In recent reports, hybrids of these two types of precursors<sup>97,98,99</sup> have been used to deposit ZrO<sub>2</sub>. The major advantage of zirconium  $\beta$ -diketonates is their stability against hydrolysis, but residual carbon contamination is a major problem<sup>100</sup>. Oxygen is often required to deposit high purity ZrO<sub>2</sub> films from zirconium  $\beta$ -diketonates. As in ALCVD and MBE, ambient oxygen environments in MOCVD causes silicon substrate oxidation and form an interfacial layer<sup>62,97</sup>.

Research on the decomposition of zirconium alkoxides suggests that the use of oxygen can be minimized if appropriate zirconium alkoxides are used as the precursor<sup>23,93,101</sup>. In 1959 Bradley reported the importance of surface hydroxyl groups in the thermal deposition of ZTB<sup>101</sup>. At elevated temperatures, the decomposition of ZTB is initiated by a self-catalyzed reaction due to trace impurity hydroxyl groups present in ZTB or on the internal surface of distillation apparatus. Then, the chemically adsorbed t-butoxy intermediate undergoes  $\beta$ -H-elimination to deposit ZrO<sub>2</sub> and regenerate the hydroxyl groups:

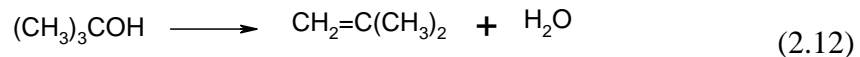




This reaction mechanism was later confirmed by Cameron in 1999<sup>23</sup>. In 2002, Burleson took the physical adsorption equilibrium of ZTB molecules on  $\text{ZrO}_2$  surface into consideration, and extracted the kinetic parameters of deposition reactions<sup>93</sup>. The stoichiometry of the deposition reaction can be expressed as



Therefore, a mass balance on oxygen can be maintained during deposition without using additional oxygen gas or water. Additionally, the dehydration reaction of alcohols at elevated temperatures is well known,



At high temperatures, water generated from the dehydration reaction could be a potential problem for substrate oxidation.

The topology of  $\text{ZrO}_2$  deposited by MOCVD on different surfaces has not been well studied. MOCVD of  $\text{ZrO}_2$  from zirconium isopropoxide on Pt surfaces has been divided into three stages: nucleation, coalescence, and bulk layer growth<sup>90</sup>. Surprisingly, nucleating layers thinner than 80 Å are composed of segregated islands, which cause high surface roughness in the bulk layer growth stage<sup>90</sup>. When  $(\text{C}_3\text{H}_7\text{O})_2(\text{C}_{11}\text{H}_{19}\text{O}_2)_2\text{Zr}$  and oxygen were used to deposit  $\text{ZrO}_2$  on H-Si surfaces, nucleation inhibition similar to that in ALCVD on H-Si occurs. This results in a rough surface and segregated islands<sup>97</sup>. In a separate report, when  $\text{Zr}(\text{O}-\text{i-Pr})_2(\text{thd})_2$  and oxygen were used to deposit  $\text{ZrO}_2$  on silicon oxide surfaces, a lower surface roughness was obtained<sup>62</sup>. The chemical composition of

the interfacial layer was not related to the starting surface. Interfacial silicate layers were reported for deposition on both H-Si and silicon oxide surfaces<sup>62,97</sup>.

ZrO<sub>2</sub> deposited by MOCVD have good electrical properties. ZrO<sub>2</sub> films in most of reports were hundreds to thousands of Å thick. Devices made from ZrO<sub>2</sub> films in this thickness range showed very low flat-band voltage shift of 0.1 V<sup>95</sup>. This is a much better result than ALCVD results because flat-band voltage shift often increases with increasing film thickness due to fixed charge accumulation in films. A low midgap interfacial state density, D<sub>it</sub>, of  $5 \times 10^{11}/\text{cm}^2\text{eV}$  for ZrO<sub>2</sub> after forming gas annealing was reported<sup>102</sup>.

Post deposition annealing of MOCVD ZrO<sub>2</sub> films produced contradictory results. An interfacial layer thickness increase has been shown after high temperature (850 °C) annealing in oxygen<sup>62,97</sup>. For films deposited on H-Si, the ZrO<sub>2</sub> diffuses into the interfacial layer to form zirconium silicate, reducing the ZrO<sub>2</sub> layer thickness<sup>62,97</sup>. For films deposited on silicon dioxide, this ZrO<sub>2</sub> thickness reduction is not observed<sup>62</sup>. Similar to the results obtained by other deposition method, high temperature annealing in ultra high vacuum will also result in interfacial layer decomposition, and the formation of interfacial silicide<sup>103</sup>.

Several precursor systems and various operation conditions have been used in ZrO<sub>2</sub> MOCVD. A comparison of the advantages and disadvantages of different MOCVD processes is very difficult. The results that we have discussed show that, for MOCVD, different starting surfaces may also affect the nucleation of ZrO<sub>2</sub> films, the topology of films, as well as the stability of interfacial layers. At MOCVD conditions, precursors are very likely to react either with the silicon substrate or with silicon dioxide to form an interfacial silicate layer. However, no work so far has proven this. The decomposition of

zirconium alkoxide shows possibilities of depositing ZrO<sub>2</sub> films without using oxygen or water. However, in most reports depositions without oxygen participation showed high carbon contamination. Details on predeposition surface preparation, ZrO<sub>2</sub> nucleation on different surfaces and at different deposition conditions need further investigation.

In this section, we have reviewed the up to date progress in the area of ZrO<sub>2</sub> deposition for high-k applications over the last few years. Almost all the deposited ZrO<sub>2</sub> films were polycrystalline. The polycrystalline structure appears not to be a strong factor in determining the films' electrical properties. Instead, the nucleation process has been shown to be critically important. The ALCVD process provides the best results so far in terms of film thickness control, film quality, and process operability. However, ALCVD is limited by the use of water vapor as a precursor, resulting potential substrate oxidation, and devices with high flat-band voltage shift. MBE and MOCVD have been shown to deposit ZrO<sub>2</sub> with desirable film properties, but the initial-stage deposition and the nucleation of ZrO<sub>2</sub> have not been studied. Results obtained from MBE and MOCVD have only been interpreted on a case-by-case basis. An overall picture of these processes is not clear. Additionally, the participation of oxygen is not essential in MOCVD process when the proper precursor is used. The deposition conditions must be carefully optimized. Details on the effects of deposition parameters on film properties need careful investigation.

In this work, we investigate the initial-stage deposition of ZrO<sub>2</sub> on different surfaces during high vacuum MOCVD and develop a general description of the initial stages of deposition. Since the properties of ultra thin ZrO<sub>2</sub> were not known when I started this work, my research began with ellipsometry characterization methodology

development for ZrO<sub>2</sub> films. Details of my research work will be discussed in the following chapters.

## CHAPTER III

### SPECTROSCOPIC ELLIPSOMETRY CHARACTERIZATION OF ZIRCONIA FILMS ON SI(100) DEPOSITED BY HV-MOCVD

#### 3.1 Background

An interfacial layer composed of either silicon oxide<sup>104</sup> or silicates<sup>25,60-63,105</sup> often exists between the high-k material and the silicon substrate. Interfacial layers have multiple effects on the performance of MOSFET devices. The dielectric constants of silicon oxide and silicates are lower than those of high-k dielectric materials<sup>22</sup>. As a result, the interfacial layer degrades the effective dielectric constant of the overall dielectric stack structure. Additionally, the quality of the interface will influence the mobility of carriers in the channel region<sup>5</sup>. For industrial applications, the thicknesses and properties of both high-k and interfacial layers need to be quickly evaluated using non-destructive characterization methods<sup>106</sup>.

Spectroscopic ellipsometry (SE) is a fast, sensitive, and nondestructive method for thin film characterization<sup>107</sup>. It requires no special environments, does not directly contact samples, and can easily be integrated into semiconductor processing. When appropriate modeling methods have been developed, the thickness and the properties of thin films, such as composition, structure, and surface-roughness, can be simultaneously extracted from SE data. These advantages make SE a good technique for controlling integrated circuit production. However, little has been reported about the optical properties of very thin high-k dielectric films, or about the optical properties of the interfacial layers. The goal of this chapter is to investigate appropriate SE data-analysis methods to characterize high-k dielectric films on silicon, by using ZrO<sub>2</sub> on Si as a model system.

The ZrO<sub>2</sub>/Si material system has complex interfacial properties. Thermodynamic calculations suggest that the interface between ZrO<sub>2</sub> and Si is stable<sup>39</sup>. However, interfacial layers between ZrO<sub>2</sub> and silicon substrates have been reported by multiple researchers<sup>25,60-63,104,105</sup>. The chemical composition of such layers is highly affected by deposition methods and conditions. In reactive sputtering or plasma-assisted chemical vapor deposition, excited energetic oxygen species help form an amorphous interfacial SiO<sub>2</sub> layer<sup>104</sup>. The interfacial layer can also be a silicate under certain reactive sputtering conditions<sup>104,105</sup>. The interfacial layers resulting from chemical vapor deposition processes, including ALCVD<sup>25,60</sup>, RTCVD<sup>61</sup>, MOCVD<sup>62</sup>, are often amorphous silicate layers. The presence of these silicate layers has been confirmed by transmission electron microscopy (TEM)<sup>25,60,62,105</sup>, and X-ray photoelectron spectroscopy (XPS)<sup>25,60-62,104</sup>, a dielectric constant of 6 to 7<sup>25,105</sup>, and a lower etching rate in HF than SiO<sub>2</sub><sup>61</sup>.

Previous ellipsometric analyses used a two-layer model to simulate the ZrO<sub>2</sub> layer and the interfacial layer<sup>63,106</sup>. By assuming the interfacial layer to be silicon dioxide, Chism and Diebold extracted the Tauc-Lorentz model (TL) parameters to describe the optical constants of ZrO<sub>2</sub> deposited by ALCVD<sup>63,106</sup>. Other research groups used an effective medium approximation (EMA) layer composed of silicon dioxide and ZrO<sub>2</sub> to simulate the interfacial layer<sup>108</sup>. Although the parameters can be decorrelated during data processing, the optical constants of the interfacial layer were arbitrarily set to those of silicon dioxide, or to those of a mixture of SiO<sub>2</sub> and ZrO<sub>2</sub>. The absorptive band tail from the interfacial layer was not separated from that of the ZrO<sub>2</sub> layer. The effective ZrO<sub>2</sub> layer in these previous works actually represented a combined contribution from both the

interfacial and ZrO<sub>2</sub> layers. It is therefore not accurate to use such models to characterize both the thickness and properties of the ZrO<sub>2</sub> and interfacial layers.

In this chapter, we use multiple-sample variable-angle spectroscopic ellipsometry (MS-VASE) to extract the optical constants of ZrO<sub>2</sub>. Based on the data, we discuss issues related to characterization of the interfacial layer, and compare the results with TEM and AFM analyses.

### **3.2 Experimental Details**

#### **3.2.1 High Vacuum Chemical Vapor Deposition System**

MOCVD of ZrO<sub>2</sub> films from ZTB was preformed in a single wafer ultra high vacuum (UHV) compatible chemical vapor deposition (CVD) system shown in Figure 4. The CVD system was evacuated by a turbo-molecular pump to a typical base pressure of  $5 \times 10^{-9}$  Torr. Three-inch silicon wafers were introduced through a load lock onto a susceptor hanging from the top of the chamber. The wafer was held polished side down and was heated from the backside. Stage temperatures were measured by a C-type thermal couple embedded into the sample heater, and controlled by an Eurotherm 2408 temperature controller with  $\pm 0.1$  °C accuracy. The wafer temperature was assumed to be the same as heater temperature. The wall of the deposition chamber was heated by a resistively heated rod to 150 °C and was controlled by an Omega CN 77000 controller.

An in-situ J.A. Woollam model M-2000D spectroscopic ellipsometer was installed on the deposition chamber. Two fused silica windows were used in the optical path to separate the vacuum from the ambient environment. A QTH lamp and a D<sub>2</sub> lamp

were used simultaneously to generate a beam with a photon energy range of 1.2 - 6.5 eV. The light beam struck the center of the wafer at a  $71^\circ$  incidence.

### 3.2.2 Sample Preparation

We used ZTB as the precursor to deposit  $\text{ZrO}_2$  films. The partial pressure of ZTB in deposition chamber is in the range of  $10^{-5}$ - $10^{-3}$  Torr, which is controlled by the temperature of the ZTB container. No carrier gas or other diluent gases were used in the deposition process.

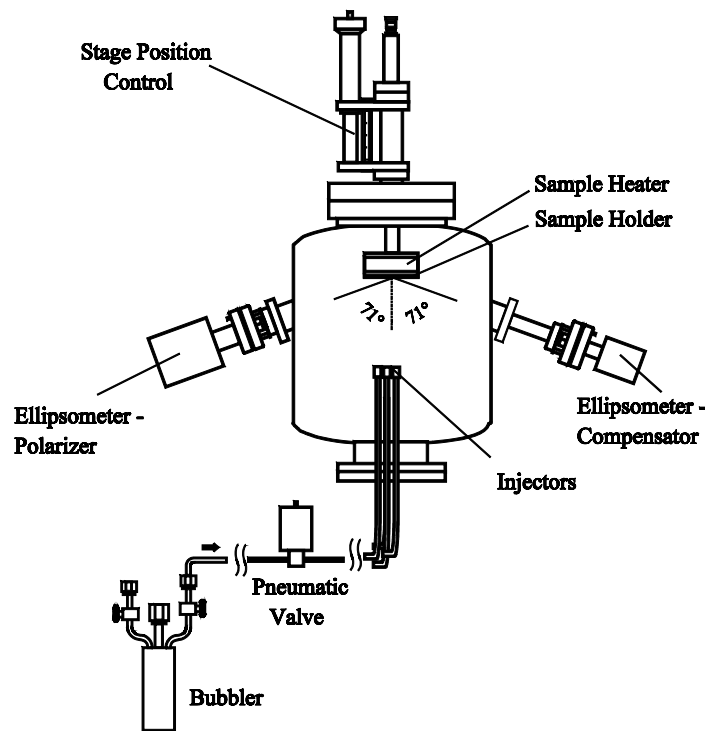


Figure 4: A schematic of high vacuum chemical vapor deposition system

Three inch Si(100) wafers with resistivities between 1 and 10  $\Omega\cdot\text{cm}$  were used as substrates. Before deposition, the native silicon oxide layer was etched off by using a 40 sec 1:50 HF-DI water dip, followed by a 150 sec DI-water rinse, and nitrogen drying. The silicon surface was changed into hydrogen atoms covered surface (H-Si) after the cleaning process<sup>109</sup>. The H-Si substrate was promptly transferred into the CVD system after cleaning. In the deposition chamber, the substrate was first heated to the desired temperature in the range of 300 to 475 °C. Once the temperature stabilized for approximately 5 minutes, the pneumatic valve in the transfer line was opened. The reaction precursor vapor, ZTB, was introduced through the bottom of the deposition chamber. ZTB molecules transfer on to the silicon surface and decompose into  $\text{ZrO}_2$ . The growth of  $\text{ZrO}_2$  was monitored in real time by in-situ SE. We used a Cauchy model to extract the nominal film thicknesses during deposition. We stopped depositions when the thickness of  $\text{ZrO}_2$  films reached 200 Å or the deposition time was longer than 20 min. The thicknesses of deposited films were in the range of 170 - 300 Å. After deposition, the silicon wafer was cooled down in  $10^6$  torr vacuum to room temperature before it was transferred out of the CVD system.

### **3.2.3 Ex-situ Spectroscopic Ellipsometry (SE)**

Ex-situ SE data from as-deposited samples were collected on a J.A. Woollam M-2000D multi-angle spectroscopic ellipsometer at 60, 65, 70, 75, and 80° incident angles. Scans were collected for 60 seconds at each incident angle to minimize random noise in collected data.  $\Psi$  and  $\Delta$  values within the full photon energy range of our ellipsometer, which is 1.2 to 6.5 eV, were used for data fitting.

Data processing was conducted using WVASE 32, a software application developed by J.A. Woollam Company. Data from six samples were used to extract the optical constants. The six samples were selected from 40 samples deposited at various substrate temperatures and total pressures. The Cauchy model was used to extract the refractive indexes of the samples at 633 nm (1.96 eV). Figure 5 shows the averages and standard deviations of the nominal refractive indexes of films deposited using different conditions. Multiple effects, such as low film density<sup>110,111</sup> and high impurity contents<sup>70</sup>, can cause low refractive indexes at low deposition temperatures. Therefore, six samples, deposited between 425 and 475 °C, were analyzed to extract the optical constants. Among the six ZrO<sub>2</sub> samples, four were deposited at 425 °C, and the other two samples were deposited at 450 and 475 °C.

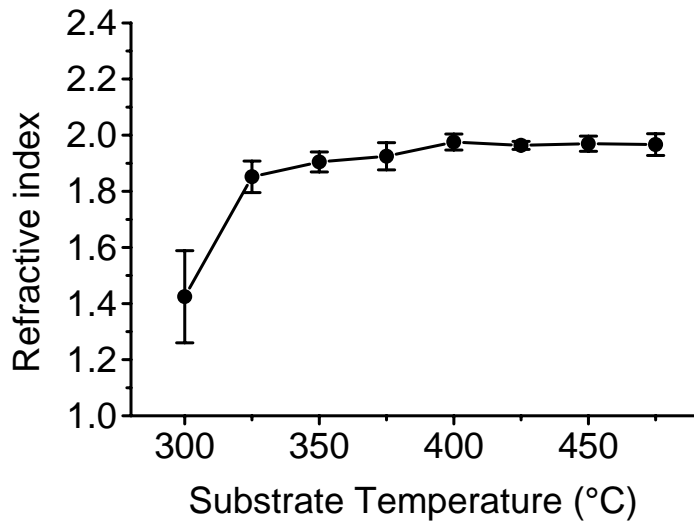


Figure 5: Average refractive indexes and standard deviations of ZrO<sub>2</sub> samples deposited at different temperatures. The refractive indexes were extracted by the Cauchy model at 1.96 eV.

### **3.2.4 Film Topology**

Topographic images were obtained from samples using a Digital Instruments' Nanoscope IIIa atomic force microscope (AFM) with etched silicon probes. Images of  $2.5 \times 2.5 \mu\text{m}$  areas with 512-line resolution were used to evaluate the surface-roughness of these samples. Before calculating surface-roughness data, a two-step image processing procedure was applied, consisting of a plane fit and a first-order flattening.

### **3.2.5 Transmission Electron Microscopy (TEM)**

Cross sectional TEM was used to evaluate the microstructure of the layers. TEM samples were prepared using a focused ion-beam (FIB) technique. Samples were prepared by mechanical polishing down to  $10 \mu\text{m}$  thickness, followed by FIB thinning of the area-of-interest down to electron transparency. A Philips CM200 transmission electron microscope with a twin-lens configuration was used for analysis. The instrument was operated at 200 kV. High-resolution TEM images were obtained with sample interfaces parallel to the direction of the beam.

## **3.3 AFM and TEM Results**

Figure 6 shows a representative top-view AFM image of the  $\text{ZrO}_2$  samples in this work. Grain sizes were similar among different samples. The measured surface-roughness values are presented in Table 2. Note that the  $R_{\text{MS}}$  value from AFM and the surface-roughness layer thickness in ellipsometric models have different definitions (Figure 7). In AFM data processing, a zero plane, which is located between the peaks and

valleys, is first fit. The height difference from this zero plain is defined as Z. The  $R_{MS}$  is calculated from

$$R_{MS} = \sqrt{\frac{(Z_1^2 + Z_2^2 + Z_3^2 + \dots + Z_N^2)}{N}} \quad (3.1)$$

However, in ellipsometry, the surface-roughness layer is defined as a layer that consists of 50% material and 50% void space. Hence,  $R_{MS}$  is approximately half of the surface-roughness layer thickness in ellipsometry. Values of two times  $R_{MS}$  were used as the reference values to compare with the surface-roughness layer thickness values extracted from ellipsometric data.

Figure 8 shows representative cross-section TEM images from the samples. Lattice fringe edges and contrast differences were used to define the top and bottom surfaces of the interfacial layers. The distance between these two surfaces was defined as the thickness of the interfacial layer. The distance between the top of the interfacial layer and the bottom of the valleys on the  $ZrO_2$  top surface was defined as the thickness of the  $ZrO_2$  layer. The measured thickness values are listed in Table 2. TEM was not used for surface-roughness measurements because of the low contrast top surface and the narrow field-of-view of TEM images.

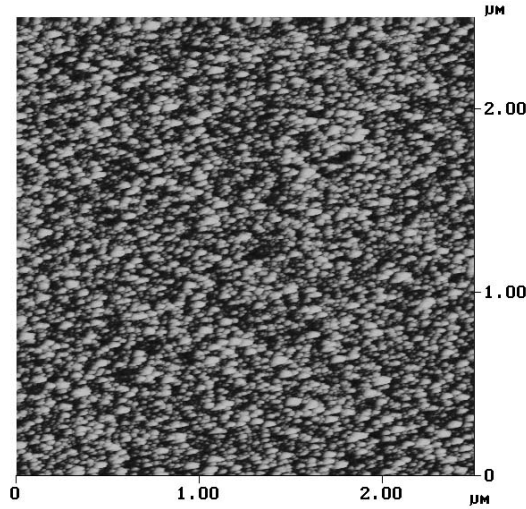


Figure 6: A  $2.5 \mu\text{m} \times 2.5 \mu\text{m}$  top view AFM image of Sample S07-07. The height scale was 10 nm.

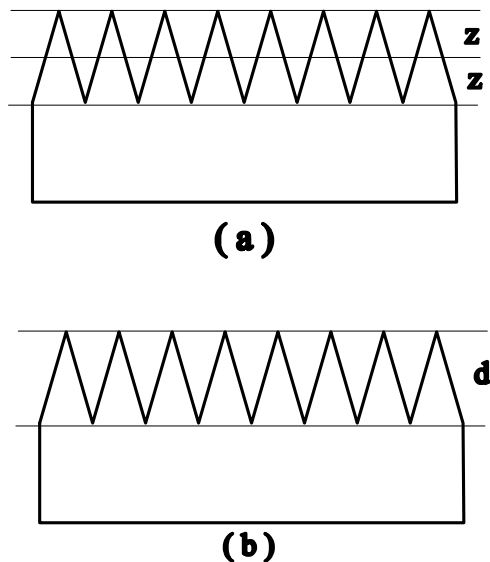


Figure 7: The definitions of RMS (a) and the surface roughness layer thickness (b)

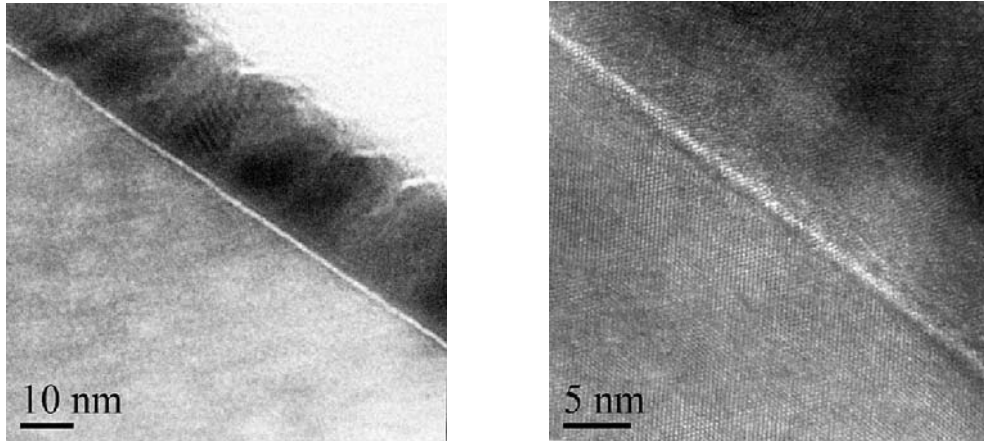


Figure 8: Cross sectional TEM images of Sample S07-08 at different magnifications.

Table 2: Combined thickness results from AFM and TEM

Samples	AFM		TEM	
	$R_{MS}$ (Å)	SR (Å)	$ZrO_2$ (Å)	Interfacial Layer (Å)
S07-07	22.3	44.5	203	23
S07-08	17.2	34.3	200	21
S07-09	13.2	26.5	190	19
S07-16	21.1	42.1	208	*
S07-24	16.5	32.9	165	22
S08-07	19.5	39.0	174	*

\* TEM results from these samples were inconclusive

### 3.4 Ellipsometry Data Analysis Results

When one extracts optical constants of very thin layers, correlation problems among fitting parameters often prevent extraction of a unique set of solutions for the parameters. MS-VASE methodology was used to minimize these possible correlation problems<sup>112,113</sup>. In using MS-VASE data analysis, experimental data from multiple samples were simultaneously loaded into the WVASE software. A single set of dispersion model parameters was used for each layer, to fit experimental data from all of the samples. This resulted in a single set of optical constants extracted for all of the

samples. The shapes of spectra generated by models were in good agreement with experimental data. We therefore used the mean squared error (MSE) value, based on Levenberg-Marquardt algorithm, as a measure of the quality-of-fit<sup>113</sup>. The best-fit results minimized MSE.

Ellipsometric characterization requires both an appropriate model for the layer stack structure, as well as appropriate optical constants or dispersion models for each layer. TEM and AFM results (Table 2) showed that thicknesses of the surface-roughness layers could be 10 - 20% of the total film thickness. Therefore, the contribution from surface-roughness cannot be neglected. At the same time, TEM images showed that interfacial layers were present between  $\text{ZrO}_2$  and silicon substrate. Based on these results, we built a three-layer model to simulate the  $\text{ZrO}_2$  films (Figure 9). A Bruggeman EMA layer<sup>110</sup>, defined as 50 % void space and 50 %  $\text{ZrO}_2$ , was used to simulate the top surface-roughness layer. The optical constants of the  $\text{ZrO}_2$  component in the EMA layer were coupled to those of the bulk  $\text{ZrO}_2$  layer.

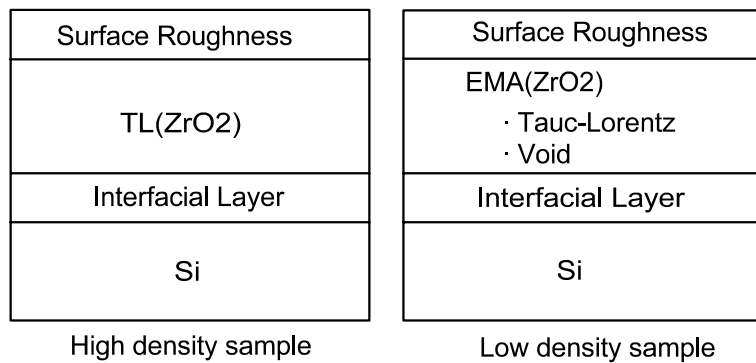


Figure 9: Models for MS-VASE data analysis. An EMA layer consisting of  $\text{ZrO}_2$  and void space was used to adjust the density difference for samples of lower densities.

In contrast to  $\text{SiO}_2$ , whose band gap (8.0 eV) is beyond the photon energy range of common spectroscopic ellipsometer (<6.0 eV),  $\text{ZrO}_2$  has a band gap of 5.0 - 5.6 eV<sup>58,114</sup>. This means  $\text{ZrO}_2$  is not fully transparent in the photon energy range of the ellipsometer used. Dispersion models for  $\text{SiO}_2$  layers, such as the Cauchy model, and the Sellmeier model cannot adequately describe  $\text{ZrO}_2$  films in the photon energy range of this work. A dispersion model capable of describing the interband absorption of thin films is essential for data analysis. We adopted the widely accepted TL model<sup>106,115-118</sup> to represent the dielectric function ( $\varepsilon = \varepsilon_1 + i\varepsilon_2$ ) of  $\text{ZrO}_2$  films in the expression

$$\varepsilon_2(E) = \begin{cases} \frac{AE_0C(E - E_g)^2}{(E^2 - E_0^2)^2 + C^2E^2} \frac{1}{E} & (E > E_g) \\ 0 & (E \leq E_g) \end{cases} \quad (3.2)$$

$$\varepsilon_1(E) = \varepsilon_\infty + \frac{2}{\pi} P \int_{E_g}^{\infty} \frac{\xi \varepsilon_2(\xi)}{\xi^2 - E^2} d\xi \quad (3.3)$$

where,  $E_g$  is the band gap,  $E_0$  is the peak transition energy,  $A$  is the amplitude,  $C$  is a broadening term, and  $\varepsilon_\infty$  is an offset. The TL model is applicable at photon energies slightly higher than the band gap of thin films. However, Jellison reported that the error in the peak transition energy,  $E_0$ , can be higher if  $E_0$  is not within the available photon energy range<sup>115</sup>. Therefore, spectra in a broader photon energy range will help extract accurate values. Additionally, samples deposited at different conditions can have different optical constants due to density differences<sup>119</sup>. In order to account for this effect, we used a TL layer to model the highest density  $\text{ZrO}_2$  film, in MS-VASE, and used the EMA model composed of high-density  $\text{ZrO}_2$  and void space to model  $\text{ZrO}_2$  films of lower densities. We used TL( $\text{ZrO}_2$ ) and EMA( $\text{ZrO}_2$ ) to represent the high-density  $\text{ZrO}_2$  layer

and low-density  $\text{ZrO}_2$  layers, respectively. During MS-VASE data analysis, the optical constants of  $\text{ZrO}_2$  in the EMA( $\text{ZrO}_2$ ) model were coupled to the TL( $\text{ZrO}_2$ ) layer, and void-space percentages were used as fitting parameters.

Accurate optical constants for the silicon substrate are also necessary for proper analyses. Therefore, we carefully examined the optical constants of silicon surfaces in comparison with published data. We collected ellipsometry data in the photon-energy range of 1.2 to 6.5 eV from four bare silicon samples after a pre-deposition cleaning procedure. We used the parametric semiconductor model to fit experimental data using the MS-VASE methodology<sup>112</sup>. Our experimental data agrees well with published data<sup>112</sup>, with the exception of a 6 - 7 Å surface-roughness layer present on our samples. This value is within the error of general cleaning experiments. In the process of comparing models and results, we used published data that was stated in a broad photon energy range from 0.2 to 6.6 eV<sup>112</sup>.

Previously, researchers used an EMA layer or the optical constants of  $\text{SiO}_2$  to simulate the interfacial layer<sup>108</sup>. However, no work concerning the modeling of the interfacial layer between high-k dielectric layers and silicon substrate appears to have been reported. How to properly model the optical constants of the interfacial layer is the major goal of this chapter.

### **3.4.1 Data of Silicon Oxide to Simulate the Interfacial Layers**

Due to the complexity of the interfacial layer properties, researchers often assume an interfacial  $\text{SiO}_2$  layer or an EMA layer to represent the interfacial layer<sup>63,106,108</sup>. Based on this assumption, thickness values or optical constants of  $\text{ZrO}_2$  layer were extracted.

We started data processing by using published optical constants of silicon oxides at different oxidation states. These silicon oxides include thermal silicon dioxide ( $\text{SiO}_2$ )<sup>120</sup>, silicon suboxide ( $\text{SiO}_x$ )<sup>120</sup>, native silicon oxide (NO-1)<sup>112</sup>, and an interfacial layer between  $\text{SiO}_2$  and Si (NO-2)<sup>112</sup>.

We used void-space percentages in the EMA( $\text{ZrO}_2$ ) layer to account for film density differences among different  $\text{ZrO}_2$  layers. Some of the resulting void-space percentage values turned out to be negative depending on which sample was defined as the highest density sample. We were unable to determine a unique highest-density sample in the sample set by fitting the void-space percentage in the EMA( $\text{ZrO}_2$ ) layer. Since the deposition conditions of these samples were similar, we assumed that all the  $\text{ZrO}_2$  layers had the same density, and set the void-space fraction for low-density  $\text{ZrO}_2$  layers to be zero. When  $\text{SiO}_x$ ,  $\text{SiO}_2$ , NO-1 and NO-2 were used to represent the interfacial layer, the MSE values of the best fits were 21.92, 19.62, 18.76, and 18.80 respectively. The extracted band gap of  $\text{ZrO}_2$  was 5.31 - 5.34 eV, and the extracted peak-transition energy was 5.70 to 5.82 eV. The optical constants of the  $\text{ZrO}_2$  layer are plotted in Figure 10, and thickness values extracted from these models are plotted in Figure 11.

### 3.4.2 The EMA Model to Simulate the Interfacial Layers

The EMA model is often used to simulate a small amount of interfacial intermixing between different phases or layers<sup>110</sup>. By adjusting the fractions of each component, the EMA model can generate the optical constants of the intermixing layer by weighting the ratio of its components. Since the interfacial layer can be assumed to be an intermixing layer between Si and  $\text{ZrO}_2$ ,  $\text{SiO}_x$  and  $\text{ZrO}_2$ , or  $\text{SiO}_2$  and  $\text{ZrO}_2$ , we used all

three of these binary combinations in data processing, and set the thickness values, the ratios between the EMA layer components, and the parameters in the TL model as fitting parameters. EMA(Si-ZrO<sub>2</sub>), EMA(SiO<sub>x</sub>-ZrO<sub>2</sub>), and EMA(SiO<sub>2</sub>-ZrO<sub>2</sub>) were used to represent the interfacial layers of different combinations. The best-fit MSE results were 18.82, 18.60, and 18.36 respectively when EMA(Si-ZrO<sub>2</sub>), EMA(SiO<sub>x</sub>-ZrO<sub>2</sub>), and EMA(SiO<sub>2</sub>-ZrO<sub>2</sub>) were used to represent the interfacial layer. Extracted compositions of the interfacial layer were Si:ZrO<sub>2</sub> = 3.7:96.3, SiO<sub>x</sub>:ZrO<sub>2</sub> = 17.5:82.5, and SiO<sub>2</sub>:ZrO<sub>2</sub> = 36.0:64.0. Figure 12 shows the optical constants of these binary compositions, and Figure 13 shows the extracted optical constants of the ZrO<sub>2</sub> layer. The thicknesses of each layer of these samples are plotted in Figure 14.

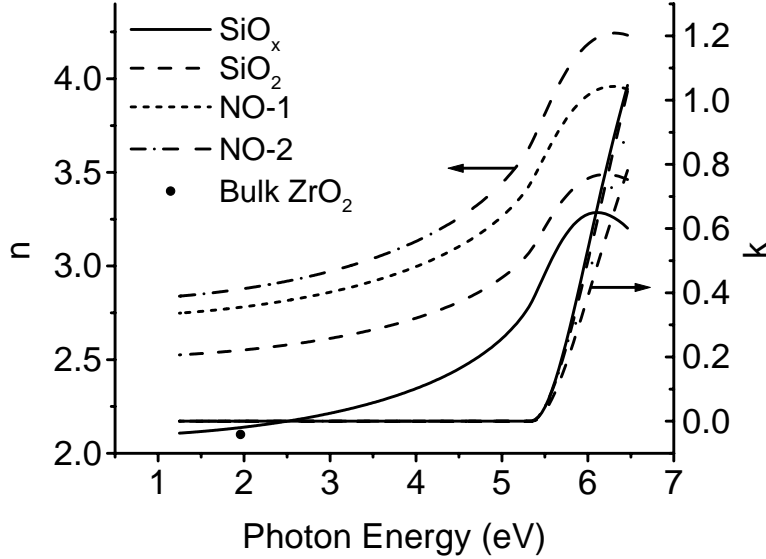


Figure 10: The extracted optical constants of the ZrO<sub>2</sub> layer when silicon oxides were used to simulate the interfacial layer.

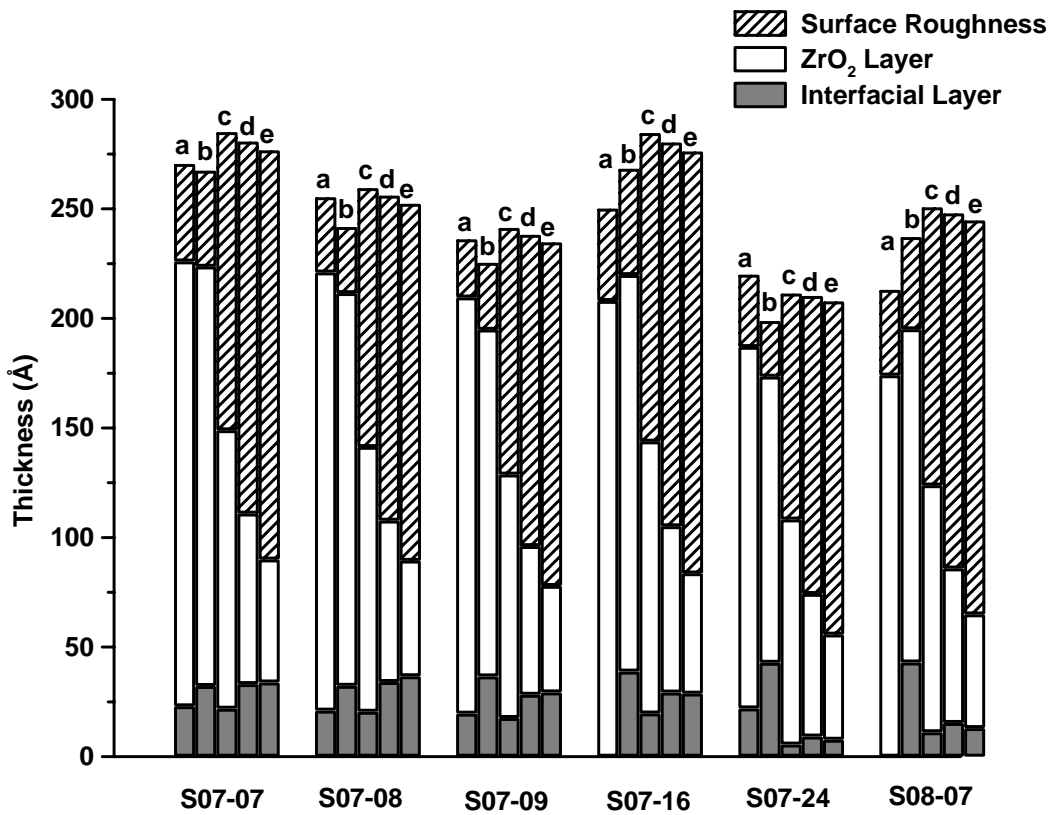


Figure 11: SE thickness results compared with (a) AFM-TEM results, when (b) SiO<sub>x</sub>, (c) SiO<sub>2</sub>, (d) NO-1, and (e) NO-2 were used to simulate the interfacial layer.

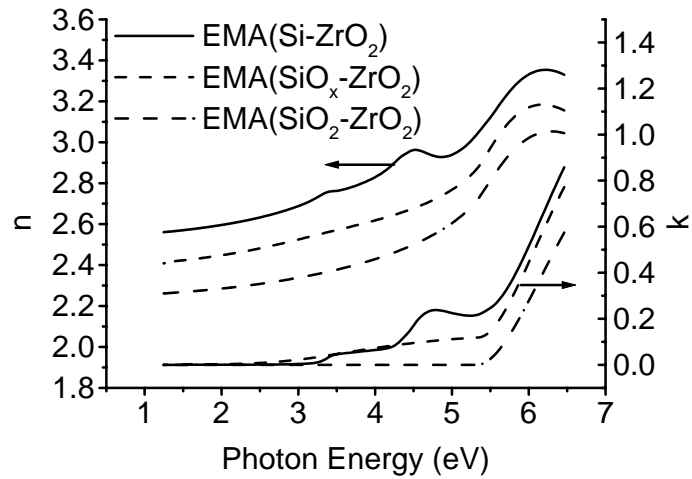


Figure 12: The optical constants of the interfacial layer extracted from different EMA models.

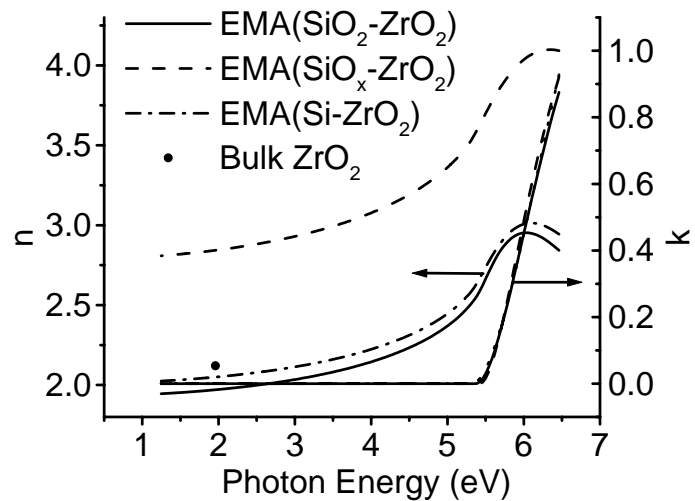


Figure 13: The extracted optical constants of ZrO<sub>2</sub> layer when different EMA layers were used to simulate the interfacial layer.

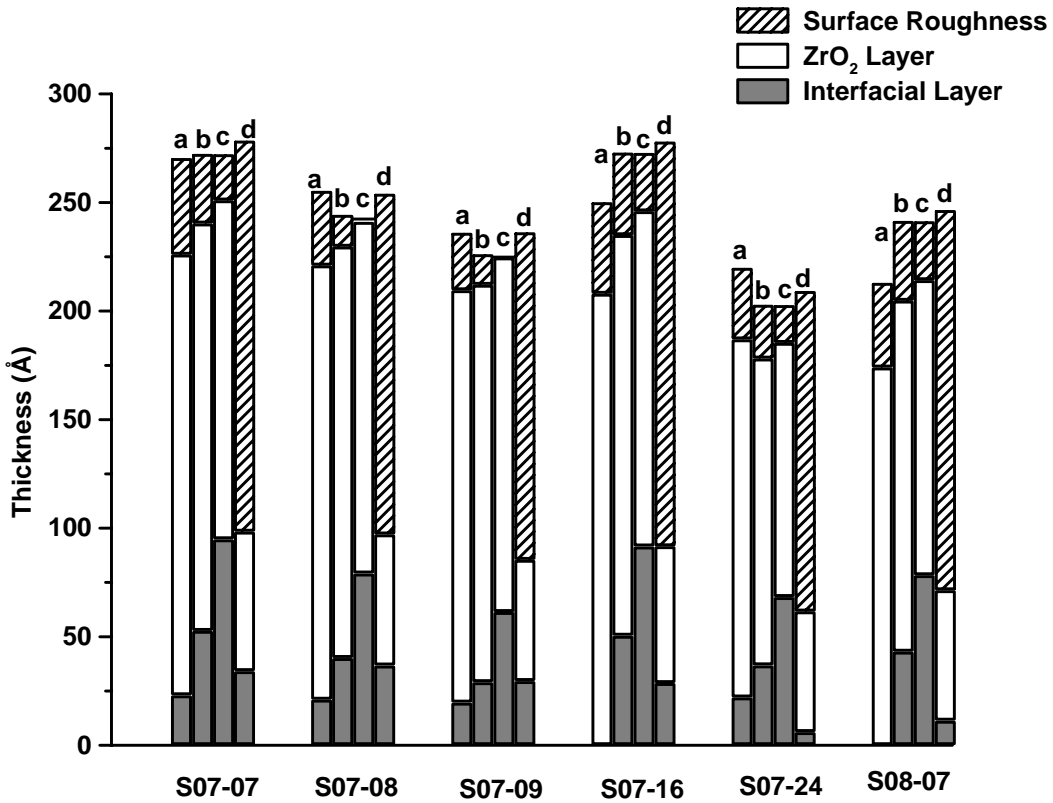


Figure 14: SE thickness results compared with (a) AFM-TEM results, when (b) EMA(Si-ZrO<sub>2</sub>), (c) EMA(SiO<sub>x</sub>-ZrO<sub>2</sub>), and (d) EMA(SiO<sub>2</sub>-ZrO<sub>2</sub>) were used to simulate the interfacial layer.

### 3.4.3 Dispersion Models to Simulate the Interfacial Layers

When optical constants of specific materials are used for ellipsometry data analysis, one has to realize that the optical constants of the sample under investigation may not be the same as published data. Sample preparation methods and preparation conditions can influence the optical properties of films. Dispersion models are often used in SE data analysis to account for this variation by adjusting dispersion model parameters. By choosing an appropriate dispersion model, and fitting the parameters in the model, including thicknesses of the layers and dispersion model parameters, the thicknesses and optical constants of the layers can be determined simultaneously.

In order to choose an appropriate dispersion model, it is necessary to know the characteristics of the interfacial layer. Since the band gaps of silicon and bulk ZrO<sub>2</sub> are 1.1 and 5.6 eV respectively, both the silicon substrate and the ZrO<sub>2</sub> are absorptive in the photon energy range of this study (1.2 to 6.5 eV). It is likely that the interfacial layer has absorptions within this photon energy range as well. Therefore, we used both the Lorentz and the TL models to simulate the interfacial layer. These were symbolized by L(IL) and TL(IL). The TL model assumes that the interband transition is the only available transition in the photon energy range, whereas the Lorentz model assumes that multiple transitions can be observed in the photon energy range under investigation. We used the Lorentz model with the expression,

$$\varepsilon = \varepsilon_1 + i\varepsilon_2 = \varepsilon_\infty + \sum_k \frac{A_k}{E_{0,k}^2 - E^2 - iC_k E} \quad (3.4)$$

where for the k<sup>th</sup> oscillator, A<sub>k</sub> is the amplitude, E<sub>0,k</sub> is the center energy, C<sub>k</sub> is the broadening of each oscillator, and ε<sub>∞</sub> is an offset. Note that each Lorentz oscillator has three parameters. Due to the ultra-thin nature of interfacial layers, strong correlation among model parameters can occur if too many oscillators are used in data processing. Therefore, we used a Lorentz model composed of up to two Lorentz oscillators to extract the optical constants of the interfacial layer. Even with this very limited number of Lorentz oscillators, the Lorentz model is no longer sensitive to the band gap of the materials, so we set the band gap value to be zero. All thickness values, and dispersion model parameters were used as fitting parameters.

We obtained 50% lower MSE values by using dispersion models to simulate the interfacial layer compared with using tabulated optical constants or the EMA models. In

order to improve the fit quality, void-space percentages in the EMA( $\text{ZrO}_2$ ) layer were also set as fitting parameters to account for small density differences among the samples. When two Lorentz oscillators were used in data processing, we experienced strong correlation problems. Only the parameters for one oscillator, centered at 6.1 eV, could be decorrelated. The parameters of the other oscillator could not be uniquely determined, so we only show one possible set of values for the dual Lorentz oscillator model (LL(IL)). The extracted dispersion model parameters are listed in Table 3. Optical constants of the  $\text{ZrO}_2$  and interfacial layers are plotted in Figure 15 and Figure 16. Thicknesses for all the layers, extracted from different models, are plotted in Figure 17.

Additionally, the Sellmeier model has been used to simulate the interfacial layer between thermal  $\text{SiO}_2$  and silicon substrate<sup>112</sup>. However, the quality of data fit obtained by using the Sellmeier model was much lower than other models in this work. We show extracted thickness values in Figure 17, and skip other results extracted from this model.

### 3.5 Discussion

The presence of an interfacial layer between  $\text{ZrO}_2$  and Si has been reported by multiple researchers<sup>6-12</sup>. Although this interfacial layer was often identified as silicon oxide, the real chemical composition varies from  $\text{SiO}_2$  to zirconium silicate, depending on deposition method and conditions. When excessive oxidation of the silicon substrate occurs either during deposition or during post-deposition annealing, a distinct interfacial  $\text{SiO}_2$  layer can form. When the deposition process is carefully controlled, the interfacial layer is an alloy between  $\text{ZrO}_2$  and silicon oxide, or zirconium silicate. Due to bonding and lattice mismatch between  $\text{ZrO}_2$  and silicon, these layers have a high density of

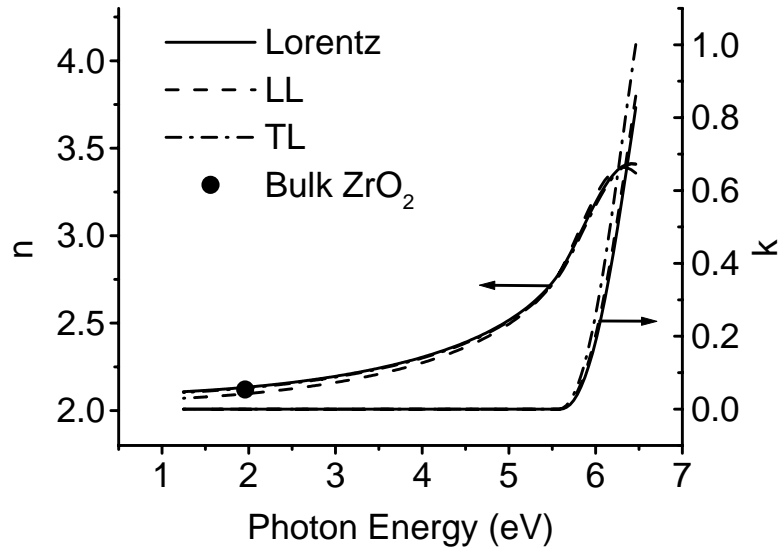


Figure 15: The optical constants of  $\text{ZrO}_2$  when dispersion models were used to simulate the interfacial layer.

Table 3: Extracted optical constant parameters for the interfacial layer and the  $\text{ZrO}_2$  layer by using dispersion model to simulate the interfacial layer.

Interfacial layer model		TL	Single Lorenz	Dual Lorenz
Interfacial layer model parameters (eV)	$\epsilon_\infty$	4.656	4.217	4.071
	$E_g$	2.395	-	-
	A	69.65	49.24	37.56
	$E_0$	6.218	6.220	6.213
	C	0.6248	0.5903	0.6433
TL( $\text{ZrO}_2$ ) layer parameters (eV)	$\epsilon_\infty$	1.375	1.424	1.307
	$E_g$	5.595	5.576	5.576
	A	592.8	581.3	644.0
	$E_0$	6.502	6.491	6.346
	C	1.898	1.858	1.740
MSE		11.63	11.52	10.66

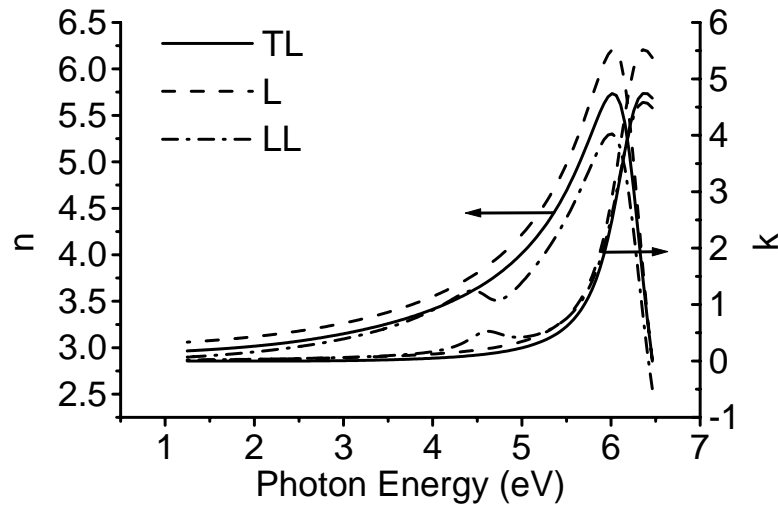


Figure 16: The optical constants of the interfacial layer extracted from different dispersion models.

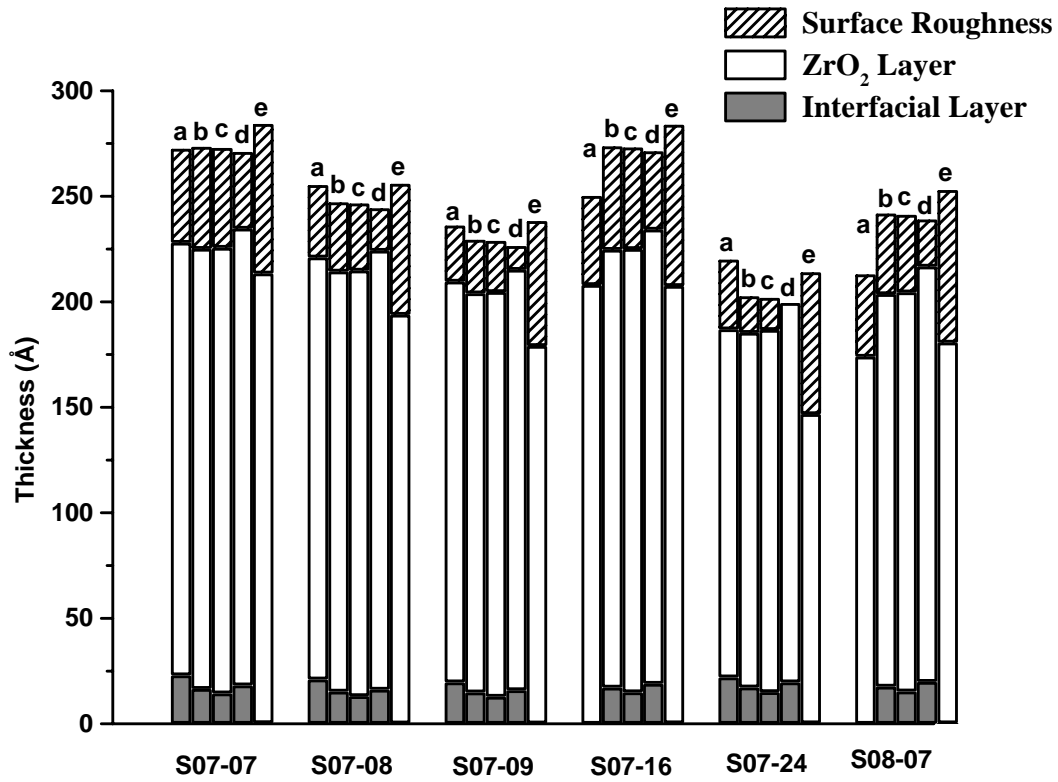


Figure 17: SE thickness results compared with (a) AFM-TEM results, when (b) TL, (c) single Lorentz oscillator, (d) dual Lorentz oscillator, and (e) the Sellmeier model were used to simulate the interfacial layer.

unsaturated dangling bonds<sup>41,42</sup>. The band gap of the interfacial layer is expected to be significantly lower than that of the ZrO<sub>2</sub> layer due to states generated by the dangling bonds within the band gap. If the interfacial layer is neglected in data processing, or the optical constant of high quality dielectric material ( $k=0$  throughout the spectrum), is used to represent the interfacial layer, the extracted TL model parameters for the ZrO<sub>2</sub> layer represent a combined contribution from both the interfacial and the ZrO<sub>2</sub> layers. The optical constants of the layers are not decorrelated, even though mathematically the correlation coefficient matrix indicates that they are decorrelated. In order to characterize both thickness and properties of the stacked structure, the optical constants of the interfacial layer must be separated from that of the ZrO<sub>2</sub> layer.

We started data processing by using a variety of silicon oxides with various oxidation states to represent the interfacial layer. SiO<sub>2</sub> has the highest oxidation state in the group. The native silicon oxides are mixtures of SiO<sub>2</sub> and suboxides. When different silicon oxides were used to simulate the interfacial layer, the MSE values were not significantly different. The TL model parameters were decorrelated. However, when SiO<sub>2</sub> and native silicon oxides were used to represent the interfacial layer, the extracted surface-roughness layer thicknesses were three to five times higher than TEM and AFM results (Figure 11). Furthermore, the refractive indexes of the ZrO<sub>2</sub> layer were all higher than that of bulk ZrO<sub>2</sub><sup>58</sup> (Figure 10). Therefore, using either SiO<sub>2</sub> or native-silicon oxide optical constants, to represent the interfacial layer between ZrO<sub>2</sub> and silicon substrate, results in inaccurate and nonphysical characterization of the samples.

The interfacial layer between silicon and ZrO<sub>2</sub> can be interpreted in terms of intermixing between SiO<sub>2</sub> and ZrO<sub>2</sub>, SiO and ZrO<sub>2</sub>, or Si and ZrO<sub>2</sub>. Hence, we used the

EMA model with all three of these binary material combinations to simulate the interfacial layer. Similar MSE values resulted, indicating that the goodness of these fits was similar. However, thickness values from the different models were significantly different from one another (Figure 14). When EMA(SiO<sub>2</sub>-ZrO<sub>2</sub>) was used, the resulting surface-roughness values accounted for more than 50% of the total film thickness, while the thickness values of the ZrO<sub>2</sub> layer were only 30-40% of those determined by TEM. The resulting refractive index of the ZrO<sub>2</sub> layer was 1.5 times higher than the published values for bulk ZrO<sub>2</sub>. This suggests that the EMA(SiO<sub>2</sub>-ZrO<sub>2</sub>) model is not sufficient to represent the interfacial layer (Figure 13). When the EMA(SiO<sub>x</sub>-ZrO<sub>2</sub>) model was used, the data fit stopped with singular value problems, so the E<sub>g</sub> value and the E<sub>n</sub> value were the same. Nevertheless, the results from the EMA(SiO<sub>x</sub>-ZrO<sub>2</sub>) model were closer to AFM/TEM results, and published data (Figure 13 and Figure 14). The EMA(Si-ZrO<sub>2</sub>) model provides the best results in this group. When the EMA(Si-ZrO<sub>2</sub>) model was used, the thickness values were comparable to TEM and AFM results (Figure 13 and Figure 14), though the interfacial layer thickness values were 1.5-3 times higher than TEM results.

Due to extinction coefficient differences among Si, SiO and SiO<sub>2</sub>, the extinction coefficient spectra, k, of the interfacial layer had different shapes (Figure 12). However, the overall shapes of the optical constant spectra were similar (Figure 12). The refractive index of the interfacial layer at 1.96 eV is higher than that of bulk ZrO<sub>2</sub> by 0.2 – 0.5, and the band gap of the interfacial layer was lower than 1.4 eV, which is much lower than the band gap of 5.3 -5.4 eV for ZrO<sub>2</sub> (Figure 13). This agrees with the high-level unsaturated dangling bond characteristics of the interfacial layer. The refractive indexes of the ZrO<sub>2</sub>

layer extracted using Si-ZrO<sub>2</sub> and SiO<sub>x</sub>-ZrO<sub>2</sub> combinations, were lower than published data by 0.1 – 0.2. This could be caused either by film properties, such as lower densities or impurities in the film, or the models themselves.

We used three dispersion models to represent the interfacial layer. Dispersion models are used to describe the optical constants of different materials. The Sellmeier model is a typical model for dielectric materials that do not have absorptions in the spectrum. The TL model describes samples having one interband transition in the spectrum; and the Lorentz model depicts materials having multiple absorptions in the spectrum.

When the TL model or the Lorentz model was used to simulate the interfacial layer, the MSE values of these fits were 50% lower than those from other model-fits in this work. Thickness values extracted from these two models were almost identical to AFM and TEM results. The optical constants of ZrO<sub>2</sub> extracted from these two models were almost identical (Table 3). Since the interfacial layer was carefully separated from the ZrO<sub>2</sub> layer, interfacial effects were not incorporated into the ZrO<sub>2</sub> layer, and the extracted band gap value is higher than that published by Diebold<sup>106</sup>. The band gap of the ZrO<sub>2</sub> layer is 5.6 eV, which is identical to results obtained by other methods<sup>114</sup>, while the peak transition energy of ZrO<sub>2</sub> is 6.5 eV, which is on the edge of the photon energy range of our ellipsometer. The corresponding refractive index of the ZrO<sub>2</sub> layer at 1.96 eV is 2.12<sup>58</sup>, which is identical to published data. Therefore, the TL parameters in Table 3 accurately depict the optical constants of the ZrO<sub>2</sub> layer. Figure 16 shows the slight differences among the interfacial layer optical constants extracted from different dispersion models.

A single Lorentz model can seldom simulate the optical constants of real materials<sup>107</sup>. When we used two or more Lorentz oscillators to simulate the interfacial layer, strong correlation problems occurred due to the ultra-thin nature of the interfacial layer. Therefore, no unique best-fit solution could be obtained. In addition, the Lorentz model is not sensitive to the band gap, so the determination of the band gap value was arbitrary. All these points could be potential problems if the Lorentz model was used to simulate the interfacial layer. However, possibly due to the ultra-thin nature of the interfacial layer, these complications did not significantly affect the results.

Compared with the single oscillator Lorentz model, the TL model has one more parameter, the band gap. Since the band gap value was uniquely extracted from experimental data, the TL model provides a better description of the optical constants of the interfacial layer. The refractive index of the interfacial layer extracted from our samples is 3.0 at 1.96 eV, which is much higher than SiO<sub>2</sub> (1.5), SiO<sub>x</sub> (1.96), ZrO<sub>2</sub> (2.1), and ZrSiO<sub>4</sub> (1.92 - 1.97), and closer to silicon (3.47).

### 3.6 Conclusion

We have demonstrated that proper modeling of the optical properties of the interfacial layer is the key to accurate ellipsometric characterization of ZrO<sub>2</sub> films. Based on a stacking model consisting of an EMA surface-roughness layer, a TL layer to represent the ZrO<sub>2</sub> layer, and a second TL layer to represent the interfacial layer, we extract the thickness of each layer in the three-layer stack structure. The extracted thickness and effective surface-roughness values were in good agreement with AFM and TEM results. We separated the optical constants of ZrO<sub>2</sub> from those of the interfacial

layer, and uniquely extracted TL parameters to depict the optical constants of  $\text{ZrO}_2$ , which were consistent with published data. We also extracted the optical constants of the interfacial layer from  $\text{ZrO}_2$  samples deposited by HV-CVD under tight environment control. The optical constants of the interfacial layer suggest that the interfacial layer is a non-stoichiometric zirconium silicate.

## CHAPTER IV

### IN-SITU ELLIPSOMETRY STUDY OF THE INITIAL STAGE DEPOSITION OF ZIRCONIA ON DIFFERENT SURFACES

#### 4.1 Background

The semiconductor industry has made remarkable progress in continuously providing microelectronic products of increasing performances and functionality. The progress was primarily based on continued scaling of MOSFET. However, new materials need to be used in order for this trend to continue. Replacing the  $\text{SiO}_2$  based gate dielectric with a high-k dielectric is one example of new material integration.

The semiconductor industry faces many challenges in integrating high-k dielectric materials into devices. Materials selection challenges have been well-reported<sup>5,30-33</sup>. In recent years, increasing attention has been focused on a few materials systems, including  $\text{ZrO}_2$  ( $k \sim 25$ , polycrystalline)<sup>35</sup>,  $\text{HfO}_2$  ( $k \sim 25$ , polycrystalline)<sup>35</sup>,  $\text{Al}_2\text{O}_3$  ( $k \sim 9$ , amorphous)<sup>35</sup>,  $\text{ZrAl}_x\text{O}_y$  ( $k = 12-20$ , amorphous)<sup>121</sup>,  $\text{HfAl}_x\text{O}_y$  ( $k = 12-15$ , amorphous)<sup>121</sup>,  $\text{ZrSiO}_4$  ( $k \sim 12.6$ )<sup>28</sup>, and  $\text{HfSi}_x\text{O}_y$  ( $k \sim 11$ , amorphous)<sup>28</sup>.

The deposition process for high-k materials presents a significant challenge. We have discussed these challenges in Section 2.2.2. The successful deposition process must produce films of uniform composition, microstructure, thickness and interface properties. Multiple processes have been used to deposit high-k materials, such as MOCVD<sup>23,60,62,97</sup>, ALCVD<sup>66-69</sup>, sputtering<sup>122</sup>, reactive sputtering<sup>111,123,124</sup>, and plasma enhanced chemical vapor deposition<sup>125</sup>.

Since MOCVD and ALCVD do not damage the silicon substrate surface, they are the most promising potential processes to deposit high-k films. However, both processes

begin with a transition period<sup>67,71,126</sup>, in which deposition rates change with time. Within this initial stage, the thickness of high-k films often reaches 40-50 Å. This means the process for depositing high-k films will have to be operated in an unsteady state, making the control of the deposition process difficult. In addition, researchers have discovered that the properties of ALCVD films within this thickness range, such as the structure and the chemistry, are strongly affected by the properties of starting surfaces<sup>66,67</sup>. The effects of starting surface properties during thermal chemical vapor deposition have not been reported. Details on the initial deposition of high-k dielectric materials are very important for successfully integrating high-k dielectric materials into MOSFET devices.

In this chapter, we will use in-situ SE to study the initial stage deposition behavior of ZrO<sub>2</sub> from ZTB on both H-terminate silicon (H-Si) surfaces and native silicon oxide surfaces during high vacuum metal organic vapor deposition (HV-MOCVD). By using HV-MOCVD, the deposition environment is tightly controlled. Since no oxidants, such as oxygen, or water vapor, are used, the oxidation of the silicon substrate is minimized. In contrast to ALCVD, HV-CVD is a continuous process, which enables us to study continuous film property evolution during the initial-stage deposition of ZrO<sub>2</sub>. The results show that ZrO<sub>2</sub> films deposited on different starting surfaces have different structures. The starting surface influences the deposition process by altering the nucleation and coalescence process. Compared with films deposited on H-Si surfaces, films deposited on native silicon oxide are more uniform and have higher densities. A detailed comprehensive investigation of the properties of ZrO<sub>2</sub> films deposited via HV-MOCVD will be addressed in Chapter V.

## 4.2 Experimental Details

The reaction precursor, ZTB, was introduced through the bottom of the deposition chamber. No carrier gas or other diluent gases were used in the deposition process. MOCVD of  $\text{ZrO}_2$  films from ZTB was preformed in a single wafer ultra high vacuum compatible CVD system (Figure 4). The deposition system was detailed in Section 3.2.1.

Three inch Si(100) wafers with resistivities between 1 and 10  $\Omega\cdot\text{cm}$  were used as substrates. Two different types of surfaces from these silicon substrates, native silicon oxide or H-terminated Si(100) (H-Si), were used as the starting surface. Silicon wafers with native silicon oxide layers were used directly from the box without further cleaning. H-Si surfaces were prepared by a 40 sec 1:50 HF-DI water dip, followed by a 150 sec DI-water rinse, and nitrogen drying. These H-Si substrates were promptly transferred into the CVD system after surface preparation.

In the deposition chamber, the substrate was first heated to the desired temperature with no flowing precursor. Once the temperature stabilized for approximately 5 minutes, a valve was opened to allow ZTB introduction. We stopped depositions when the thickness of  $\text{ZrO}_2$  films reached 200 Å as determined by in-situ SE monitoring.

The software EASE<sup>®</sup> (J.A. Woollam Company) was used for data collection and processing. Ellipsometric spectra were collected every two seconds during deposition. We used photon energies between 1.25 and 5.8 eV for data processing. The signal to noise level in photon energy range above 5.8 eV was not acceptable due to slight  $\text{ZrO}_2$  coatings on the two windows.

X-ray diffraction (XRD) scans were obtained using a Scintag X1  $\theta/\theta$  automated powder X-ray diffractometer. The diffractometer is equipped with a Cu target and a Peltier cooled solid-state detector. All  $\text{ZrO}_2$  samples were scanned in  $2\theta$  range  $20 - 60^\circ$  with a step size of  $0.05^\circ$  and a preset scan time of 9 seconds. The total scan time for each sample was 2 hours.

Topographic images were obtained from samples using a Digital Instruments' Nanoscope IIIa atomic force microscope (AFM) with etched silicon probes (SSS-NCH, from Nanosensors). Images of  $2.0 \times 2.0 \mu\text{m}$  areas with 512-line resolution were used to evaluate the surface-roughness of these samples. Before calculating surface-roughness data, a two-step image processing procedure was applied, consisting of a plane fit and a first-order flattening.

### 4.3 Results and Discussion

SE is a sensitive nondestructive method to characterize thin films. Based on measurements of two parameters,  $\Delta$  and  $\Psi$ , and using appropriate models, several important parameters, such as film thickness, surface roughness, and optical properties of the thin film, can be quickly extracted<sup>107</sup>. One of the difficulties for in-situ ellipsometry data analysis is that the optical constants at deposition temperatures are typically not available. Therefore, optical constants at room temperature are often used<sup>90</sup>. This will induce error in data analysis. Recent progress in SE and modeling enabled us to extract the optical constants directly from in-situ SE data. We show the results from XRD and AFM before discussing the extraction of optical constants of  $\text{ZrO}_2$  at deposition temperatures.

#### 4.3.1 XRD Results of 200 Å Samples

Figure 18 shows X-ray diffraction spectra from 200 Å thick ZrO<sub>2</sub> films deposited on H-Si. ZrO<sub>2</sub> films deposited on H-Si consist of the tetragonal phase only. We assign the diffraction peak at 30° to the tetragonal (100) face. The diffraction peak at 34.5° 2θ is the overlapping diffraction pattern of tetragonal (002) and (110) faces, while the peak at 50° 2θ is the joint contribution from tetragonal (112) and (200) faces. The intensity of these peaks decreases with increasing deposition temperatures. This suggests that films deposited at higher deposition temperatures have low crystallinity, and hence low long-range orders.

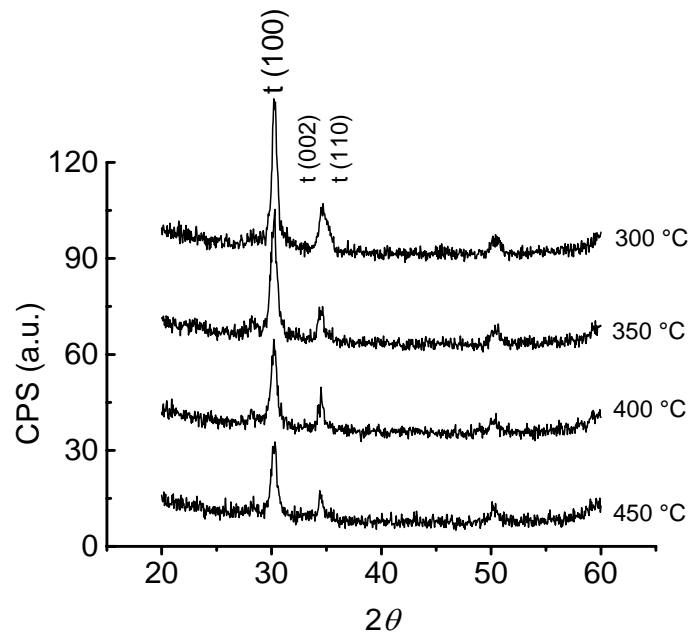


Figure 18: X-ray diffraction spectra of 200 Å ZrO<sub>2</sub> deposited on H-Si.

Figure 19 shows the X-ray diffraction spectra from 200 Å ZrO<sub>2</sub> films deposited on native silicon oxide surfaces. Most of the diffraction patterns show peaks at 28 and 30° 2θ. We assign the diffraction peak at 30° to the tetragonal (100) face, and the peak at 28° 2θ to the monoclinic (100) face. Therefore, most of the ZrO<sub>2</sub> films consist of both the tetragonal and monoclinic phases. However, a weak peak from the diffraction off the tetragonal (110) and (002) faces at 34.5° 2θ can only be observed when deposition temperatures are higher than 425 °C. Similar to samples deposited on H-Si surfaces, the intensity of the tetragonal (100) face decreases with increasing deposition temperatures in temperature range 325-450 °C. This suggests that the crystallinity of the tetragonal phase decreases with increasing temperatures.

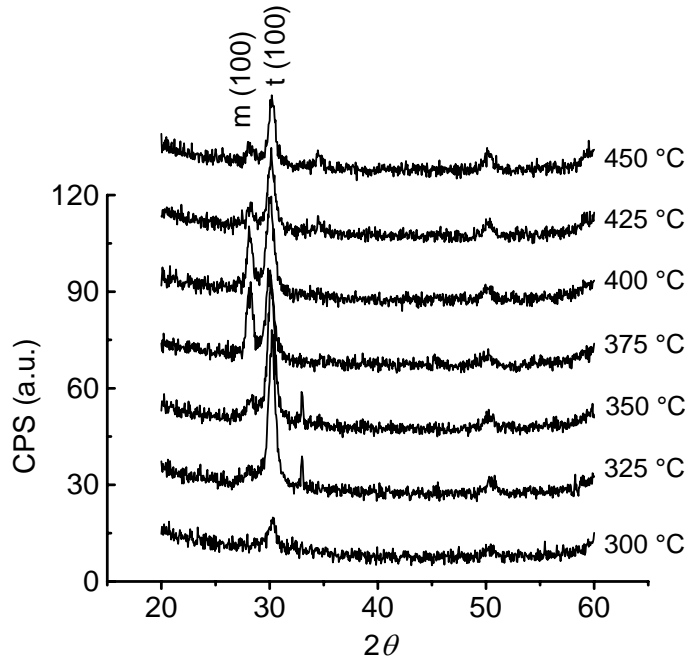


Figure 19: X-ray diffraction pattern of 200 Å ZrO<sub>2</sub> deposited on native silicon oxide

The intensity change of the monoclinic (100) peak is not monotonic. At deposition temperatures between 325 and 375 °C, the intensity of the monoclinic (100) peak increases with increasing depositions temperatures to a maximum intensity at 375 °C. The monoclinic (100) peak intensity decreases at temperatures higher than 375 °C. The phase change of ZrO<sub>2</sub> between monoclinic and tetragonal phases is beyond the scope of this study, and more information can be found in reference<sup>127</sup>.

The sample deposited at 300 °C on native silicon oxide is a special case. We do not detect the monoclinic phase in films deposited at this temperature. Additionally, the intensity of the tetragonal (100) face is much lower than that from samples deposited on native silicon oxide at 325 °C. This suggests that ZrO<sub>2</sub> has a different nucleation process on native silicon oxide at 300 °C.

#### 4.3.2 Film Topology

Figure 20 shows representative topology of ZrO<sub>2</sub> films at different thicknesses and temperatures. Figure 21 plots the surface roughness change with film thickness for samples deposited on different surfaces. On both surfaces, the film surface roughness increases with increasing film thickness. The surface roughness increase becomes smaller at higher deposition temperatures. This suggests lower deposition temperature facilitates surface roughness evolution. The properties of the starting surface influence the extent of surface roughness increase during initial-stage deposition. On native silicon oxide surfaces, when the film thickness increased from 30 to 60 Å the surface roughness increased by less than 1 Å. However, on H-Si surfaces, the surfaces roughness increased by more than 2 Å measured by AFM.

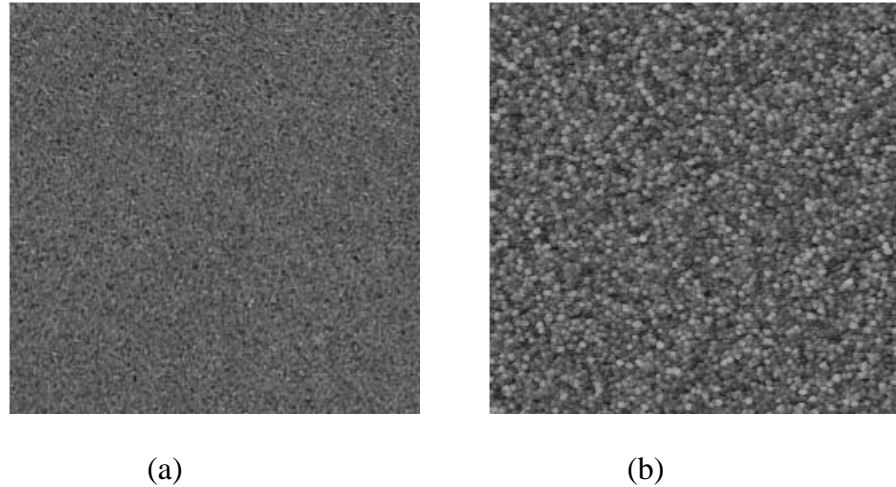


Figure 20:  $2\mu\text{m} \times 2\mu\text{m}$  AFM images of (a)  $30\text{ \AA}$  and (b)  $60\text{ \AA}$   $\text{ZrO}_2$  films deposited on H-Si surfaces at  $350\text{ }^\circ\text{C}$ .

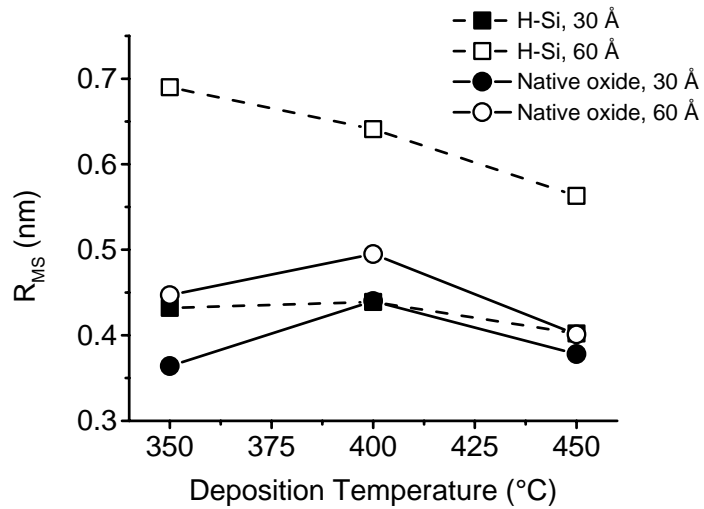


Figure 21: Surface roughness of  $\text{ZrO}_2$  films deposited on different surfaces and at different temperatures and thicknesses.

XRD results suggest that deposition on native silicon oxide at  $300\text{ }^\circ\text{C}$  is different from depositions at higher temperatures, so we stopped deposition at different thicknesses and scanned the topology of these surfaces. Figure 22 shows the surface image of  $\text{ZrO}_2$  deposited on native silicon oxide surfaces at  $300\text{ }^\circ\text{C}$ , and Figure 23 shows the surface

roughness increase during deposition. 3-D type nucleation started after the film is thicker than 15 Å, indicating a uniform ultra thin ZrO<sub>2</sub> film is formed before a 3-D nucleation process starts. During the following deposition process, the surface roughness increased continuously in the thickness range studied.

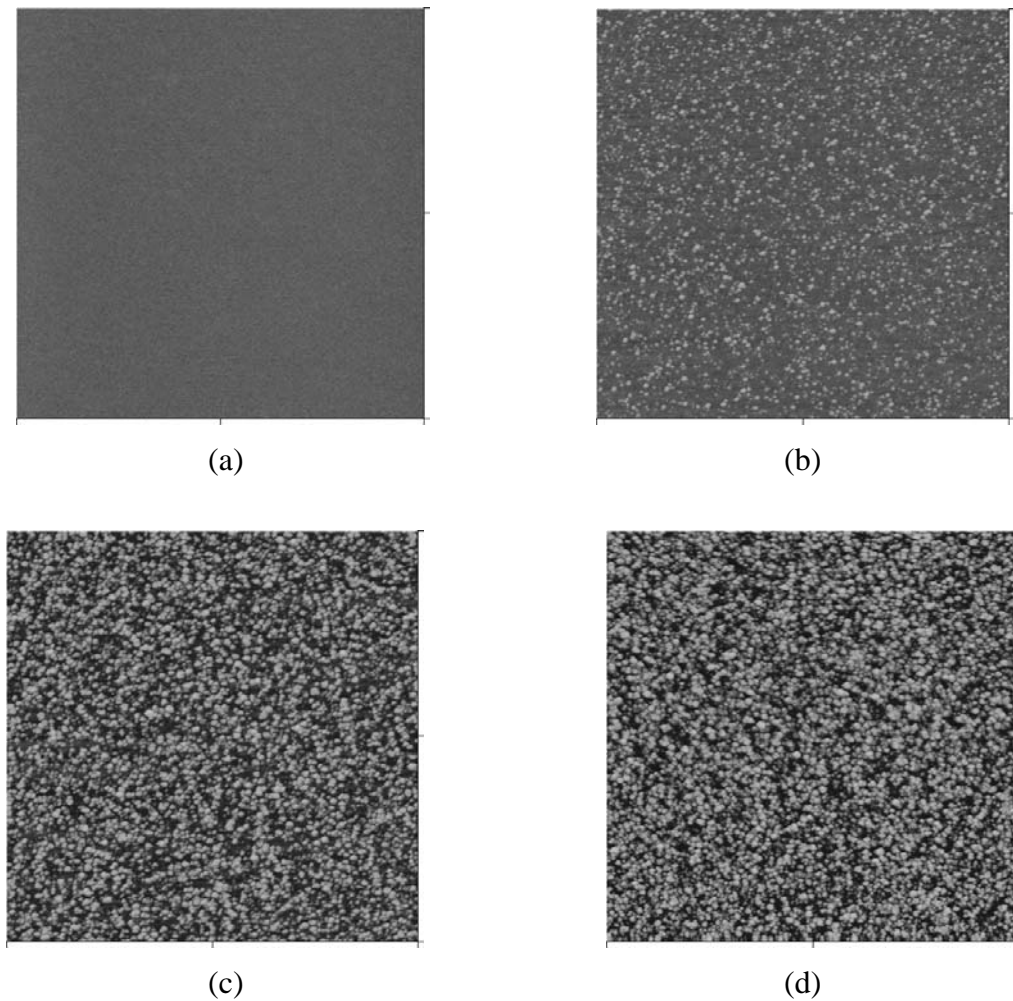


Figure 22: 2μm × 2μm AFM images of (a) 15 Å, (b) 30 Å, (c) 50 Å, and (d) 100 Å ZrO<sub>2</sub> films deposited on native silicon oxide at 300 °C.

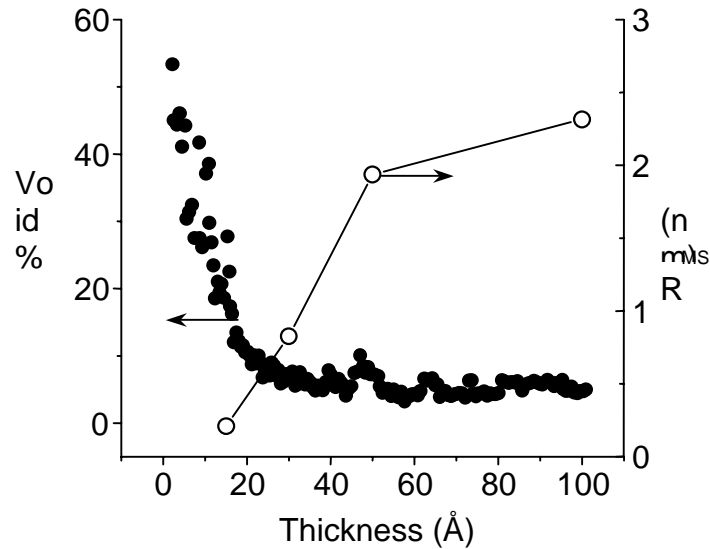


Figure 23: Surface roughness measured by AFM and void fractions measured by SE of  $\text{ZrO}_2$  films deposited on native silicon oxide surfaces at 300 °C and different thicknesses.

#### 4.3.3 Extraction of Refractive Indexes of $\text{ZrO}_2$

The XRD and AFM results showed topology, structure, and the crystallinity of deposited films. Both methods required significant time to collect experimental data, so neither of these two methods can be directly applied to real time process control. In-situ spectroscopic ellipsometry has been proven to be a powerful tool for real time process monitoring and control. However, SE models and data analysis need to be carefully developed.

Data processing was first conducted on the EASE software in dynamic mode data analyses <sup>128,129</sup>. Dynamic mode data analysis assumes: 1) available SE data were collected during steady state deposition, in which the deposition rate does not change with time; 2) the optical constants of the deposited film during steady state deposition do not change with increasing film thickness. A schematic of the initial-stage deposition and

the steady state deposition is plotted in Figure 24. In dynamic mode data processing, SE models are fitted simultaneously to hundreds of spectra collected during deposition. Difficulties in decorrelating parameters due to limited available experimental data in ex-situ SE analysis can often be successfully resolved, so the steady state deposition rates and the optical constants can be accurately extracted.

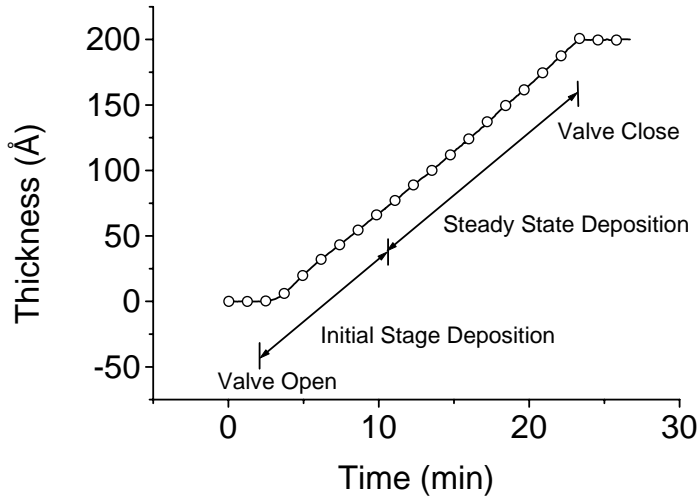
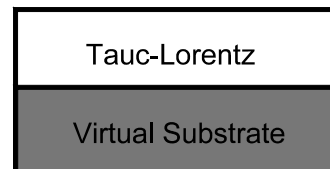


Figure 24: A schematics of deposition stages

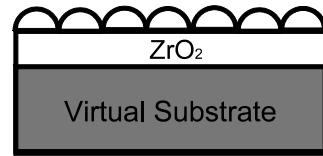
We first used a one layer ellipsometric model (Figure 25.a) consisting of one TL layer<sup>115</sup> on the top of a virtual substrate to extract the optical constants of deposited ZrO<sub>2</sub> films. Ellipsometric data collected from the starting surfaces after the desired substrate temperature was reached but before precursor introduction were used to represent the virtual substrate. We use ZrO<sub>2,H-Si</sub> to denote ZrO<sub>2</sub> films deposited on H-Si surfaces, and ZrO<sub>2,NO</sub> to denote the ZrO<sub>2</sub> films deposited in native silicon oxide surfaces. Figure 26 plots the pseudorefractive index spectra of 200 Å films deposited on the two starting surfaces at temperatures between 300 and 450 °C. We can see that the refractive indexes

of  $\text{ZrO}_2$  deposited on different surfaces and at different temperatures fall into three groups.  $\text{ZrO}_2$  films deposited on native silicon oxide surfaces at 300 °C have exceptionally low refractive indexes, while  $\text{ZrO}_2$  films deposited on native silicon oxide surfaces at higher temperatures between 325 and 450 °C have the highest refractive indexes.  $\text{ZrO}_2$  films deposited on H-Si surfaces have refractive indexes between these two groups of refractive indexes. Except for the special case of  $\text{ZrO}_2$  deposited on native silicon oxide at 300 °C, deposition temperatures used in this study appears to have a limited effect on a film's refractive index. Therefore, we ignore the temperature effect in the following data analysis.

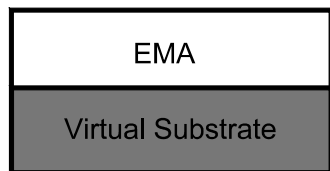
The structure of films can strongly affect the optical constants of these films. XRD results have shown that  $\text{ZrO}_2$  deposited on different surfaces have different structures.  $\text{ZrO}_2$  deposited on H-Si consists of only tetragonal phase, while at certain temperatures,  $\text{ZrO}_2$  deposited on native silicon oxides surfaces consists both tetragonal and monoclinic phase. However, the monoclinic phase in  $\text{ZrO}_2$  films deposited on native silicon oxide surfaces cannot be directly linked to their high refractive indexes. If the monoclinic phase was the cause of their higher refractive indexes, we should have observed large difference in refractive indexes between films deposited at 325 °C and 375 °C. The film deposited at 325 °C on native silicon oxide surface predominantly consists of the tetragonal phase, while the film deposited at 375 °C on native silicon oxide surface consist of almost equivalent amount of the tetragonal and the monoclinic phases (Figure 19). Figure 26 shows that the refractive indexes of  $\text{ZrO}_2$  deposited on native silicon oxide surfaces at temperatures higher than 325 °C all fall in the same



(a)



(b)



(c)

Figure 25: SE models for data analysis

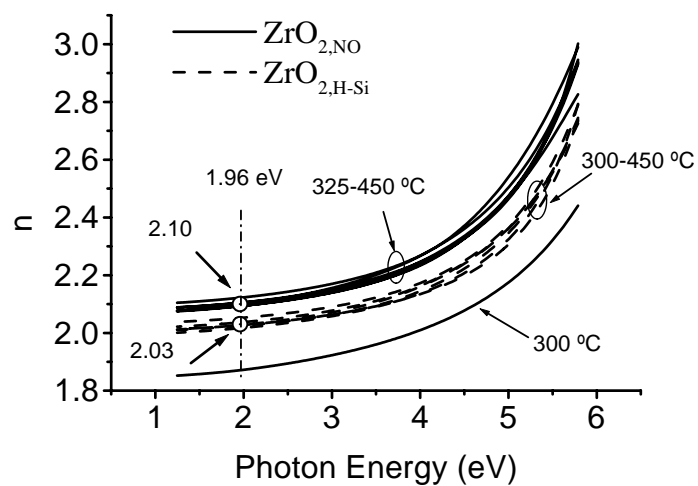


Figure 26: The refractive indexes of  $\text{ZrO}_2$  films deposited on native silicon oxide and H-Si surfaces at different temperatures extracted by the Tauc-Lorentz model

group. Therefore, the structural differences are not the major cause of such refractive index differences.

The most salient feature in Figure 26 is that the refractive index spectra of different samples are roughly parallel to each other. In ellipsometric data analysis, this often suggests that the films are comprised of similar materials, but contain different void fractions<sup>110,119</sup>. The void can exist either in the bulk film as void points or atop the surface as part of the surface roughness layer. Additionally, we must realize that the assumptions for dynamic mode data analysis cannot be strictly satisfied for the initial deposition of ZrO<sub>2</sub>. The surface roughness evolution occurs during deposition, so the contribution from the void fraction in the surface roughness layer is not separated when we extracted these optical constants. As a result, the average refractive index of ZrO<sub>2</sub> films deposited on native silicon oxide surfaces and H-Si surfaces are 2.10 and 2.03, respectively, at 1.96 eV, the energy commonly referenced for refractive index measurements. These values are slight lower than the published refractive index of bulk polycrystalline ZrO<sub>2</sub> (2.2)<sup>58</sup>. This error must be calibrated before the extracted optical constants can be used for further data analysis. However, since the growth rate of the surface roughness layer is not constant, a two-layer model (Figure 25.b), in dynamic mode data analysis, was not successful.

We used a two-step procedure to calibrate this error. First, we used a two-layer model (Figure 25.b), to separate the surface roughness layer and the ZrO<sub>2</sub> layer in static mode data analysis. Unlike the dynamic mode data analysis, where SE models are fitted to all available spectra, in static mode SE models are fitted to each individual SE spectrum. We used the results obtained in Figure 26 as a guide to choose the sample

having the highest refractive index, and its optical constants to best represent the  $\text{ZrO}_2$  layer. A Bruggeman EMA layer<sup>110</sup>, composed of 50%  $\text{ZrO}_2$  and 50% void space, was used to represent the surface roughness layer. Then, a two-layer model, Model B (Figure 27.b) is fitted to each individual SE spectrum collected during deposition, and the thicknesses of both the surface roughness layer and the  $\text{ZrO}_2$  layer were extracted (Figure 27).

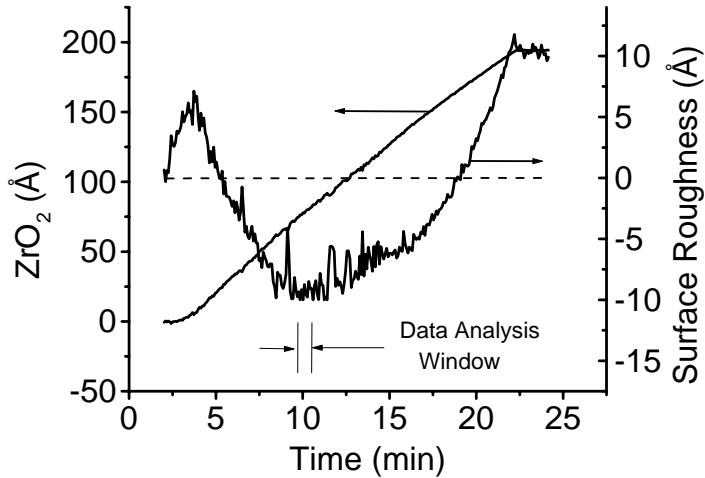


Figure 27: Two-layer model static mode data analysis results

Since the optical constants shown in Figure 26 are combinations of both the  $\text{ZrO}_2$  layer and the surface roughness layer, negative surface roughness layer thickness values are extracted from spectra taken during parts of the deposition process. For further data analysis, we then chose the experimental data within a narrow time window where the  $\text{ZrO}_2$  film has the minimum surface roughness, as shown in Figure 27. In this time window, the deposition rate of the  $\text{ZrO}_2$  layer is constant, so the assumptions for dynamic mode data analysis are satisfied. Therefore, Model A (Figure 25.a) was used to fit

experimental data in this time window using dynamic mode data analysis, and the calibrated optical constants of  $\text{ZrO}_2$  were extracted (Figure 28).

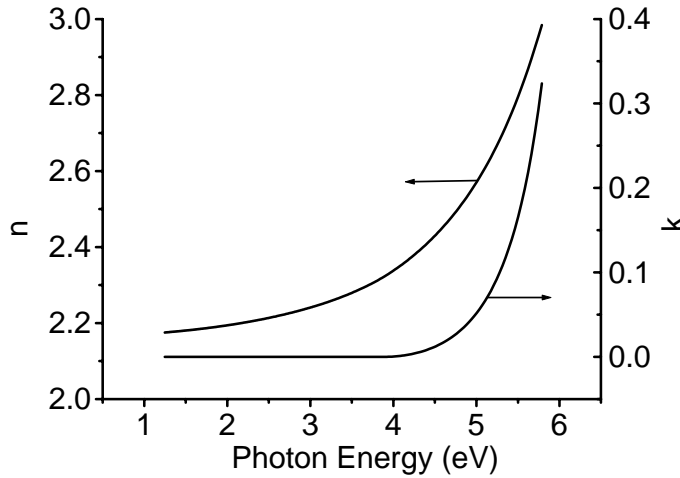


Figure 28: Optical constant of  $\text{ZrO}_2$

#### 4.3.4 SE Modeling of the Initial-stage Deposition of $\text{ZrO}_2$

##### 4.3.4.1 Two-layer SE Model (Model B)

Models using arbitrarily defined nuclei shape and densities are often used to determine the nucleation density and grain size<sup>130,131</sup>. If we assume that the nuclei are hemispherical, a surface roughness layer consisting of 50% film materials and 50% void can be used to simulate the nucleation and the surface roughness evolution during deposition. We used Model B (Figure 25.b) and calibrated optical constants of  $\text{ZrO}_2$  to fit to SE spectra at each individual time to obtain the thickness-time profiles of both the surface roughness layer and the  $\text{ZrO}_2$  layer during deposition on native silicon oxide surfaces (Figure 29) and H-Si surfaces (Figure 30).

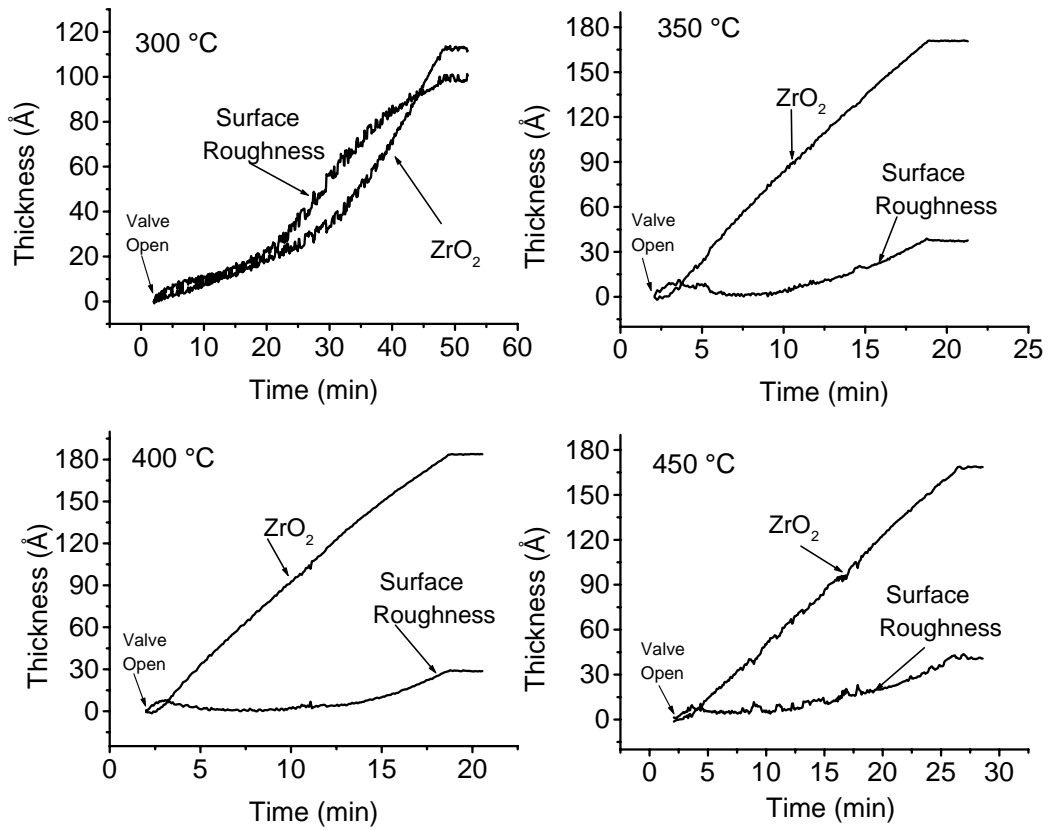


Figure 29: Thickness-time profiles of depositions on native silicon oxide surfaces at different temperatures

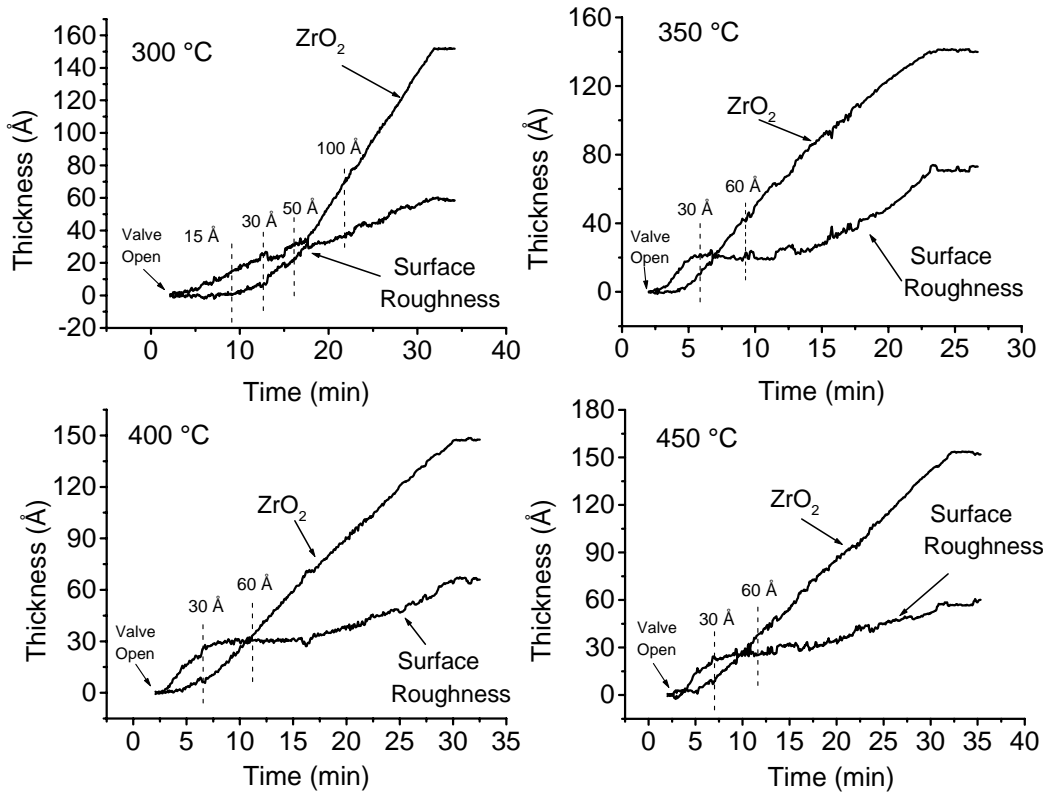


Figure 30: Thickness-time profiles of depositions on H-Si surfaces at different temperatures

$\text{ZrO}_2$  depositions on native silicon oxide surfaces at temperatures higher than 350  $^{\circ}\text{C}$  have similar thickness-time profiles. The growth rates of  $\text{ZrO}_2$  layers change very little over time, and are constant at all these temperatures. All the depositions show a three-stage surface evolution during deposition: (I) initial nucleation, (II) transition, and (III) further nucleation. All deposition processes start with a nucleation process, in which the  $\text{ZrO}_2$  layer does not start growing until a 5-7  $\text{\AA}$  thick surface roughness layer is formed. If we assume the surface roughness layer consists of hemispherical nucleus, the average distance between neighboring nuclei is 10-14  $\text{\AA}$ . As soon as the  $\text{ZrO}_2$  layer starts growing, and the initial nuclei coalesce into a continuous film, the surface roughness

layer starts to decrease. At 350 °C the surface roughness layer decreases faster than at higher temperatures, such as 400 °C. In temperature range 350-400 °C, the surface roughness layer can decrease to zero at certain thicknesses between 30 and 140 Å, while, at temperatures higher than 425 °C, the thickness of surface roughness layer does not drop to zero. Films deposited at temperatures higher than 425 °C have a surface roughness layer throughout the deposition process. Following the surface roughness decrease, the deposition process continues with a further nucleation process, which is characterized by a continuous surface roughness layer thickness increase.

The thickness-time profiles of ZrO<sub>2</sub> depositions on H-Si surface at temperatures higher than 350 °C are also similar. All depositions also show a three-stage surface evolution: (I) initial nucleation, (II) transition, and (III) further nucleation. Unlike the depositions on native silicon oxide surfaces, in the initial deposition processes surface roughness layers reach a thickness of 20-30 Å. During the transition stage, the surface roughness layer thickness keeps constant, instead of decaying to zero, resulting in rougher surfaces compared to ZrO<sub>2</sub> films deposited on native silicon oxide. These results are similar to an earlier report on the deposition on Pt surfaces<sup>90</sup>. In that work, a 95 Å surface roughness was observed before the bulk ZrO<sub>2</sub> layer started growing. The thickness of the surface roughness layer keeps constant until the further nucleation process starts.

Depositions of ZrO<sub>2</sub> at 300 °C on native silicon oxide and H-Si surfaces are different from depositions at higher temperatures. On native silicon oxide surfaces, the surface roughness and ZrO<sub>2</sub> increase simultaneously at a similar growth rate throughout the deposition process, resulting in a high void content low refractive index film. On H-Si

surface, the initial growth of  $\text{ZrO}_2$  layer is inhibited. The deposition process started with a surface roughness increase, suggesting a nucleation process. In the following deposition, the thickness of the  $\text{ZrO}_2$  layer and the surface roughness layer increase simultaneously. Since the growth rate of the  $\text{ZrO}_2$  layer is higher than that of the surface roughness layer after the  $\text{ZrO}_2$  layer reached 30 Å, the  $\text{ZrO}_2$  film deposited on H-Si at 300 °C has a lower void fraction than the film deposited on native silicon oxide.

The two-layer model gives a general description of the deposition process of  $\text{ZrO}_2$  on different surfaces. SE results also show that  $\text{ZrO}_2$  films deposited on native silicon oxide surfaces have lower surface roughness than on H-Si surfaces, consistent with AFM results. However, when we compare details of the results obtained from AFM and in-situ SE, we can find the shortcomings of the two-layer model. AFM results shows that on both native silicon oxide surfaces and H-Si surfaces, the surface roughness increases with nominal film thickness, while on H-Si surfaces, the surface roughness differences between 60 and 30 Å films at 350 °C are larger than at 450 °C. However, SE results show no surface roughness increase between 60 and 30 Å thick  $\text{ZrO}_2$  films. We think this is due to the limitations of SE's capability to characterize these ultra thin films. Although the two-layer model has been successfully used to characterize deposition thick  $\text{ZrO}_2$  (hundreds of nm) films on Pt, using the same two-layer model to characterize ultra thin  $\text{ZrO}_2$  films in this study is problematic. The major difficulty is that the two-layer model cannot separate the void fraction inside the  $\text{ZrO}_2$  layer and the void fraction in these ultra thin films. When we arbitrarily assume a structure consisting of a surface roughness layer and a  $\text{ZrO}_2$  layer, we force the void fraction in the  $\text{ZrO}_2$  layer into the surface roughness layer. This can lead to unphysical results.

The XRD results show a possible explanation to the difference between AFM results and SE results. On H-Si surfaces, the crystallinity of films deposited at lower temperatures, such as 350 °C, is much higher than films deposited at higher temperatures, such as 450 °C. Therefore, the ZrO<sub>2</sub> films deposited at 350 °C have larger long-range order compared to samples deposited at 450 °C. This means that films deposited at 350 °C contain larger grains than films deposited at 450 °C during the initial-stage deposition on H-Si. Therefore, when larger grains stick to each other to form a film, more void fraction is expressed as the surface roughness. On the contrary, when small grains stick to each other more void fractions will become the space between such small grains, while the surface roughness is comparatively unaffected. However, the two-layer model gives a better result for the early nucleation process of ZrO<sub>2</sub> before the film has coalesced, such as depositions at 300 °C on native silicon oxide. Both AFM and SE show consistent results in thickness range lower than 50 Å (Figure 23 and Figure 30).

#### **4.3.4.2 One-layer SE Model (Model C)**

When we used Model B, we arbitrarily added an unnecessary constraint that ZrO<sub>2</sub> and void space each account for 50 % surface roughness layer. This assumption introduces problems in characterizing films having high surface roughness. For high-k gate dielectric applications, the goal is neither to deposit high void fraction films nor to deposit high surface roughness films. It is not necessary to separate the void fraction in ZrO<sub>2</sub> layer from the void fraction in the surface roughness layer. The results from two-layer model shows that the further nucleation process does not start until the film thickness is larger than 80-120 Å. Therefore, we used a one-layer EMA model, consisting

of  $\text{ZrO}_2$  and void (Figure 25.c), to characterize films thinner than 80 Å, the target film thickness range for high-k gate applications. We set film thickness and the void space percentage as fitting parameters, and extracted thickness and void space percentage at each time step throughout the deposition.

Data analysis shows that the MSE values obtained from Model C are lower than those obtained from Model B for depositions on native silicon oxide surfaces at certain conditions: 1) at temperatures 350-400 °C and at thicknesses lower than 140 Å; and 2) at temperatures higher than 425 °C and at the thickness lower than 80 Å. For depositions on H-Si surfaces, Model C has a lower MSE value at thickness less than 80-100 Å. These results indicate that Model C is a more suitable model for analyzing the initial deposition processes. Since the densities of deposited  $\text{ZrO}_2$  films can also affect the optical properties, we changed the  $\text{ZrO}_2$  layer in Model B into an EMA layer consisting of  $\text{ZrO}_2$  and void to account for density differences in  $\text{ZrO}_2$  layer. However, strong correlation problems prevent us from extracting the void fractions in the  $\text{ZrO}_2$  layer and the surface roughness layer simultaneously.

#### 4.3.5 Initial-stage Deposition Profile and Void Fraction Evolution

We used Model C to extract film thicknesses and the corresponding void fraction at each individual time. The void fraction-thickness profiles for depositions on different surfaces are plotted in Figure 31 and Figure 32. The void fraction evolutions of  $\text{ZrO}_2$  films during initial-stage deposition on different surfaces at representative temperatures higher than 350 °C are plotted in Figure 33. We plot the void fraction-thickness profile

for deposition on native silicon oxide surface at 300 °C in Figure 23 along with the previously discussed AFM results.

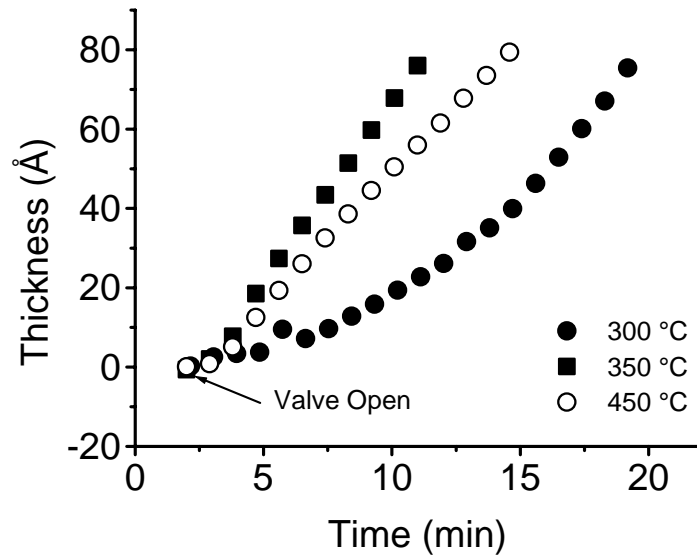


Figure 31: Thickness-time profile of  $\text{ZrO}_2$  initial-stage deposition on H-Si surfaces

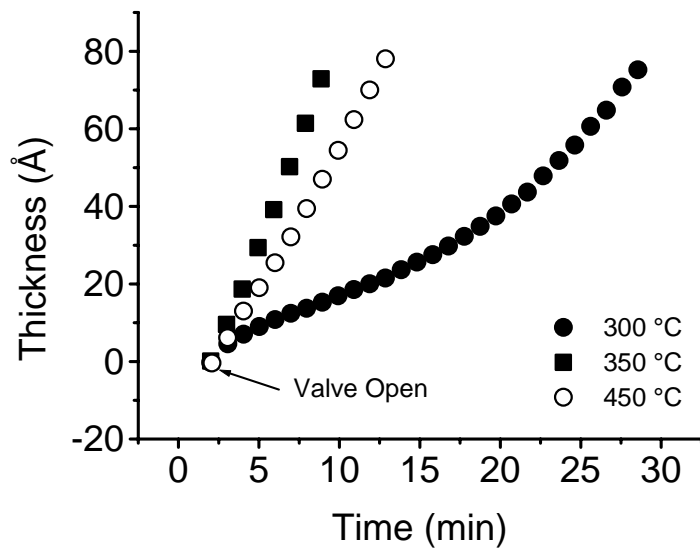


Figure 32: Thickness-time profiles of initial stage  $\text{ZrO}_2$  deposition on native silicon oxide surfaces

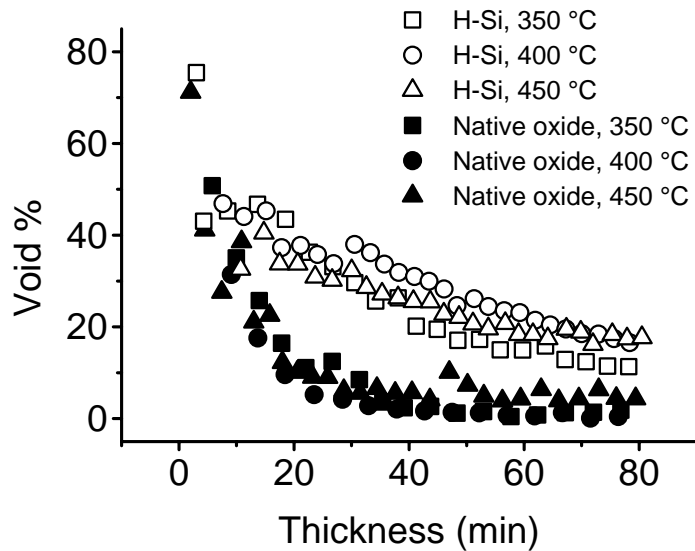


Figure 33: Void fraction evolution during initial-stage deposition

Initial-stage depositions on H-Si surfaces can be divided into two periods: an acceleration period after the onset of deposition, and the following steady state deposition in which deposition rate does not change with time (Figure 31). During the acceleration period the deposition rate increases with time. The length of this transition period is comparatively short when the deposition temperature is higher than 350 °C the film thickness is less than 10 Å during the acceleration period, but these films have void fractions of ~ 40% at the end of the transition period (Figure 33). While the steady state deposition rate does not change with time, the void fraction decreases with time. This is explained by a steady state deposition on the top of a rough surface. The film has limited further surface roughness development. Hence, the void fraction decreases with increasing film thickness. However, when the deposition temperature is low, such as 350 °C, the acceleration period is long, resulting a very non-uniform film (Figure 21).

Depositions on native silicon oxide have two different types of film thickness – time profiles depending on deposition temperature (Figure 32). Depositions on native silicon oxide surfaces at temperatures higher than 350 °C do not have an acceleration period. These depositions directly jump into the steady state deposition, while the void fraction quickly drops to less than 10 % at film thickness ~ 20 Å. Depositions on native silicon oxide surfaces at lower temperatures, such as 300-325 °C, also start at a high deposition rate. However, the deposition rate decreases dramatically after deposition starts. Then, the deposition process exhibits an acceleration period similar to depositions on H-Si surfaces, before it slowly reaches steady state (Figure 32), indicating a nucleation process. The resulting film has both low density and high surface roughness.

Figure 33 shows ZrO<sub>2</sub> films on the two surfaces have different void fraction evolutions during deposition. The void fractions of films deposited on native silicon oxide surfaces are lower than films deposited on H-Si surfaces at all film thicknesses. The void fraction in films deposited on H-Si surfaces decreases continuously as the film deposits, up to a film thickness of 80 Å. The void fraction of films deposited on native silicon oxide surfaces decreases drastically at the onset of deposition. At a thickness of approximately 30-40 Å, the film void fraction reaches zero, suggesting a high-density, low surface roughness film. Therefore, high quality films up to 80 Å can be deposited on native silicon oxide surfaces through proper deposition condition control.

## **4.4 A Discussion on the Initial-stage Deposition of ZrO<sub>2</sub>**

### **4.4.1 Initial-stage Deposition of ZrO<sub>2</sub> on H-Si**

The decomposition mechanism of ZTB can be used to explain the observed differences in initial deposition behavior of ZrO<sub>2</sub> on different surfaces. Details on the deposition mechanism of ZrO<sub>2</sub> from ZTB were discussed in Section 2.2.5.

Native silicon oxide surfaces are terminated by hydroxyl groups, while H-Si surfaces are terminated by hydrogen atoms<sup>109</sup>. At the onset of deposition, ZTB molecules decompose through the  $\beta$ -H-elimination reaction, which produces surface hydroxyl groups<sup>101</sup> and form ZrO<sub>2</sub> clusters on H-Si surfaces. Due to the high reactivity of hydroxyl groups produced on the deposited ZrO<sub>2</sub>, the ZrO<sub>2</sub> clusters become the preferential deposition sites as soon as they are formed. From this moment, the deposition process proceeds in two dimensions: 1) the vertical growth due to the decomposition of ZTB on the top of ZrO<sub>2</sub> clusters, and 2) the lateral growth due to surface diffusion of ZTB molecules initially physically adsorbed on areas terminated by hydrogen atoms, and the decomposition of such ZTB molecules on the edge of ZrO<sub>2</sub> clusters. Since the ZrO<sub>2</sub> coverage during the very early stage deposition is much lower than hydrogen terminated areas, the lateral growth is more significant than vertical growth. This is evident in Figure 31, which shows all depositions on H-Si have an acceleration period after the ZTB supply was turned on. No film thickness increase was observed during the induction period. As the process proceeds, the surface coverage of hydrogen atoms decreases. Since the lateral growth depends on the surface coverage of hydrogen atoms, the vertical growth rate soon becomes higher than lateral growth of the ZrO<sub>2</sub> clusters (or islands at this stage).

At this stage the surface has changed into a hydroxyl group terminated surface. Both hydroxyl groups and ZTB have polarized bonds. Because of stronger interaction between hydroxyl groups and ZTB molecules, ZTB molecules are less mobile on hydroxyl group terminated surfaces. On the other hand, due to the topology developed during the induction period, the fluxes to different points on the surface will differ. The peaks of  $\text{ZrO}_2$  clusters/islands will have a higher ZTB flux impinging on them, enhancing the deposition rates compared to a flat surface. This magnifies the existing topology, leading to a 3-dimentional (3-D) nucleation process (Figure 34). An extreme example is the deposition at 300 °C. Due to the low surface mobility of ZTB molecules and low surface density of hydroxyl groups, the surface roughness layer keeps increasing during the whole deposition process, resulting in a highly non-uniform film. At higher temperatures the decomposition rate of ZTB is so fast that the influence of surface diffusion becomes less important. Whenever ZTB molecules reach the surface they decompose immediately at the same location. Small clusters form on the top of clusters, so the films deposited at higher temperatures have lower long-range order. Additionally, the topology of the film is mainly influenced by the uniformity of the flux, so surface roughness increase at lower temperatures is much higher than at higher deposition temperatures. In summary, at the target film thickness range for high-k gate application, ~50% of the film thickness is the surface roughness layer. Due to the high surface roughness, the resulting  $\text{ZrO}_2$  film deposited on H-Si surface is not suitable for depositing high-k gate dielectric films.

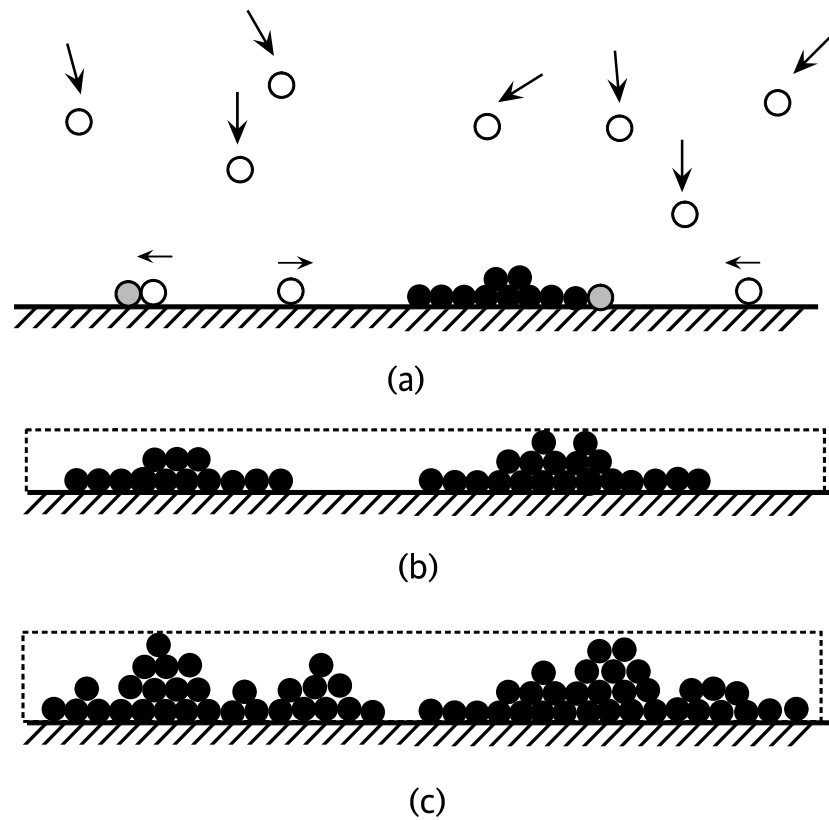


Figure 34: A schematic of the film formation mechanism of  $\text{ZrO}_2$  on H-Si surfaces, where O represents ZTB molecules, ● represents the reaction intermediates, and ● represents  $\text{ZrO}_2$ . (a) At the onset of deposition, the deposition process is limited by the number of available reactive sites. Adsorbed ZTB molecules diffuse on H-Si surface to form  $\text{ZrO}_2$  clusters. (b) Due to high coverage of H-Si surface, the lateral growth of  $\text{ZrO}_2$  is faster than vertical growth. At the same time, topology is developed as soon as clusters form. (c) When H-Si coverage is low, the lateral growth of  $\text{ZrO}_2$  stops. At this stage the H-Si has been replaced by  $\text{ZrOH}$ , on which ZTB cannot diffuse quickly. Due to the topology development in (b), the sites receive different ZTB fluxes. Therefore, the topology development is magnified during further deposition process.

#### **4.4.2 Initial-stage Deposition of ZrO<sub>2</sub> on Native Silicon Oxide Surfaces**

Native silicon oxide surfaces are covered with hydroxyl groups. Due to the high reactivity of hydroxyl groups and their high surface density on native silicon oxide surfaces, surface hydroxyl groups quickly react with ZTB molecules and form a low void fraction ZrO<sub>2</sub> monolayer. The void fraction of these films quickly dropped to a minimum value shortly after initiating deposition. This is proven by the high starting deposition rate on native silicon oxide surfaces at 300 °C. As shown in Equations 2.7 to 2.9, concurrent with the reaction between surface hydroxyl groups and ZTB molecules, the surface is changed into a t-butoxy group terminated surface.

The thermal stability of the t-butoxy groups, as well as the surface density of hydroxyl groups influences the continued deposition. At lower deposition temperatures, such as 300-325 °C, the t-butoxy groups have higher stability. Since the t-butoxy groups do not directly react with ZTB like hydroxyl groups do, the properties of the surface are similar to H-Si surfaces. As a result, the deposition rate quickly degrades as the surface hydroxyl groups are depleted (Figure 32). Thereafter, the deposition rate increases slowly while the density of surface hydroxyl group builds up through the decomposition of butoxy groups or incoming ZTB. The surface of deposited is rough (Figure 22 and Figure 23). This deposition process is described by Figure 35.a.

At temperatures higher than 350 °C, the stability of the intermediate t-butoxy groups no longer affects the deposition process, so the surface hydroxyl groups can be effectively regenerated. Since the first layer is formed uniformly, the distribution of hydroxyl groups on the surface is even. The 3-D type nucleation does not happen on native silicon oxide surfaces (Figure 35.b). As soon as the native silicon oxide surface is

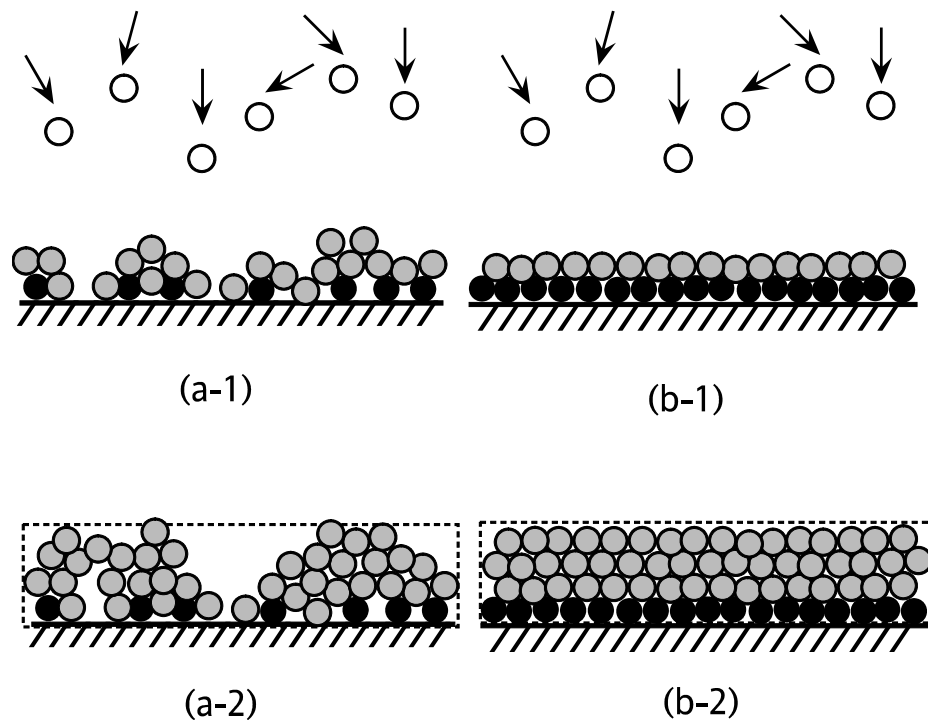


Figure 35: A schematic of the film formation mechanism of  $\text{ZrO}_2$  on native silicon oxide surfaces, which have few (a) and many (b) reactive sites, where  $\circ$  represents ZTB molecules,  $\bullet$  represents decomposed ZTB and  $\text{ZrO}_2$ , and  $\bullet\bullet$  represents high energy hydroxyl groups on native silicon oxide surfaces. (a-1) At low substrate temperatures,  $\text{ZrO}_2$  reacts with high energy hydroxyl groups, and form clusters on native surface oxide surface. (a-2) ZTB molecules diffuse slowly on hydroxyl group terminated surfaces. Due to different ZTB fluxes on different sites, the topology is magnified in further deposition process, resulting high void fraction in films. (b-1) At higher substrate temperatures, such as  $400\text{ }^\circ\text{C}$ , native silicon oxide surface is covered by reactive hydroxyl groups. A monolayer of  $\text{ZrO}_2$  is quickly formed at the onset of deposition. (b-2) Since all the sites have a similar view angle, topology development is suppressed.

completely changed into ZrO<sub>2</sub> surface, the following deposition on H-Si surface is the same as the deposition on native silicon oxide surface. The effects of ZTB surface diffusivity and ZTB decomposition rate will also affect the surface roughness increase during film thickness increases and the crystallinity of films.

In summary, the initial-stage deposition of ZrO<sub>2</sub> on different surfaces will directly influence the properties of deposited films. The initial-stage deposition of ZrO<sub>2</sub> on H-Si surface induces large topology development, resulting non-uniform films, so H-Si is not suitable for high-k gate dielectric applications. The reactive hydroxyl groups on native silicon oxide surface prevent the initial 3-D type nucleation of ZrO<sub>2</sub>. The films deposited on native silicon oxide surfaces are uniform at thicknesses less than 80 Å. Native silicon oxide surface is suitable for high-k gate dielectric film deposition.

#### **4.5 Conclusions**

We used in-situ SE method to study the deposition process of ZrO<sub>2</sub> from ZTB on both native silicon oxide and H-Si surfaces. We compared the results obtained from different SE models to the results from AFM, and discussed the difficulties in SE characterization on ultra thin ZrO<sub>2</sub> films during initial-stage deposition. We discovered that ZrO<sub>2</sub> films deposited of native silicon oxide surfaces have higher refractive indexes and film densities. We showed that different nucleation and coalescence processes during the initial-stage deposition on different surfaces affect the properties of the deposited films. On H-Si surfaces, the lack of reactive surface hydroxyl groups and high surface diffusivity of ZTB molecules lead to 3-D nucleation process. The resulting films have high surface roughness, and are inappropriate for gate dielectric applications. On native

silicon oxide surface, the highly reactive hydroxyl groups react with ZTB molecules to form a high-density layer on the top of native silicon oxide surface. At temperatures higher than the decomposition temperature of the t-butoxy group, further 3-D nucleation of  $\text{ZrO}_2$  is suppressed. The resulting films have low void fraction and low topology development, and are more suitable for gate dielectric applications.

## CHAPTER V

### INITIAL-STAGE DEPOSITION OF ZRO<sub>2</sub> ON H-TERMINATED SI(100) AND NATIVE SILICON OXIDE SURFACES

#### 5.1 Background

The aggressive dimensional scaling of MOSFET has pushed the traditional gate dielectric material, silicon dioxide, to its physical property limits. Silicon dioxide films thinner than approximately 1 nm cannot sustain the potential drop necessary to drive the devices, resulting in large direct tunneling currents. These tunneling currents negatively impact proper operation of the MOSFETs<sup>5,30</sup>. High-k dielectric materials are expected to replace silicon dioxide as the gate dielectric layers to solve this problem<sup>5,30</sup>.

There are several significant differences between the current gate stack structure and the one fabricated with a high-k dielectric material. High-k materials require a different formation process from the traditional thermal silicon oxidation. The silicon oxidation process involves the diffusion of an oxidant, often O<sub>2</sub>, into the silicon substrate followed by the reaction between silicon and the oxidant<sup>65</sup>. The uniformity of silicon dioxide films has not been a significant issue for many years. The deposition process for high-k materials presents a significant challenge. We have discussed these challenges in high-k dielectric deposition processes in Section 2.2.2. The successful deposition process must produce films of uniform composition, microstructure, thickness and interface properties.

ZrO<sub>2</sub> films deposited by ALCVD on H-Si surfaces consist of two layers: the ZrO<sub>2</sub> layer and an interfacial layer<sup>59,85</sup>. Neither the ZrO<sub>2</sub> layer thickness nor the interfacial layer thickness was reported to be uniform. The ZrO<sub>2</sub> layer consisted of separated ZrO<sub>2</sub>

islands, while the interfacial layer was composed of zirconium silicate. On the contrary,  $\text{ZrO}_2$  deposited on oxidized silicon surfaces are uniform, and have favorable properties for high-k gate applications. These results show that the starting surface can significantly affect the properties of deposited films. A detailed report of the influences of deposition conditions on film properties is not currently available.

In Chapter IV, we presented in-situ SE results about the differences between the  $\text{ZrO}_2$  initial-stage deposition process on H-Si surfaces and native silicon oxide surfaces<sup>132</sup>. We discussed the influence of deposition conditions on film properties and proposed a general description of the deposition process of  $\text{ZrO}_2$  on different surfaces. In this chapter, we extend our previous work and investigate details of deposited films using complementary analytical tools, such as angle resolved X-ray photoelectron spectroscopy (ARXPS), time of flight medium energy back scattering (TOF MEBS), and TEM techniques.

## 5.2 Experimental Details

$\text{ZrO}_2$  films were deposited from ZTB in an UHV compatible CVD system at substrate temperatures of 350, 400, and 450 °C, and at a total pressure of  $10^{-6}$ - $10^{-5}$  Torr. Native silicon oxide and H-Si were used as starting surfaces for this work. The deposition precursor, ZTB, flowed from a bubbler through a heated gas manifold system and entered the reactor through the bottom of the deposition chamber. No carrier diluent gases were used. Spectroscopic ellipsometric (SE) spectra were collected with the software EASE® (J.A. Woollam Company, Lincoln, NE) at two second intervals during deposition. SE spectra within the photon energy range of 1.25 – 5.8 eV were used for data processing.

We stopped deposition when the thickness of deposited films measured by in-situ SE reached 30 or 60 Å. Details of the CVD system, the preparation of substrate surfaces, and deposition process can be found in Section 3.2. A brief description is provided here for completeness.

We used a two-layer ellipsometric model to monitor the growth of ZrO<sub>2</sub> during the deposition process. The two-layer model consisted of a TL layer<sup>115</sup> to represent the ZrO<sub>2</sub> layer, and a virtual substrate layer. Ellipsometric data collected from the starting surfaces before precursor introduction were used to represent the virtual substrate. After deposition, the data were reevaluated using an EMA layer to extract the void fraction evolution during the deposition process<sup>133</sup>. Details of this method were discussed in Chapter IV and previously reported in references<sup>132</sup>.

Topographic images of the deposited films were obtained using a Digital Instruments' Nanoscope IIIa atomic force microscope (AFM) with etched silicon probes (NanoSensor NCH). The typical tip radius of curvature is 2 nm. Images of 2×2 μm areas with 512-line resolution were used to determine the surface-roughness of these samples. A plane fit and a first-order flattening were performed prior to calculating surface-roughness.

TEM was used to evaluate the morphology and microstructure of the films. TEM samples were prepared by mechanical polishing down to 5 μm thickness, followed by argon ion thinning in the area of interest to the point of electron transparency. A 200 kv acceleration voltage field-emission transmission electron microscope with a twin-lens configuration was used for analysis. The instrument was operated at 200 kV. High-resolution cross-sectional TEM images were obtained with sample interfaces parallel to

the direction of the beam. Plan-view TEM images were obtained with the Si(100) plane perpendicular to the direction of the beam.

Time-of-flight medium energy backscattering (TOF MEBS) was used to analyze the composition of both the ZrO<sub>2</sub> and interfacial layer. The ion scattering measurements were carried out in vacuum at  $\sim 10^{-6}$  Torr. 270 keV incident He<sup>+</sup> beam was used for all experiments. Details of data collection are available in reference<sup>134</sup>. ToF MEBS spectra were simulated using the Mathematica based RBSTools package<sup>135</sup>. A three layer thin-film model was used to simulate the backscattering spectra. The model consisted of a ZrO<sub>2</sub> layer on a Si substrate with an interfacial layer containing Zr, Si, and O. Stoichiometry and thickness values were obtained from a best fit of the simulation to experimental spectra.

A ThetaProbe® ARXPS system was used to study the depth profile of samples deposited on different surfaces at 350 °C. Photoelectrons initiated by X-rays emerge from the sample surface over a range of angles. The ThetaProbe ARXPS systems measures the intensity of the photoelectron emission, as a function of emission angle, which provides information about the distribution of elements as a function of depth below the surface. A micro channel detector (MCD) incorporated in the ThetaProbe system allows spectra to be acquired with up to 112 energy channels and up to 96 angular channels. Samples were mounted on a standard ThetaProbe sample holder, and analyzed using a standard micro-focused, monochromatic Al K<sub>α</sub> X-rays, with a 400 μm X-ray spot size, a 100 eV pass energy and a 0.1 eV step size to scan Si<sub>2p</sub>, O<sub>1s</sub> and Zr<sub>3d</sub> peaks. For each elemental region, sixteen angle resolved spectra were recorded.

Ex-situ ellipsometry data were collected from as-deposited samples using a J.A. Woollam M-2000DI multi-angle spectroscopic ellipsometer at a  $75^\circ$  incident angle. Scans were collected for 60 s to minimize random noise in the collected data.  $\Psi$  and  $\Delta$  values within the full photon energy range of our ellipsometer (1.2 to 6.5 eV) were used for data fitting. Data processing was conducted using WVASE 32, a software application developed by J.A. Woollam Company.

## 5.3 Results

### 5.3.1 In-situ SE

In-situ real time SE data were collected during deposition. After deposition, we used a two-layer ellipsometric model to evaluate the void fraction evolution during deposition. The two-layer ellipsometric model consists an EMA layer and a virtual substrate layer. The EMA layer has two components void and  $\text{ZrO}_2$  whose optical constant were obtained from experiments<sup>132</sup>. The optical constants of  $\text{ZrO}_2$  were the same as those extracted from the TL model<sup>115</sup> in reference<sup>132</sup>. Ellipsometric data collected from the starting surfaces before precursor introduction were used to represent the virtual substrate. Therefore, the void fraction evolution during deposition was extracted from in-situ ellipsometric data.

Figure 36 and Figure 37 show the void fraction evolution of  $\text{ZrO}_2$  films deposited on different surfaces during initial-stage deposition. On H-Si surfaces, the void fraction of  $\text{ZrO}_2$  films decreases continuously with increasing film thickness, but does not reach zero. At a fixed thickness, film void fraction decreases with increasing substrate temperature. On native silicon oxide surfaces, the void fraction of  $\text{ZrO}_2$  films dropped to

approximately zero in the 30-40 Å thickness range. The void fraction remains low during further deposition. Additionally, substrate temperature has only a weak influence on void fraction.

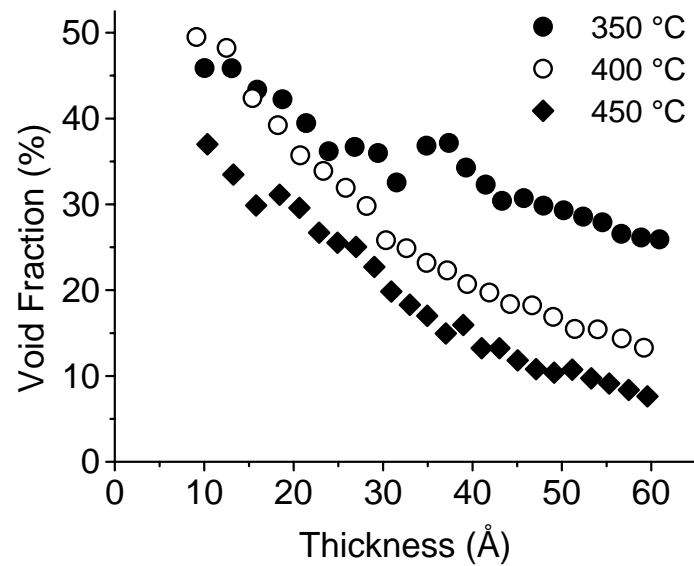


Figure 36: Void fraction evolution during  $\text{ZrO}_2$  initial-stage deposition on H-Si surfaces.

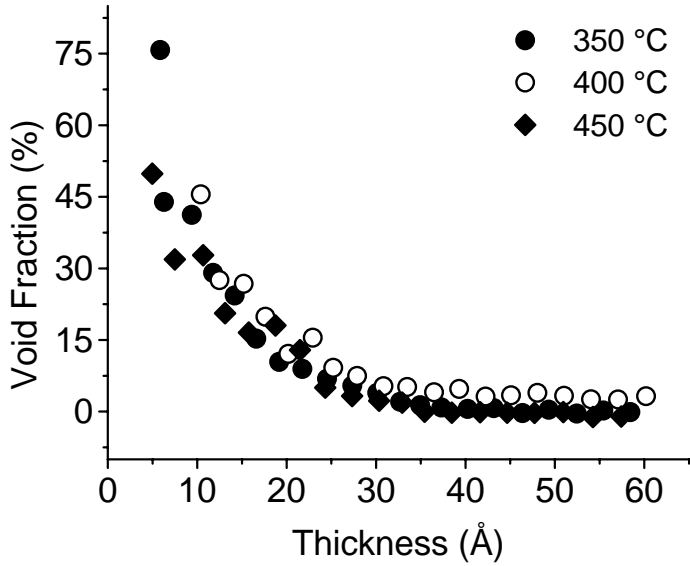


Figure 37: Void fraction evolution during  $\text{ZrO}_2$  initial-stage deposition on native silicon oxide surfaces

### 5.3.2 AFM

Figure 38 contains representative AFM images of films deposited on the different surfaces. The surface roughness results are plotted in Figure 39 and listed in Table 4. Figure 38 shows that starting surface, deposition temperature, and film thickness all have an influence on the surface roughness of the deposited films. On both H-Si and native silicon oxide surfaces, surface roughness increases with film thickness. When the film thickness increased from 30 to 60 Å, the surface roughness of films deposited on native silicon oxide surfaces increased by less than 1 Å, but on H-Si surfaces, the surface roughness increased by more than 2.5 Å. The surface roughness of films deposited on H-Si surfaces decreases with increasing deposition temperature. On native silicon oxide surfaces, films deposited at 400 °C have higher surfaces roughness than for depositions at both 350 and 450 °C. The magnitude of the effect of thickness on surface roughness is dependent on deposition temperature. When the thickness is increased from 30 to 60 Å,

on both H-Si surfaces and native silicon oxide surfaces,  $\text{ZrO}_2$  films exhibit a maximum in surface roughness increase at 350 °C, and a minimum in surface roughness increases at 450 °C.

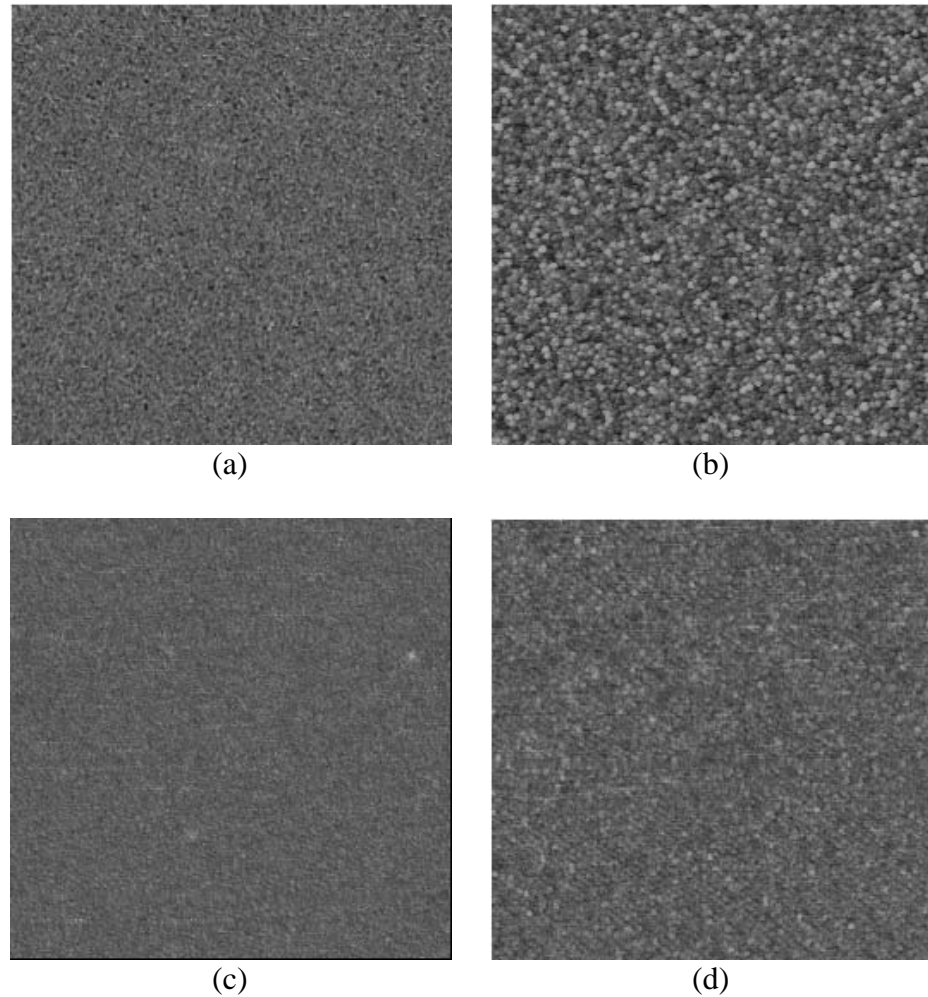


Figure 38:  $2\mu\text{m} \times 2\mu\text{m}$  AFM images of (a) 30 Å and (b) 60 Å  $\text{ZrO}_2$  films deposited on H-Si surfaces at 350 °C, and (c) 30 Å and (d) 60 Å  $\text{ZrO}_2$  films deposited on native silicon oxide surfaces at 350 °C

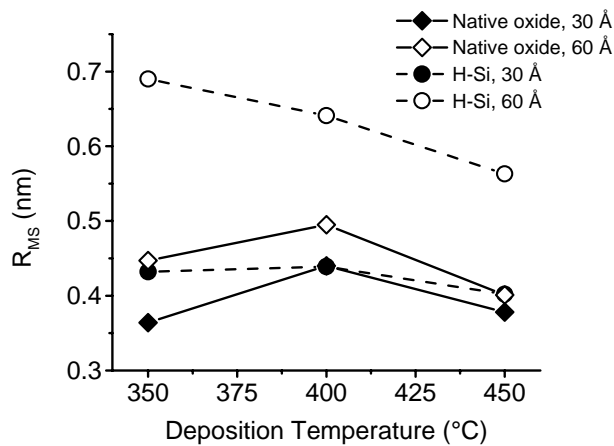


Figure 39: The surface roughness of 30 and 60 Å ZrO<sub>2</sub> films deposited on H-Si and native silicon oxide surfaces

Table 4 Thicknesses of some samples measured by different methods

Starting surface	Deposition Temperature (Å)	Layers	Physical Measurement*	Ex-situ SE (Å)	ToF MEBS (Å)	ARXPS (Å)
H-Si	350	Surface roughness	4.32	24.12	-	-
		ZrO <sub>2</sub>	0 – 36.6	0.88	13.82	9
		Interfacial layer	21.9	21.89	14.67	25
H-Si	450	Surface roughness	4.02	30.12	-	-
		ZrO <sub>2</sub>	15.8 – 26.8	0	18.05	-
		Interfacial layer	14.6	18.4	17.93	-
Native silicon oxide	350	Surface roughness	3.04	18.12	-	-
		ZrO <sub>2</sub>	30.4	13.97	22.68	29
		Interfacial layer	14.6	18.98	16.57	13
Native silicon oxide	450	Surface roughness	3.78	19.34	-	-
		ZrO <sub>2</sub>	31.7	13.33	24.33	-
		Interfacial layer	15.9	19.37	16.95	-

\* Surface roughness is measured by AFM, while ZrO<sub>2</sub> layer thickness and interfacial layer thickness are measured by cross sectional TEM.

### 5.3.3 TEM

Figure 40 shows the cross sectional TEM images of 30 Å ZrO<sub>2</sub> films deposited on H-Si and native silicon oxide surfaces at 350 and 450 °C. Lattice fringe edges and contrast differences were used to define the top and bottom surfaces of the interfacial layers. The distance between these two surfaces was defined as the thickness of the interfacial layer. The distance between the top of the interfacial layer and the bottom of the valleys on the ZrO<sub>2</sub> top surface was defined as the thickness of the ZrO<sub>2</sub> layer. The measured thickness values are listed in Table 4.

The TEM images show that ZrO<sub>2</sub> films deposited on different surfaces have different structures. ZrO<sub>2</sub> films deposited on H-Si surfaces are not uniform, and consist of separated islands. The spacing between islands for films deposited at 350 °C is larger than for films deposited at 450 °C. This is also confirmed by plan view TEM results [Figure 41(a) and (b)]. This observation indicates that the coalescence of ZrO<sub>2</sub> films begins at a lower films thickness at 450 °C than at 350 °C. Figure 42(a) and (b) show further progression of the coalescence process. At 60 Å film thickness the boundary between islands can still be identified, though the spacing between islands has been reduced compared to that seen in Figure 41(a) and (b). Films deposited on native silicon oxide surfaces appear uniform. No separated islands can be identified on either the cross sectional TEM images [Figure 40(c) and (d)] or plan view TEM images [Figure 41(c) and (d)]. Figure 42(c) and (d) show that 60 Å ZrO<sub>2</sub> films deposited on native silicon oxide surfaces have coalesced. Additionally, all cross sectional TEM images contain an interfacial layer between ZrO<sub>2</sub> and the silicon substrate. The interfacial layer thicknesses of ZrO<sub>2</sub> films deposited on native silicon oxide surfaces are not affected by deposition

temperature, while the interfacial layer thickness of  $\text{ZrO}_2$  deposited on H-Si at 350 °C is thicker than at 450 °C.

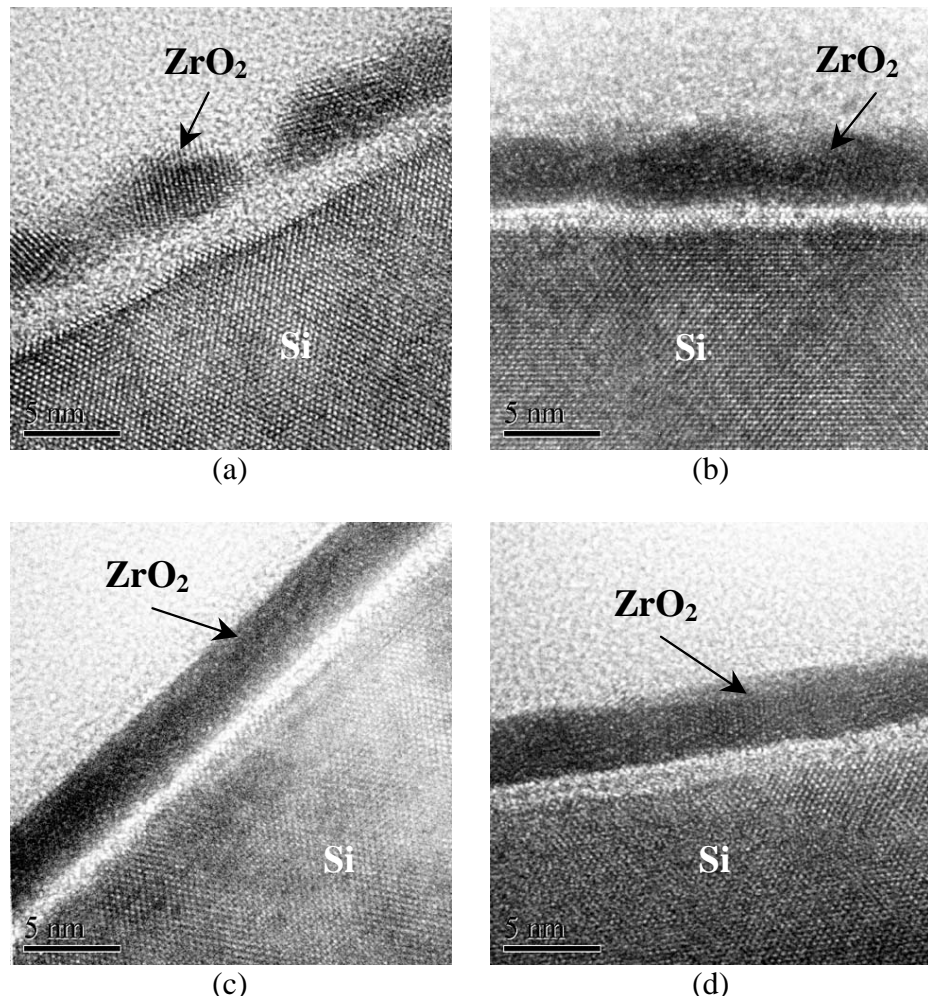


Figure 40: Cross sectional TEM images of 30 Å  $\text{ZrO}_2$  films deposited on H-Si surfaces at (a) 350 °C and (b) 450 °C, and 30 Å films deposited on native silicon oxide surfaces at (c) 350 °C and (d) 450 °C

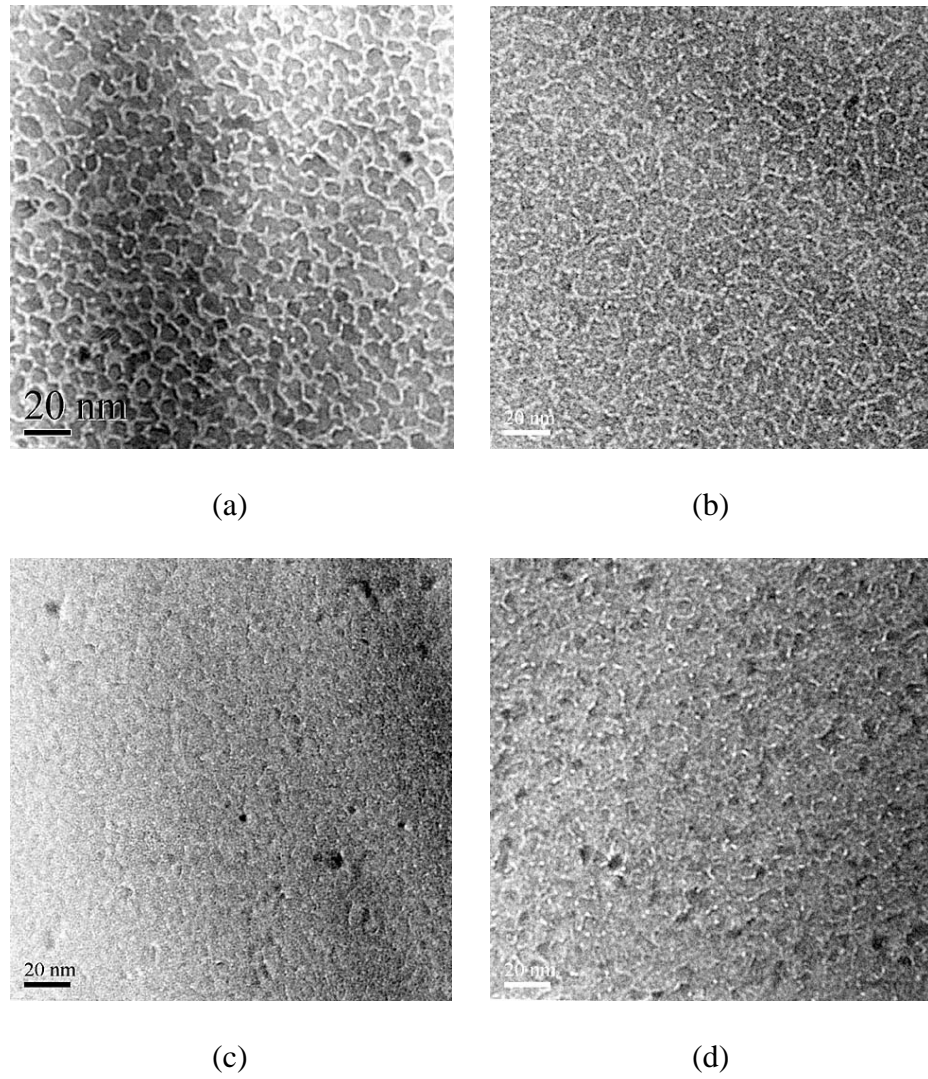


Figure 41: Plan view TEM images of 30 Å ZrO<sub>2</sub> films deposited on H-Si surfaces at (a) 350 °C and (b) 450 °C, and deposited on native silicon oxide surfaces at (c) 350 °C and (d) 450 °C

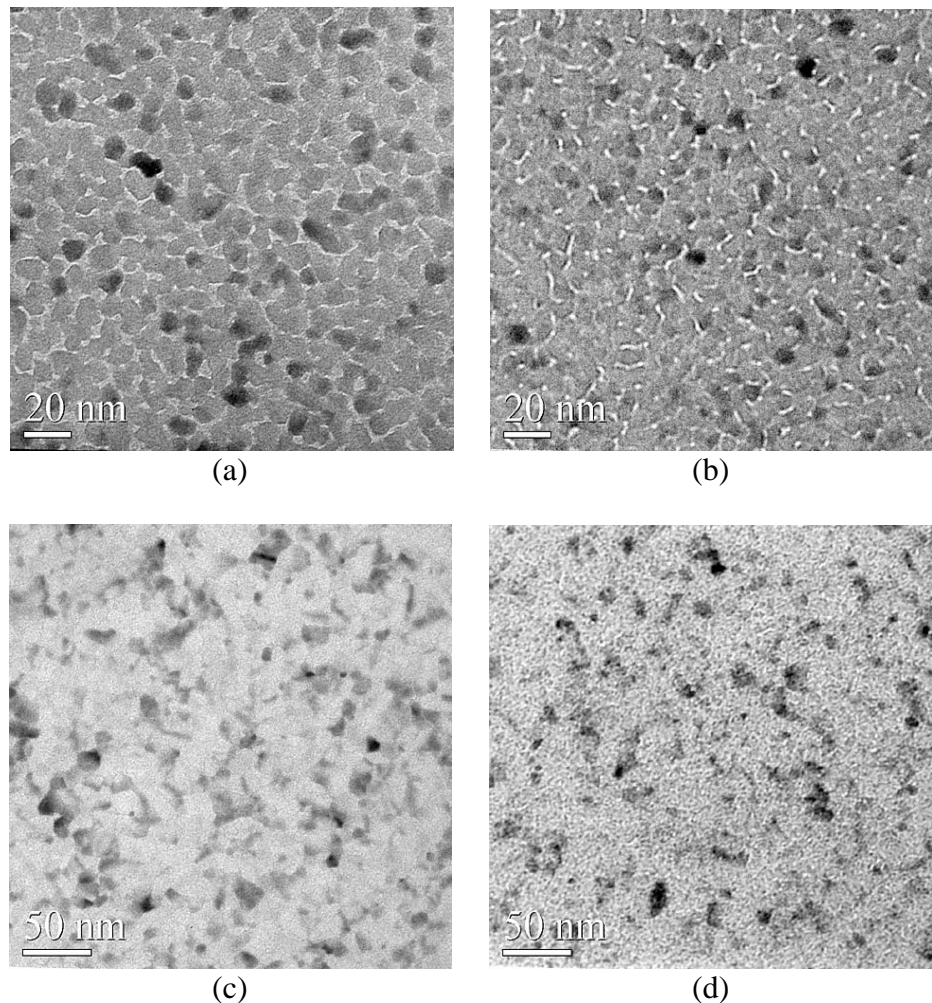


Figure 42: Plan view TEM images of 60 Å ZrO<sub>2</sub> films deposited on H-Si surfaces at (a) 350 °C and (b) 450 °C, and deposited on native silicon oxide surfaces at (c) 350 °C and (d) 450 °C

### 5.3.4 ToF MEBS

Figure 43 presents representative backscattering spectra of  $\text{ZrO}_2$  deposited on H-Si and native silicon oxide surfaces. Both films have a nominal thickness of 30 Å, as determined by in-situ SE. Identical integrated charge was collected for each experiment; however, the zirconium and oxygen peaks in the spectrum from the film deposited on native silicon oxide are larger. This result is consistent for all samples in this work. These results demonstrate that a denser  $\text{ZrO}_2$  film is deposited on native silicon oxide surfaces than on H-Si surfaces. Similar results were obtained in a study by Copel et al using 200 keV MEIS where  $\text{ZrO}_2$  was deposited on thermally grown  $\text{SiO}_2$ <sup>59</sup>.

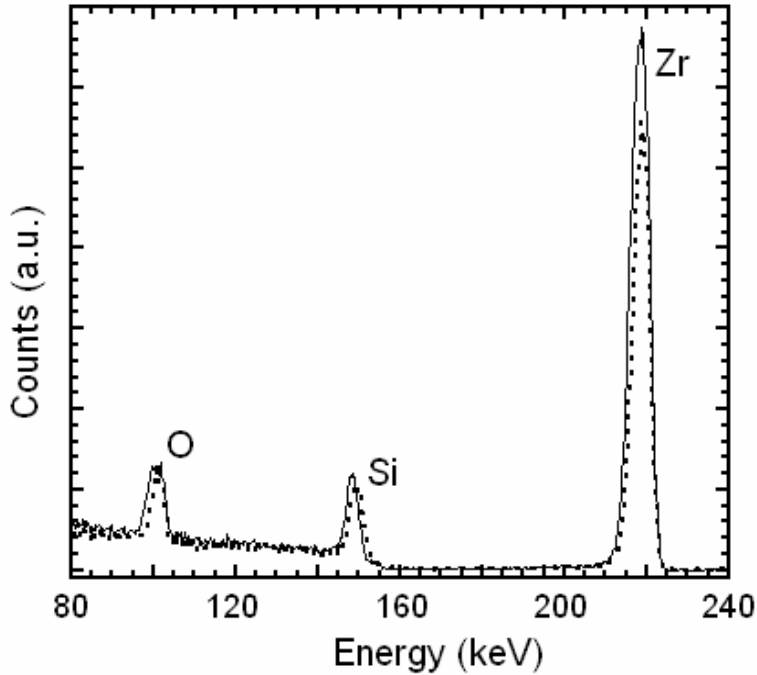


Figure 43: 270 keV  $\text{He}^+$  TOF-MEBS backscattering spectra of 30 Å  $\text{ZrO}_2$  deposited at 450 °C on native silicon oxide (—) and H-Si (----).

Figure 44 shows a representative TOF-MEBS  $\text{He}^+$  backscattering spectrum and simulation for 30 Å  $\text{ZrO}_2$  deposited on H-Si at 450° C. Simulations indicated that the

$\text{ZrO}_2$  films were slightly oxygen deficient, and an interfacial layer of  $\text{ZrSi}_x\text{O}_y$  was present. The atomic ratio of Zr to oxygen in all of the  $\text{ZrO}_x$  layers is in the range of 1-1.2:2, which is not affected by the deposition temperature, film thickness, nor starting surface. However, the composition of the interfacial layer does depend on the starting surface (Figure 45). The interfacial layer of films deposited on H-Si surfaces contains twice as many zirconium atoms as than those deposited on native silicon oxide surfaces.

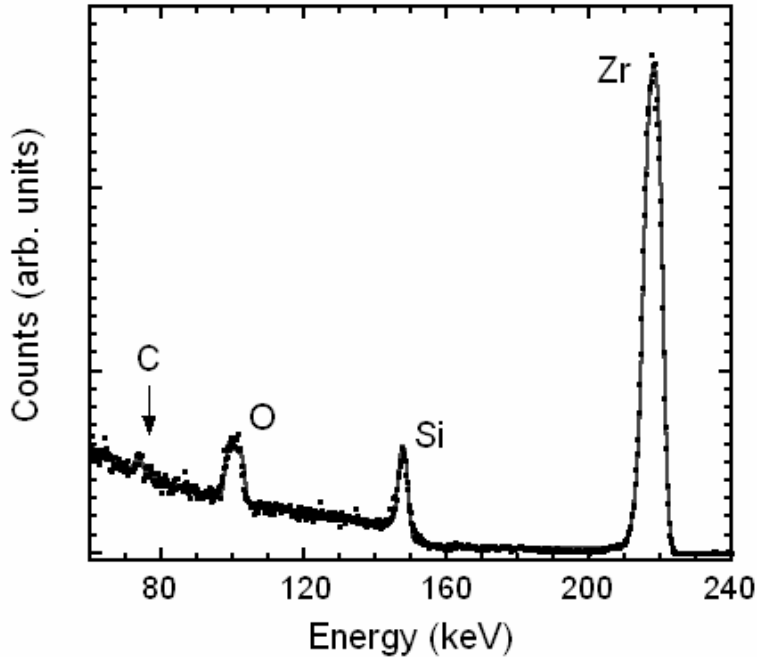


Figure 44: 270 keV  $\text{He}^+$  TOF-MEBS  $\text{He}^+$  backscattering spectrum (....) and simulation (—) of 30 Å  $\text{ZrO}_2$  deposited on native silicon oxide at 450° C. The solid line shows the simulation.

Precise TOF MEBS determination of the thicknesses of each layer is difficult since accurate density values for the layers are not available. Additionally, results are limited by the depth resolution of the TOF MEBS system<sup>136</sup>. We used the bulk  $\text{ZrO}_2$  density of 5.7 g/cm<sup>3</sup> and an empirical interfacial layer density of 3.7 g/cm<sup>3</sup> in simulations.

TOF MEBS is not sensitive to the surface roughness. Therefore, only the thickness values of ZrO<sub>2</sub> layers and interfacial layers are plotted in Figure 45 and listed in Table 4.

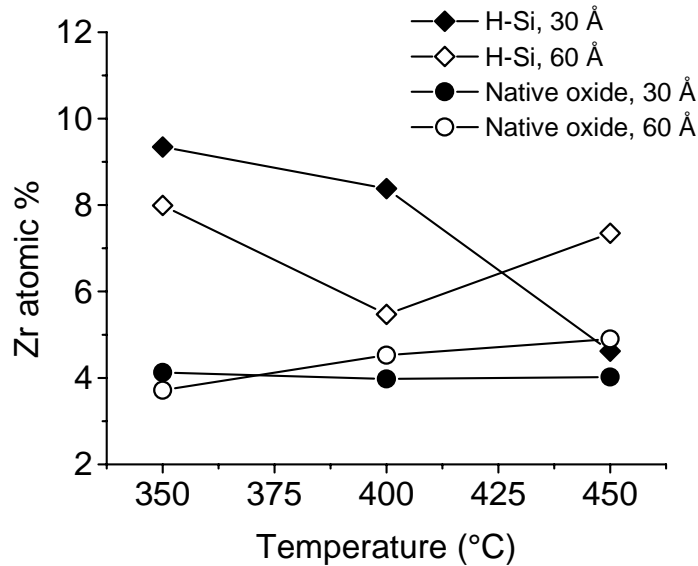
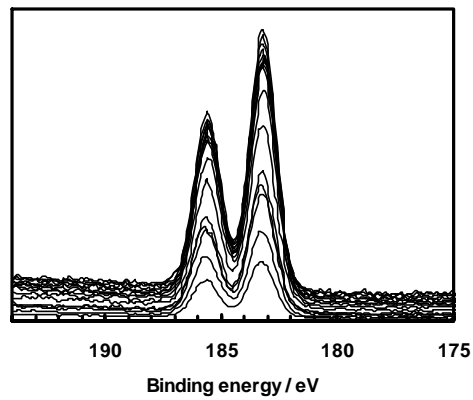


Figure 45: Interfacial layer zirconium atomic ratio of 30 and 60 Å ZrO<sub>2</sub> films deposited on H-Si and native silicon oxide surfaces at different temperatures.

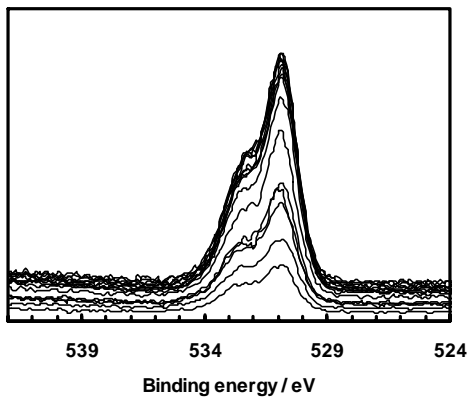
### 5.3.5 ARXPS

Zr 3d, O 1s, and Si 2p ARXPS spectra were acquired from two 30 Å ZrO<sub>2</sub> samples deposited at 350 °C on H-Si (Figure 46) and on native silicon oxide surfaces (Figure 47). Spectra from 16 take-off angles were recorded simultaneously for each elemental region. These ARXPS spectra were used to calculate the concentration depth profiles of the elements and the thickness of the zirconium oxide films using the method of maximum entropy<sup>137</sup>. For concentration depth profile calculations, we assumed that the film and the substrate have 0% and 100 % elemental silicon respectively. For sample thickness calculations, the film deposited on H-Si surfaces was assumed to consist of ZrO<sub>2</sub> and Zr<sub>2</sub>SiO<sub>4</sub> layers on Si. The stoichiometry of the interfacial silicate layer was

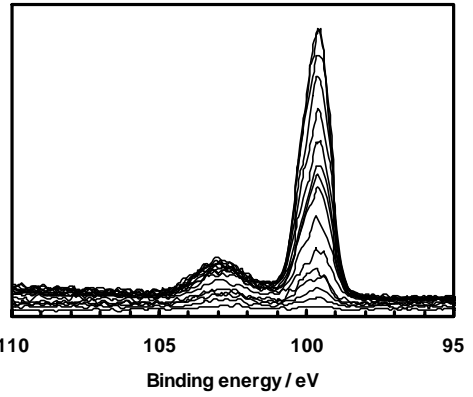
taken from the concentration depth profile. Density values of 5.68 g/cm<sup>3</sup> and 3.1 g/cm<sup>3</sup> were used for the ZrO<sub>2</sub> layer and the interfacial Zr<sub>2</sub>SiO<sub>4</sub> layer respectively<sup>138</sup>. The film deposited on native silicon oxide surface was assumed to consist of ZrO<sub>2</sub> and SiO<sub>2</sub> layers. Density values of 5.68 g/cm<sup>3</sup> and 2.196 g/cm<sup>3</sup> were used in calculations, for ZrO<sub>2</sub> and SiO<sub>2</sub>, respectively<sup>138</sup>.



(a)

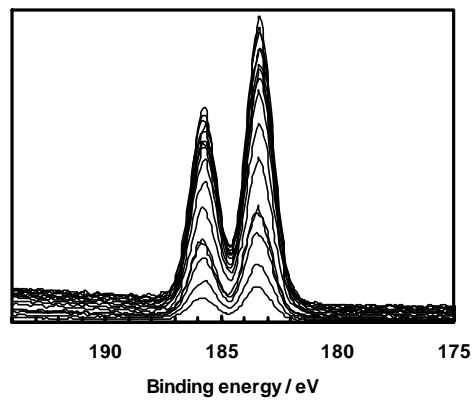


(b)

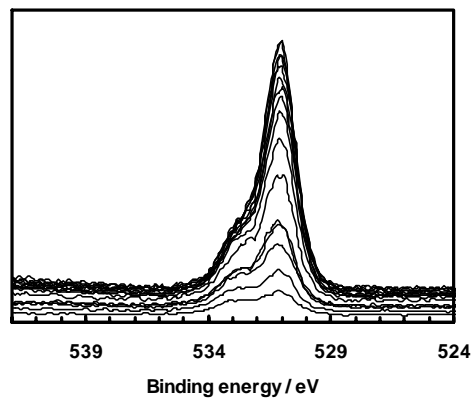


(c)

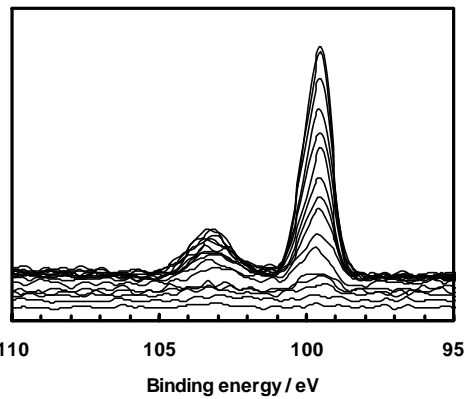
Figure 46: ARXPS of (a) Zr 3d, (b) O 1s, and (c) Si 2p spectra of 30 Å ZrO<sub>2</sub> deposited on H-Si surface at 350 °C.



(a)



(b)



(c)

Figure 47: ARXPS of (a) Zr 3d, (b) O 1s, and (c) Si 2p spectra of 30 Å ZrO<sub>2</sub> deposited on native silicon oxide surface at 350 °C.

Films deposited on different surfaces have distinctively different composition depth profiles. For the sample deposited on H-Si surfaces, an oxidized silicon signal was detected at zero depth, while both zirconium and oxygen concentration decrease continuously with increasing depth (Figure 48). The interface between the  $\text{ZrO}_2$  layer and the interfacial layer is not clearly defined. These results are consistent with the TEM observation that these films are discontinuous. However, the profile extraction process assumes smooth layers of uniform thickness. Therefore, the extracted profile in Figure 48 does not describe the sample well. Further work is already underway to improve the analysis of ARXPS data from samples with fractional coverage.

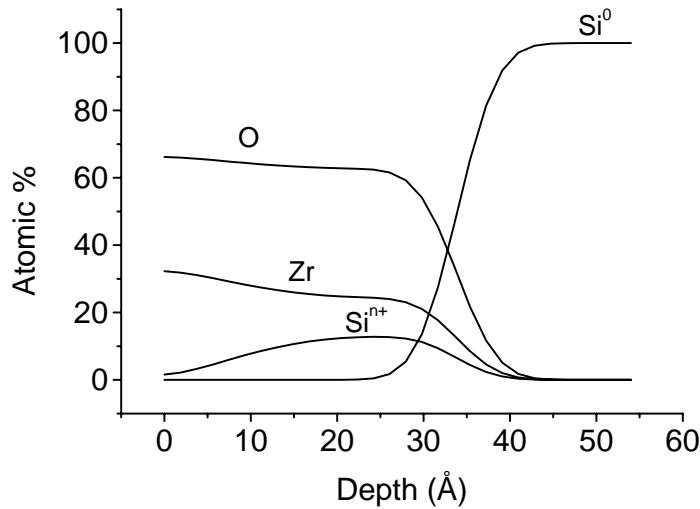


Figure 48: Elemental depth profile of a 30 Å  $\text{ZrO}_2$  film deposited on H-Si surface at 350 °C

For the sample deposited on a native silicon oxide surface, the concentration of oxygen and zirconium is constant in the  $\text{ZrO}_2$  layer (Figure 49). The O:Zr ratio of the  $\text{ZrO}_2$  layer is 1.75, indicating that the  $\text{ZrO}_2$  layer is oxygen deficient. The depth corresponding to half maximum intensity is used to define the interfaces. Using different

elements to determine the interface between the silicon substrate and the interfacial layer resulted in negligible differences in measured thicknesses. This suggests that the interface between the interfacial layer and the silicon substrate is abrupt. However, the  $\text{ZrO}_2$ /interfacial layer interface depths, defined by  $\text{Si}^{n+}$  and Zr, have a 3 Å difference, suggesting the presence of a less abrupt transition.

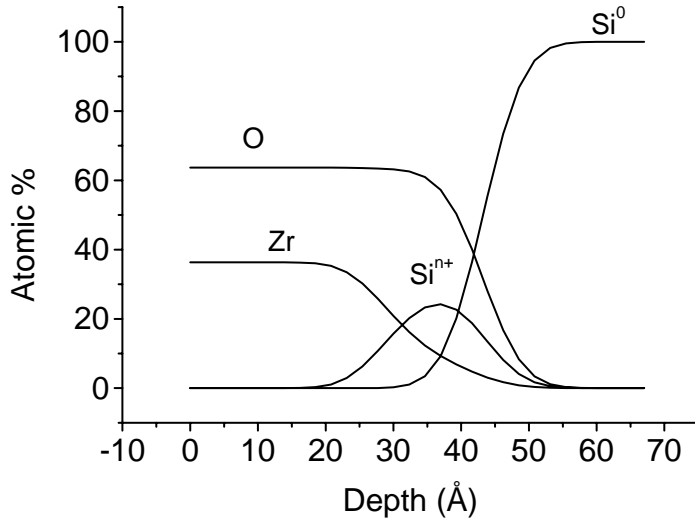


Figure 49: Elemental depth profile of a 30 Å  $\text{ZrO}_2$  film deposited on native silicon oxide surface at 350 °C

The ARXPS spectra for the two samples were also integrated over photoemission angle to give total Si 2p and O 1s intensities from each sample. The spin-orbit splitting in the Si 2p regions of interest was removed from the angle integrated spectrum. Both the O 1s and Si 2p spectra were deconvoluted to investigate the chemical bonding states of these elements. Atomic concentrations of the different bonding states identified by this process are listed in Table 5.  $\text{ZrO}_2$  films deposited on H-Si surfaces have silicon suboxide, silicate, and silicon dioxide components. The silicate component accounts for

more than 60 % of oxidized silicon. This suggests significant silicate formation at the interface.  $\text{ZrO}_2$  films deposited on native silicon oxide surfaces only have silicon suboxide and silicon dioxide components. No silicate component was observed.

Table 5: Atomic concentration (%) of elements at different chemical states

Starting surface	H-Si	Native silicon oxide
$\text{Si}_{\text{sub-oxide}}$	0.8	0.4
$\text{Si}_{\text{silicate}}$	4.2	-
$\text{Si}_{\text{oxide}}$	1.6	3.0
Zr	28.2	33.7
$\text{O}_A$	41.7	47.6
$\text{O}_B$	20.4	14.0
$\text{O}_C$	3.2	1.4

### 5.3.6 Ex-situ SE

A three-layer model, consisting of a surface roughness layer, a TL layer to represent the  $\text{ZrO}_2$  layer, and another TL layer to represent the interfacial layer, was used for data analysis. Details on this model and the data analysis methodology can be found in Chapter III and in reference<sup>139</sup>. The TL model parameters for the  $\text{ZrO}_2$  layer extracted in the previous work were used as constants for the  $\text{ZrO}_2$  TL model in this work. The TL model parameters for the interfacial layer, as well as the thickness of each layer, are set as fitting parameters. The resulting thicknesses are plotted in Figure 50 and listed in Table 4.

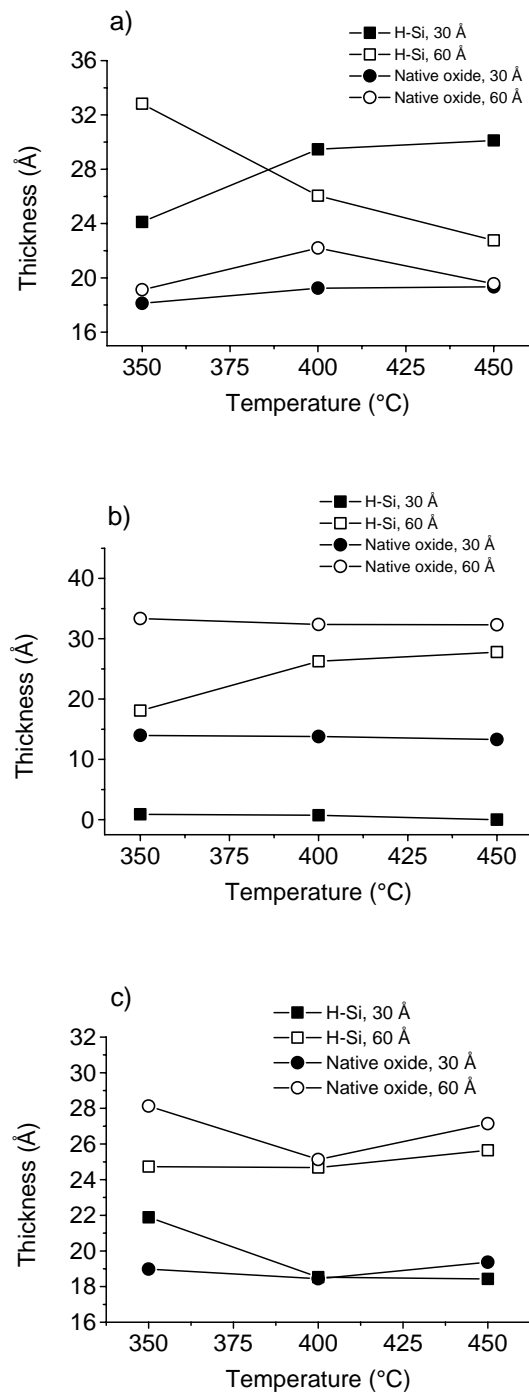


Figure 50: Ex-situ SE results of (a) surface roughness layer, (b) ZrO<sub>2</sub> layer, and (c) interfacial layer thicknesses of 30 and 60 Å ZrO<sub>2</sub> samples deposited on different surfaces and at different temperatures.

Films deposited on native silicon oxide surfaces have lower surface roughness compared to those deposited on H-Si surfaces [Figure 50(a)], consistent with AFM measurements. However, for samples deposited on H-Si surfaces, the surface roughness increase measured by AFM is not observed by SE measurements. For a given nominal film thickness, the  $\text{ZrO}_2$  layer thicknesses of films deposited on H-Si surfaces are much lower than for films deposited on native silicon oxide surfaces [Figure 50(b)]. In the studied thickness range, the interfacial layer thickness of films deposited on both H-Si and native silicon oxide surfaces increases with increasing film thickness [Figure 50(c)].

#### 5.4 Discussion

At elevated temperatures ZTB decomposes through two routes: a  $\beta$ -H-elimination reaction or a substitution reaction with surface hydroxyl groups<sup>23,101</sup>. Details on the deposition reaction mechanism can be found in Section 2.2.5.

Since the  $\beta$ -H-elimination reaction generates surface hydroxyl groups, and t-butanol readily dehydrates to form butene at elevated temperatures, the contribution of the two reactions cannot be distinctively separated during bulk deposition. However, the predominant decomposition route significantly affects the nucleation and coalescence process on different starting surfaces. In Chapter IV, modeling the evolution of void space in the deposited films led to a proposed model for the initial-stage deposition of  $\text{ZrO}_2$  on different surfaces<sup>132</sup>. Due to the ultra thin nature of deposited films, the void space inside the deposited film and the void space resulting from surface roughness cannot be separated. In the current work we comprehensively used in-situ SE, AFM, and TEM to study the details of the structures of these films.

#### **5.4.1 Nucleation and Coalescence on H-Si Surfaces**

The same in-situ SE data analysis method as in Chapter IV was used to extract void fraction evolution in this work. The void fraction of films deposited on H-Si surfaces is influenced by both deposition temperature and film thickness (Figure 36). These void fractions decrease consistently until the film thickness reaches approximately 60 Å. The void fraction of 60 Å films is in the range of 10-30 %. The nucleation and coalescence process has not reached completion for these films. This is confirmed by AFM results that show a large surface roughness increase is observed when film thickness is increased from 30 to 60 Å (Figure 39).

Void fraction can exist as either the void space inside the deposited films or as equivalent void-space in the surface roughness layer. The contribution from these two types of void space cannot be distinguished by in-situ SE measurement<sup>132</sup>. We used both cross sectional TEM and plan view TEM to further investigate the structure of deposited films. Cross sectional TEM images show that ZrO<sub>2</sub> films deposited on a H-Si surface consist of ZrO<sub>2</sub> islands (Figure 40). The 30 Å ZrO<sub>2</sub> films deposited at 350 °C on a H-Si surface consist of separated islands. The 30 Å thick film deposited at 450 °C has coalesced. Once coalesced, the ZrO<sub>2</sub> film can be divided into a surface roughness layer and a ZrO<sub>2</sub> layer.

TEM results also show the film structure evolution during ZrO<sub>2</sub> initial-stage deposition. Figure 40 and Figure 41 show the cross sectional TEM images and plan view images, respectively, of 30 Å ZrO<sub>2</sub> films. These images suggest that the initial-stage deposition of ZrO<sub>2</sub> on H-Si surfaces is a 3-D type nucleation process. During deposition on H-Si, spacing between centers of islands is conserved when the thickness increases

from 30 Å (Figure 41) to 60 Å (Figure 42). This suggests that the surface topology characteristics developed in the first 30 Å are preserved through the remainder of the initial-stage deposition process.

H-Si surfaces lack hydroxyl groups. At the onset of deposition on H-Si, ZTB molecules decompose through the  $\beta$ -H-elimination reaction, producing surface hydroxyl groups<sup>101</sup> and forming zirconium silicate clusters (more details are discussed in Section IV.C) surrounding these newly formed hydroxyl groups. Based on the topology development at the onset of deposition, the fluxes of ZTB to different sites on the substrate surface are different. The peaks of  $ZrO_2$  islands have higher ZTB fluxes, so further surface roughness development is expected for thicker films. Additionally, for a given film thickness, in-situ SE results show that the void fraction of films deposited on H-Si surfaces decreases with increasing deposition temperature. This can be explained by increased decomposition rate of ZTB at the onset of deposition. Since more hydroxyl groups are generated, more silicate clusters are formed. In brief, the relatively inert H-Si surface cannot provide enough reactive hydroxyl groups at the onset of deposition to facilitate a layer-by-layer deposition. Instead, the formation of separated reactive surface hydroxyl group clusters facilitates a 3-D nucleation process, resulting in a nonuniform film. A detailed discussion was published in our earlier report<sup>132</sup>.

#### **5.4.2 Nucleation and Coalescence on Native Silicon Oxide Surfaces**

For films deposited on native silicon oxide surfaces, the void fraction is influenced only by film thickness (Figure 37). The void fraction of films deposited on native silicon oxide surfaces drops to zero in the thickness range of 30 - 40 Å. Thereafter,

the void fraction remains constant up to 80 Å thickness. This suggests that ZrO<sub>2</sub> deposition on native silicon oxide surfaces is a layer-by-layer process, or alternatively, that the ZrO<sub>2</sub> films have completed the initial nucleation and coalescence process at thicknesses lower than 30 Å.

Since the void fraction mentioned above are relative values, the absolute void space in these samples increases with film thickness. Additionally, because the void fractions of these films are almost zero, the films deposited on the native silicon oxide surface have high densities. AFM measurements indicate that the surface roughness increases slightly with increasing film thickness (Figure 39). Therefore, void space in these films exists mainly as the void components in the surface roughness layer.

TEM images show no thickness variations, as might arise from ZrO<sub>2</sub> islands, for the 30 Å sample deposited on a native silicon oxide surfaces. The film deposited on native silicon oxide at 350 °C has a flat top surface. The sample deposited at 450 °C shows some contrast variation on the top surface, but a surface roughness layer cannot be clearly defined.

Figure 40 and Figure 41 contain the cross sectional TEM images and plan view images of 30 Å ZrO<sub>2</sub> films. No surface topology development is shown in these figures. Surface roughness increase is limited. Plan view images of 60 Å ZrO<sub>2</sub> films deposited on native silicon oxide surfaces show that these films have fully coalesced. No large separated islands or grains, like those seen on H-Si surfaces, were observed. These results agree with the in-situ SE and AFM results. We infer, therefore, that the initial-stage deposition of ZrO<sub>2</sub> on native silicon oxide surfaces is a layer-by-layer deposition process. In brief, a high-density of surface hydroxyl groups on native silicon oxide surfaces

provides active reaction sites for ZTB molecules. ZTB molecules first react with surface hydroxyl groups, and then undergo a  $\beta$ -H-elimination reaction to form a uniform monolayer (Equations 1 to 4), resulting in a high-density, low surface roughness  $ZrO_2$  films.

#### 5.4.3 Formation of the Interfacial Layer

In addition to film structure, the formation of interfacial layers between high-k dielectric layers and the silicon substrate is important in high-k gate dielectric applications. Although thermodynamic calculations suggest that  $ZrO_2$  is stable in direct contact with  $Si^{39}$ , the formation of an interfacial layer on H-Si surfaces has been observed. The thickness of these interfacial layers is influenced by both deposition temperature and starting surface.

Table 4 Thicknesses of some samples measured by different methods shows that 30 Å films deposited at 350 °C on H-Si surface have a thicker interfacial layer than those deposited at 450 °C. However, for samples deposited on native silicon oxide surfaces, the interfacial layer thickness is not influenced by deposition temperature. These results suggest that interfacial layers on the different surfaces are formed through different mechanisms.

TOF MEBS (Figure 45) analyses show that the interfacial layer of films deposited on H-Si surfaces contain more zirconium atoms than those deposited on native silicon oxide surfaces. This result is confirmed by ARXPS (Figure 48). Additionally, ARXPS shows that the interfacial layer of a sample deposited on H-Si contains silicate components (Table 5). These results suggest that at the onset of deposition ZTB or its

decomposition intermediates react with the H-Si surface and form an interfacial silicate layer. For  $ZrO_2$  films deposited on native silicon oxide surfaces, ARXPS shows that the interfacial layer is composed of silicon oxide and suboxides. No silicate components were observed. These results suggest that ZTB or its decomposition intermediates do not participate in the formation of interfacial layers on native silicon oxide surfaces.

An abrupt interface forms on the native silicon oxide surfaces due to ZTB reacting with the hydroxyl groups on the native silicon oxide surfaces. Ex-situ SE results show that the interfacial layer thickness increases with film thickness for films deposited on both H-Si and native silicon oxide surfaces (Figure 50). At the identical deposition conditions, thicker films are exposed to the deposition process longer. Therefore, the time that the substrate is exposed to deposition chemicals affects the interfacial layer thickness. Chemicals in the deposition chamber can diffuse through the forming  $ZrO_2$  layer and react with the silicon substrate. Since the interfacial layer of films deposited on native silicon oxide surfaces are composed of silicon suboxides only, water formed during ZTB decomposition may be reacting with the silicon substrate in that case. Therefore, the formation of the interfacial layer involves two mechanisms: 1) ZTB or its decomposition intermediates react with H-Si or native silicon oxide surfaces; 2) water or other oxidants diffuse through the forming  $ZrO_2$  and interfacial layers to react with the silicon substrate. Therefore, a metal oxide oxygen barrier with higher dielectric constant than  $SiO_2$ , such as  $Al_2O_3$ , may be necessary for high-k gate dielectric applications<sup>5</sup>.

#### **5.4.4 Discussion of Characterization Methods**

The target thickness for high-k gate dielectric films is in the range of a few nanometers. We have shown that the uniformity of these films is highly affected by deposition conditions and starting surfaces. Extra consideration of the modeling and limitations of tools must be made during characterization. Table 4 contains selected results obtained by different tools used in this study. Values in the physical measurements columns are either AFM (surface roughness values) or TEM (film thickness) measurements. The results obtained from other tools are compared to these physical measurements. Generally, ex-situ SE, ToF MEBS, and ARXPS results are closer to the physical measurements for the samples deposited on native silicon oxide surfaces as compared to results from samples deposited on H-Si surfaces. The complicated structure of ZrO<sub>2</sub> films deposited on H-Si surfaces makes it difficult to interpret ARXPS and TOF MEBS data because a uniform film structure is assumed in typical data analysis. In addition, ToF MEBS thickness measurement is also limited by depth resolution, and unavailable interfacial layer densities. For samples deposited on both H-Si and native silicon oxide surfaces, ex-situ SE gives fairly accurate interfacial layer thickness compared to the physical measurements. The difficulty for ex-situ SE analyses lies in the determination of the surface roughness layer. AFM results indicate that the surface roughness of these samples is less than 10 Å, which is below the resolution limit of our visible to near ultra violet ellipsometer<sup>110</sup>. Edwards' report has shown that vacuum ultra violet SE has advantages in determining the thickness of such ultra-thin surface roughness layers <sup>140</sup>. In SE modeling, the interfacial layer are more important for long wavelength measurements, while surface roughness is more important for short

wavelength measurements, such as measurements in vacuum ultraviolet range <sup>140</sup>. In 1.25 – 6.5 eV photon energy range, our ex-situ measurements infer a higher surface roughness layer thickness than physical measurements. However, the sums of the ZrO<sub>2</sub> layer and the surface roughness layer thickness are nearly identical to the physical measurements. For samples deposited on H-Si surfaces, due to excessive 3-D type nucleation, the SE surface roughness layer accounts for a large portion of film thickness. The surface roughness measurements are close to the physical measurements in this case.

Additionally, in-situ SE results show that the void fractions of 30 Å thick films deposited on H-Si surface are 5-10 time higher than for films deposited on native silicon oxide surfaces. Therefore, a 5-10 times higher surface roughness could be expected for films deposited on H-Si surfaces. However, only a slight surface roughness increase is measured by AFM (Figure 39). This difference can be explained by either ZrO<sub>2</sub> layer density or the finite AFM tip size. Films deposited on H-Si surface have high void fractions. The void can either exist in the ZrO<sub>2</sub> layer or in the surface roughness layer. The void fraction is not directly related to surface roughness unless the films are high-density films like those deposited on native silicon oxide surfaces. TEM results show that the grain sizes of 30 Å films deposited on the H-Si surface are less than 50 Å. Since the radius of curvature of AFM tips is approximately 20 Å, the finite tip size could be a limitation for AFM measurements. Despite these limitations, AFM results support those obtained from in-situ SE measurements.

In brief, high-k gate dielectric applications require accurate measurement of ultra thin films. This can be challenging for some typical surface characterization tools due to

both instrumental limitations and the complex structure of these ultra thin films. Careful confirmation of the results from different surface analysis tools is necessary.

## 5.5 Conclusions

We used in-situ and ex-situ SE, AFM, TEM, ToF MEBS, and ARXPS to study the properties of 30 and 60 Å thick ZrO<sub>2</sub> films deposited at different temperatures on H-Si and native silicon oxide surfaces. Results show that the initial-stage depositions of ZrO<sub>2</sub> on H-Si and native silicon oxide surfaces are different. A 3-D nucleation process of ZrO<sub>2</sub> on H-Si results in high surface roughness films, while a layer-by-layer deposition on native silicon oxide surfaces results in uniform ZrO<sub>2</sub> films. The interfacial layer is formed through two independent mechanisms: the reaction between ZTB or its decomposition intermediates with the starting surface, and the diffusion of reactive oxidants through the ultra thin ZrO<sub>2</sub> layer and the newly formed interfacial layer down to the silicon substrate to form silicon suboxide. We also compare the thickness measurement results obtained from different tools and discuss their limitations.

## CHAPTER VI

### CONCLUSIONS AND RECOMMENDATIONS

When we started this project, much of the attention in the field was focused on material selection and the physical properties of desired materials, such as band offsets, band gap, and dielectric constants. Over the last few years, more and more evidence has shown that the high-k dielectric deposition process strongly influences film properties. ALCVD, MBE, and MOCVD are candidate processes for high-k gate dielectrics since they do not damage the silicon substrate. All of these deposition processes are also expected to be able to deposit high-k dielectric films with controlled microstructure, thickness, and properties. However, as we showed in Chapter II, these processes are all strongly affected by the factors during the initial-stage deposition, such as chemical reaction, nucleation, and coalescence. We chose ZrO<sub>2</sub> as the gate dielectric material and HV-CVD as the deposition method to study the details of the initial-stage deposition, and gave a general description of the initial-stage deposition of ZrO<sub>2</sub> on different surfaces.

The ultra thin nature and the complicated structure of high-k gate dielectric films make it challenging for both deposition and characterization. We developed both in-situ and ex-situ SE characterization methodologies for high-k gate dielectric films. We first developed a methodology to characterize ZrO<sub>2</sub> films deposited on the silicon substrate using ex-situ SE. We demonstrated that proper modeling of the optical properties of the interfacial layer is the key to accurate ellipsometric characterization of ZrO<sub>2</sub> films. Based on a stacking model consisting of an EMA surface-roughness layer, a TL layer to represent the ZrO<sub>2</sub> layer, and a second TL layer to represent the interfacial layer, we

extracted the thickness of each layer in the three-layer stack structure. The extracted thickness and effective surface-roughness values were in good agreement with physical measurements, including AFM and TEM results. We separated the optical constants of  $\text{ZrO}_2$  from those of the interfacial layer, and uniquely extracted TL parameters to depict the optical constants of  $\text{ZrO}_2$ , which were consistent with published data. We also extracted the optical constants of the interfacial layer from  $\text{ZrO}_2$  samples deposited by HV-CVD under tight environment control. The optical constants of the interfacial layer suggest that the interfacial layer is a non-stoichiometric zirconium silicate.

Thereafter, we used in-situ SE method to study the initial stage deposition process of  $\text{ZrO}_2$  from ZTB on both native silicon oxide and H-Si surfaces. We compared the results obtained from different SE models to the results from AFM, and discussed the issues for in-situ SE characterization on ultra thin  $\text{ZrO}_2$  films during the initial-stage deposition. We extracted the optical constant of high-density  $\text{ZrO}_2$  films during deposition. We discovered that  $\text{ZrO}_2$  films deposited of native silicon oxide surfaces have higher refractive indexes and film densities. We showed that different nucleation and coalescence processes during the initial-stage deposition on different surfaces affect the properties of the deposited films. On H-Si surfaces, the lack of reactive surface hydroxyl groups and high surface diffusivity of ZTB molecules lead to 3-D nucleation process. The resulting films have high surface roughness, and are inappropriate for gate dielectric applications. On native silicon oxide surface, the highly reactive hydroxyl groups react with ZTB molecules to form a high-density layer on the top of native silicon oxide surface. At temperatures higher than the decomposition temperature of the t-butoxy group, further 3-D nucleation of  $\text{ZrO}_2$  is suppressed. The resulting films have low void

fraction and low topology development, and are more suitable for gate dielectric applications.

Finally, we comprehensively used complementary characterization tools, including in-situ and ex-situ SE, AFM, TEM, ToF MEBS, and ARXPS, to study the properties of 30 and 60 Å thick ZrO<sub>2</sub> films deposited at different temperatures on H-Si and native silicon oxide surfaces. This further proved the initial-stage deposition model we proposed in Chapter IV. Results show that the initial-stage depositions of ZrO<sub>2</sub> on H-Si and native silicon oxide surfaces are different. A 3-D nucleation process of ZrO<sub>2</sub> on H-Si results in high surface roughness films, while a layer-by-layer deposition on native silicon oxide surfaces results in uniform ZrO<sub>2</sub> films. The interfacial layer is formed through two independent mechanisms: the reaction between ZTB or its decomposition intermediates with the starting surface, and the diffusion of reactive oxidants through the ultra thin ZrO<sub>2</sub> layer and the newly formed interfacial layer down to the silicon substrate to form silicon suboxide. We also compare the thickness measurement results obtained from different tools and discuss their limitations.

In summary, this work developed methodologies to characterize deposited films by both in-situ real-time monitoring, and ex-situ characterization methods, investigated details of the initial-stage deposition of ZrO<sub>2</sub> on different surfaces, and discovered the mechanism of the formation of interfacial layers between ZrO<sub>2</sub> films and the silicon substrate. I have the following recommendations for future work:

- 1) Use Al<sub>2</sub>O<sub>3</sub> as the interfacial layer. The interfacial layer between high-k films and the silicon substrate are critical for successful replacement of the gate silicon dioxide dielectric layer. The bonding constraint theory suggests that an amorphous interfacial

layer will relax the bonding constraints on the interface. We showed that silicate interfacial layer could be formed during deposition. Although silicates have higher dielectric constants than silicon dioxide, the properties and uniformity of these silicate interfacial layers are major problems. The deposition results on native silicon oxide surfaces showed that a hydroxyl group terminated surface is necessary to form uniform  $\text{ZrO}_2$  films. However, the native silicon oxide layer strongly degrades the effective dielectric constant of the gate dielectric structure. Additionally, our results demonstrated that the interfacial layer is formed through two mechanisms: the reaction between precursor and the silicon substrate, the diffusion of oxidant into the silicon substrate. When we consider all of these results, the use of an interfacial  $\text{Al}_2\text{O}_3$  layer becomes the first topic for future research.  $\text{Al}_2\text{O}_3$  has a higher dielectric constant ( $k = 8$ ) than silicon dioxide, and is an excellent oxygen barrier.  $\text{Al}_2\text{O}_3$  is also an amorphous material, which could help relax the bonding constraints. ALCVD results have shown that  $\text{Al}_2\text{O}_3$  deposition on H-Si also has a transition period at the beginning of deposition<sup>67</sup>. This suggests that  $\text{Al}_2\text{O}_3$  deposition may also have issues for the initial-stage deposition. However, details need to be investigated.

2) In-situ surface preparation. Wet cleaning, such as RCA cleaning<sup>109</sup>, is a standard method before growing thermal silicon dioxide. The resulting surface is a H-terminated silicon surface. Our results showed that a hydroxyl groups terminated surface or oxidized surface is necessary for depositing uniform  $\text{ZrO}_2$  films. Although the films deposited on native silicon oxide surfaces showed preferable properties, the 10-20 Å interfacial oxide layer is not acceptable. Effort must be made to minimize the thickness of such interfacial layers. A direct method is to oxidize the silicon surface under vacuum.

This needs in-situ characterization tools, such as XPS, AES, to be integrated on to our deposition system.

3) Electrical characterization. The electrical characterization is beyond the scope of this work. The discussion of processing conditions and properties in this work are based on an understanding of the chemical composition and the microstructure of films. These properties only partially satisfy the requirements of high-k gate dielectric films. More properties, such as interfacial state density, flat-band voltage, fixed charge density, and so on, require detailed electrical characterization. Additionally, we have used complementary physical characterization tools to study the properties of films. Detailed results from electrical characterization will help to link processing condition, physical characterization results, and electrical properties together, and will be very useful for process improvement.

4) Integration with strained silicon surfaces. In the last few years, several technologies were developing simultaneously. One of the more and more accepted technologies is strained silicon<sup>141</sup>. Carrier mobility degradation is still a significant challenge for high-k dielectric integration. Strained silicon has shown improved carrier mobility compared with the silicon substrate<sup>141,142</sup>. Therefore, using strained silicon will potentially help ease the stringent requirements on high-k dielectric/Si interfacial properties. The strained silicon layers (typically < 20 nm) are often grown on relaxed SiGe substrates under UHV-CVD condition<sup>142</sup>. Therefore, our deposition system can potentially integrate strained silicon deposition, pre-high-k dielectric deposition surface preparation, and high-k dielectric into one process.

## REFERENCES

- <sup>1</sup> R. H. Dennard, Gaensle.Fh, H. N. Yu, V. L. Rideout, E. Bassous, and A. R. Leblanc, IEEE J. Solid-State Circuit **SC 9**, 256-268 (1974).
- <sup>2</sup> *The National Technology Roadmap for Semiconductors Technology Needs*, 1997 ed. (Semiconductor Industry Association, San Jose, CA, 1997).
- <sup>3</sup> *International Technology Roadmap for Semiconductors*, 2003 ed. (International SEMATECH, Austin, TX, 2003).
- <sup>4</sup> M. Morgen, E. T. Ryan, J. H. Zhao, C. Hu, T. H. Cho, and P. S. Ho, Annu. Rev. Mater. Sci. **30**, 645-680 (2000).
- <sup>5</sup> G. D. Wilk, R. M. Wallace, and J. M. Anthony, J. Appl. Phys. **89**, 5243-5275 (2001).
- <sup>6</sup> S. J. Tans, A. R. M. Verschueren, and C. Dekker, Nature **393**, 49-52 (1998).
- <sup>7</sup> P. C. Collins, M. S. Arnold, and P. Avouris, Science **292**, 706-709 (2001).
- <sup>8</sup> P. M. Solomon, Annu. Rev. Mater. Sci. **30**, 681-697 (2000).
- <sup>9</sup> R. S. Muller and T. I. Kamins, *Device Electronics for Integrated Circuits*, 2nd ed. (Wiley, New York, 1986).
- <sup>10</sup> G. E. Moore, Proc. IEEE **86**, 82-85 (1998).
- <sup>11</sup> "Front End Processes," in *International Technology Roadmap for Semiconductors*, 2003 ed. (International SEMATECH, Austin, TX, 2003), p. 24.
- <sup>12</sup> J. D. Plummer and P. B. Griffin, Proc. IEEE **89**, 240-258 (2001).
- <sup>13</sup> M. L. Green, T. W. Sorsch, G. L. Timp, D. A. Muller, B. E. Weir, P. J. Silverman, S. V. Moccio, and Y. O. Kim, Microelectron. Eng. **48**, 25-30 (1999).
- <sup>14</sup> H. E. Maes, G. Groeseneken, R. Degraeve, J. De Blauwe, and G. Van den Bosch, Microelectron. Eng. **40**, 147-166 (1998).
- <sup>15</sup> H. Iwai, Microelectron. Eng. **48**, 7-14 (1999).
- <sup>16</sup> D. A. Buchanan, IBM J. Res. Dev. **43**, 245-264 (1999).
- <sup>17</sup> J. F. Scott, Annu. Rev. Mater. Sci. **28**, 79-100 (1998).

- <sup>18</sup> A. Y. Mao, K. A. Son, D. A. Hess, L. A. Brown, J. M. White, D. L. Kwong, D. A. Roberts, and R. N. Vrtis, *Thin Solid Films* **349**, 230-237 (1999).
- <sup>19</sup> S. A. Campbell, H. S. Kim, D. C. Gilmer, B. He, T. Ma, and W. L. Gladfelter, *IBM J. Res. Dev.* **43**, 383-392 (1999).
- <sup>20</sup> M. Hartmanova, K. Gmucova, M. Jergel, I. Thurzo, F. Kundracik, and M. Brunel, *Thin Solid Films* **345**, 330-337 (1999).
- <sup>21</sup> A. Chin, C. C. Liao, C. H. Lu, W. J. Chen, and C. Tsai, *Digest of Technical Papers - Symposium on VLSI Technology*, 135-136 (1999).
- <sup>22</sup> J. Robertson, *Integr. Ferroelectr.* **32**, 943-950 (2001).
- <sup>23</sup> M. A. Cameron and S. M. George, *Thin Solid Films* **348**, 90-98 (1999).
- <sup>24</sup> M. Houssa, V. V. Afanas'ev, A. Stesmans, and M. M. Heyns, *Appl. Phys. Lett.* **77**, 1885-1887 (2000).
- <sup>25</sup> C. M. Perkins, B. B. Triplett, P. C. McIntyre, K. C. Saraswat, S. Haukka, and M. Tuominen, *Appl. Phys. Lett.* **78**, 2357-2359 (2001).
- <sup>26</sup> G. D. Wilk and R. M. Wallace, *Appl. Phys. Lett.* **76**, 112-114 (2000).
- <sup>27</sup> G. D. Wilk and R. M. Wallace, *Appl. Phys. Lett.* **74**, 2854-2856 (1999).
- <sup>28</sup> G. D. Wilk, R. M. Wallace, and J. M. Anthony, *J. Appl. Phys.* **87**, 484-492 (2000).
- <sup>29</sup> M. Itsumi, S. Ohfuji, M. Tsukada, and H. Akiya, *J. Electrochem. Soc.* **144**, 4321-4325 (1997).
- <sup>30</sup> R. Liu, S. Zollner, P. Fejes, R. Gregory, S. Lu, K. Reid, D. Gilmer, B.-Y. Nguyen, Z. Yu, R. Droopad, J. Curless, A. Demkov, J. Finder, and K. Eisenbeiser, *Mat. Res. Soc. Symp. Proc.* **670**, K1.1.1 - K1.1.13 (2001).
- <sup>31</sup> R. M. Wallace and G. Wilk, *MRS Bull.* **27**, 186-187 (2002).
- <sup>32</sup> D. G. Schlom and J. H. Haeni, *MRS Bull.* **27**, 198-204 (2002).
- <sup>33</sup> B. W. Busch, O. Pluchery, Y. J. Chabal, D. A. Muller, R. L. Opila, J. R. Kwo, and E. Garfunkel, *MRS Bull.* **27**, 206-211 (2002).
- <sup>34</sup> V. Misra, G. Lucovsky, and G. Parsons, *MRS Bull.* **27**, 212-216 (2002).
- <sup>35</sup> J. Robertson, *J. Vac. Sci. Technol. B* **18**, 1785-1791 (2000).
- <sup>36</sup> R. Degraeve, E. Cartier, T. Kauerauf, R. Carter, L. Pantisano, A. Kerber, and G. Groeseneken, *MRS Bull.* **27**, 222-225 (2002).

- <sup>37</sup> R. D. Shannon, J. Appl. Phys. **73**, 348-366 (1993).
- <sup>38</sup> *CRC Handbook of Chemistry and Physics*; Vol., edited by D. R. Lide (CRC Press, Boca Raton, FL, 2004).
- <sup>39</sup> K. J. Hubbard and D. G. Schlom, J. Mater. Res. **11**, 2757-2776 (1996).
- <sup>40</sup> G. Lucovsky, Y. Wu, H. Niimi, V. Misra, and J. C. Phillips, Appl. Phys. Lett. **74**, 2005-2007 (1999).
- <sup>41</sup> G. Lucovsky and J. C. Phillips, Microelectron. Eng. **48**, 291-294 (1999).
- <sup>42</sup> G. Lucovsky and J. C. Phillips, Appl. Surf. Sci. **166**, 497-503 (2000).
- <sup>43</sup> V. Misra, H. Lazar, Z. Wang, Y. Wu, H. Niimi, G. Lucovsky, J. J. Wortman, and J. R. Hauser, J. Vac. Sci. Technol. B **17**, 1836-1839 (1999).
- <sup>44</sup> G. Lucovsky, H. Niimi, Y. Wu, and H. Yang, Appl. Surf. Sci. **159-160**, 50-61 (2000).
- <sup>45</sup> H. Niimi and G. Lucovsky, J. Vac. Sci. Technol. B **17**, 2610-2621 (1999).
- <sup>46</sup> G. Lucovsky, J. Vac. Sci. Technol. A **17**, 1340-1351 (1999).
- <sup>47</sup> G. Lucovsky, H. Yang, H. Niimi, M. F. Thorpe, and J. C. Phillips, J. Vac. Sci. Technol. B **18**, 2179-2186 (2000).
- <sup>48</sup> Y. Lee, M. Park, and J. Song, Semicond. Int. (2001).
- <sup>49</sup> K. Chu, J. P. Chang, M. L. Steigerwald, R. M. Fleming, R. L. Opila, D. V. Lang, R. B. V. Dover, and C. D. W. Jones, J. Appl. Phys. **91**, 308-316 (2002).
- <sup>50</sup> C. T. Sah, L. L. Tsopp, and T. H. Ning, Surf. Sci. **32**, 561-& (1972).
- <sup>51</sup> "Front End Processes," in *International Technology Roadmap for Semiconductors*, 2003 ed. (International SEMATECH, Austin, TX, 2003), p. 17.
- <sup>52</sup> V. Craciun, J. M. Howard, N. D. Bassim, and R. K. Singh, Appl. Surf. Sci. **168**, 123-126 (2000).
- <sup>53</sup> R. A. McKee, F. J. Walker, and M. F. Chisholm, Phys. Rev. Lett. **81**, 3014-3017 (1998).
- <sup>54</sup> S. J. Wang, C. K. Ong, S. Y. Xu, P. Chen, W. C. Tjiu, A. C. H. Huan, W. J. Yoo, J. S. Lim, W. Feng, and W. K. Choi, Semicond. Sci. Technol. **16**, L13-L16 (2001).
- <sup>55</sup> T. Ngai, W. J. Qi, R. Sharma, J. Fretwell, X. Chen, J. C. Lee, and S. Banerjee, Appl. Phys. Lett. **76**, 502-504 (2000).

- <sup>56</sup> S. B. Qadri, J. S. Horwitz, D. B. Chrisey, E. P. Donovan, and E. F. Skelton, *Sur. Coat. Technol.* **86-87**, 149-152 (1996).
- <sup>57</sup> A. S. Gandhi, V. Jayaram, and A. H. Chokshi, *Mater. Sci. Eng. A-Struct. Mater. Prop. Microstruct. Process.* **304**, 785-789 (2001).
- <sup>58</sup> M. J. Weber, *Handbook of Optical Materials* (CRC Press, Boca Raton, 2003).
- <sup>59</sup> M. Copel, M. Gribelyuk, and E. Gusev, *Appl. Phys. Lett.* **76**, 436-438 (2000).
- <sup>60</sup> J. P. Chang, Y. S. Lin, S. Berger, A. Kepten, R. Bloom, and S. Levy, *J. Vac. Sci. Technol. B* **19**, 2137-2143 (2001).
- <sup>61</sup> J. P. Chang, Y.-S. Lin, and K. Chu, *J. Vac. Sci. Technol. B* **19**, 1782-1787 (2001).
- <sup>62</sup> H. W. Chen, T. Y. Huang, D. Landheer, X. Wu, S. Moisa, G. I. Sproule, and T. S. Chao, *J. Electrochem. Soc.* **149**, F49-F55 (2002).
- <sup>63</sup> W. Chism, A. Diebold, J. Canterbury, and C. Richter, "Characterization and production metrology of thin transistor gate dielectric films," in *Ultra Clean Processing of Silicon Surfaces 2000; Vol. 76-77* (Scitec Publications Ltd, Uetikon-Zuerich, 2001), p. 177-180.
- <sup>64</sup> *Science and Technology of Zirconia; Vol.*, edited by A. H. Heuer, L. W. Hobbs, Case Institute of Technology. Ceramics Group, and American Ceramic Society. (American Ceramic Society, Columbus, Ohio, 1981).
- <sup>65</sup> S. A. Campbell, *The Science and Engineering of Microelectronic Fabrication* (Oxford University Press, New York, 1996).
- <sup>66</sup> S. K. Dey, C. G. Wang, D. Tang, M. J. Kim, R. W. Carpenter, C. Werkhoven, and E. Shero, *J. Appl. Phys.* **93**, 4144-4157 (2003).
- <sup>67</sup> W. Tsai, R. J. Carter, H. Nohira, M. Caymax, T. Conard, W. Cosnier, S. DeGendt, M. Heyns, J. Petry, O. Richard, W. Vandervorst, E. Young, C. Zhao, J. Maes, M. Tuominen, W. H. Schulte, E. Garfunkel, and T. Gustafsson, *Microelectron. Eng.* **65**, 259-272 (2003).
- <sup>68</sup> G. Scarel, S. Ferrari, S. Spiga, C. Wiemer, G. Tallarida, and M. Fanciulli, *J. Vac. Sci. Technol. A* **21**, 1359-1365 (2003).
- <sup>69</sup> M. Ritala and M. Leskela, *Appl. Surf. Sci.* **75**, 333-340 (1994).
- <sup>70</sup> K. Kukli, M. Ritala, and M. Leskela, *Chem. Vapor Depos.* **6**, 297-302 (2000).
- <sup>71</sup> K. Kukli, K. Forsgren, J. Aarik, T. Uustare, A. Aidla, A. Niskanen, M. Ritala, M. Leskela, and A. Harsta, *J. Cryst. Growth* **231**, 262-272 (2001).

- <sup>72</sup> S. Ferrari, D. T. Dekadjevi, S. Spiga, G. Tallarida, C. Wiemer, and M. Fanciulli, *J. Non-Cryst. Solids* **303**, 29-34 (2002).
- <sup>73</sup> R. Matero, M. Ritala, M. Leskela, A. C. Jones, P. A. Williams, J. F. Bickley, A. Steiner, T. J. Leedham, and H. O. Davies, *J. Non-Cryst. Solids* **303**, 24-28 (2002).
- <sup>74</sup> J. Niinisto, M. Putkonen, L. Niinisto, K. Kukli, M. Ritala, and M. Leskela, *J. Appl. Phys.* **95**, 84-91 (2004).
- <sup>75</sup> M. Putkonen, T. Sajavaara, J. Niinisto, L. S. Johansson, and L. Niinisto, *J. Mater. Chem.* **12**, 442-448 (2002).
- <sup>76</sup> M. Putkonen, J. Niinisto, K. Kukli, T. Sajavaara, M. Karppinen, H. Yamauchi, and L. Niinisto, *Chem. Vapor Depos.* **9**, 207-212 (2003).
- <sup>77</sup> M. Putkonen and L. Niinisto, *J. Mater. Chem.* **11**, 3141-3147 (2001).
- <sup>78</sup> A. Nakajima, T. Kidera, H. Ishii, and S. Yokoyama, *Appl. Phys. Lett.* **81**, 2824-2826 (2002).
- <sup>79</sup> H. Ishii, A. Nakajima, and S. Yokoyama, *J. Appl. Phys.* **95**, 536-542 (2004).
- <sup>80</sup> E. P. Gusev, E. Cartier, D. A. Buchanan, M. Gribelyuk, M. Copel, H. Okorn-Schmidt, and C. D'Emic, *Microelectron. Eng.* **59**, 341-349 (2001).
- <sup>81</sup> M. Cassir, F. Goubin, C. Bernay, P. Vernoux, and D. Lincot, *Appl. Surf. Sci.* **193**, 120-128 (2002).
- <sup>82</sup> O. Renault, D. Samour, D. Rouchon, P. Holliger, A. M. Papon, D. Blin, and S. Marthon, *Thin Solid Films* **428**, 190-194 (2003).
- <sup>83</sup> H. Kim, *J. Vac. Sci. Technol. B* **21**, 2231-2261 (2003).
- <sup>84</sup> E. P. Gusev, E. Cartier, D. A. Buchanan, M. Gribelyuk, M. Copel, H. Okorn-Schmidt, and C. D'Emic, *Microelectron. Eng.* **59**, 341-349 (2001).
- <sup>85</sup> Y. S. Lin, R. Puthenkovilakam, J. P. Chang, C. Bouldin, I. Levin, N. V. Nguyen, J. Ehrstein, Y. Sun, P. Pianetta, T. Conard, W. Vandervorst, V. Venturo, and S. Selbrede, *J. Appl. Phys.* **93**, 5945-5952 (2003).
- <sup>86</sup> S. J. Wang, C. K. Ong, S. Y. Xu, P. Chen, W. C. Tjiu, J. W. Chai, A. C. H. Huan, W. J. Yoo, J. S. Lim, W. Feng, and W. K. Choi, *Appl. Phys. Lett.* **78**, 1604-1606 (2001).
- <sup>87</sup> J. P. Maria, D. Wicaksana, A. I. Kingon, B. Busch, H. Schulte, E. Garfunkel, and T. Gustafsson, *J. Appl. Phys.* **90**, 3476-3482 (2001).
- <sup>88</sup> S. Miyazaki, M. Narasaki, M. Ogasawara, and M. Hirose, *Microelectron. Eng.* **59**, 373-378 (2001).

- 89 J. H. Hong, W. J. Choi, and J. M. Myoung, Microelectron. Eng. **70**, 35-40 (2003).
- 90 T. Kubota, N. Hara, and K. Sugimoto, J. Electrochem. Soc. **148**, C632-C639 (2001).
- 91 J. J. Gallegos, T. L. Ward, T. J. Boyle, M. A. Rodriguez, and L. P. Francisco, Chem. Vapor Depos. **6**, 21-26 (2000).
- 92 Z. Xue, B. A. Vaartstra, K. G. Caulton, M. H. Chisholm, and D. L. Jones, Eur. J. Solid State Inorg. Chem. **29**, 213-225 (1992).
- 93 D. J. Burleson, J. T. Roberts, W. L. Gladfelter, S. A. Campbell, and R. C. Smith, Chem. Mat. **14**, 1269-1276 (2002).
- 94 M. Pulver, W. Nemetz, and G. Wahl, Surf. Coat. Technol. **125**, 400-406 (2000).
- 95 M. Balog and M. Schieber, Thin Solid Films **47**, 109-120 (1977).
- 96 S. Harasek, H. D. Wanzenboeck, B. Basnar, J. Smoliner, J. Brenner, H. Stoeri, E. Gornik, and E. Bertagnolli, Thin Solid Films **414**, 199-204 (2002).
- 97 X. Wu, D. Landheer, M. J. Graham, H. W. Chen, T. Y. Huang, and T. S. Chao, J. Cryst. Growth **250**, 479-485 (2003).
- 98 A. C. Jones, T. J. Leedham, P. J. Wright, D. J. Williams, M. J. Crosbie, H. O. Davies, K. A. Fleeting, and P. O'Brien, J. European Ceram. Soc. **19**, 1431-1434 (1999).
- 99 M. Morstein, I. Pozsgai 1, and N. D. Spencer, Chem. Vapor Depos. **5**, 151-158 (1999).
- 100 E. Fredriksson and K. Forsgren, Sur. Coat. Technol. **88**, 255-263 (1997).
- 101 D. C. Bradley and M. M. Faktor, Trans. Faraday Soc. **55**, 2117 - 2123 (1959).
- 102 S. Harasek, H. D. Wanzenboeck, and E. Bertagnolli, J. Vac. Sci. Technol. A **21**, 653-659 (2003).
- 103 T. S. Jeon, J. M. White, and D. L. Kwong, Appl. Phys. Lett. **78**, 368-370 (2001).
- 104 Y. M. Sun, J. Lozano, H. Ho, H. J. Park, S. Veldman, and J. M. White, Appl. Surf. Sci. **161**, 115-122 (2000).
- 105 W. J. Qi, R. Nieh, B. H. Lee, L. G. Kang, Y. Jeon, and J. C. Lee, Appl. Phys. Lett. **77**, 3269-3271 (2000).
- 106 A. C. Diebold, J. Canterbury, W. Chism, C. Richter, N. Nguyen, J. Ehrstein, and C. Weintraub, Mater. Sci. Semicon. Proces. **4**, 3-8 (2001).

- <sup>107</sup> H. G. Tompkins and W. A. McGahan, *Spectroscopic Ellipsometry and Reflectometry : A User's Guide* (Wiley, New York, 1999).
- <sup>108</sup> Y. Z. Hu and S. P. Tay, J. Vac. Sci. Technol. B **19**, 1706-1714 (2001).
- <sup>109</sup> W. Kern, *Handbook of Semiconductor Wafer Cleaning Technology* (Park Ridge, New Jersey, Park Ridge, New Jersey, USA, 1993).
- <sup>110</sup> D. E. Aspnes, Thin Solid Films **89**, 249-262 (1982).
- <sup>111</sup> J. P. Riviere, S. Harel, P. Guerin, and A. Straboni, Surf. Coat. Technol. **84**, 470-475 (1996).
- <sup>112</sup> C. M. Herzinger, B. Johs, W. A. McGahan, J. A. Woollam, and W. Paulson, J. Appl. Phys. **83**, 3323-3336 (1998).
- <sup>113</sup> J.A. Woollam Co., Inc., *Guide to Using WVASE*.
- <sup>114</sup> H. Nohira, W. Tsai, W. Besling, E. Young, J. Petry, T. Conard, W. Vandervorst, S. De Gendt, M. Heyns, J. Maes, and M. Tuominen, J. Non-Cryst. Solids **303**, 83-87 (2002).
- <sup>115</sup> G. E. Jellison and F. A. Modine, Appl. Phys. Lett. **69**, 371-373 (1996).
- <sup>116</sup> G. E. Jellison, V. I. Merkulov, A. A. Puretzky, D. B. Geohegan, G. Eres, D. H. Lowndes, and J. B. Caughman, Thin Solid Films **377**, 68-73 (2000).
- <sup>117</sup> B. von Blanckenhagen, D. Tonova, and J. Ullmann, Appl. Optics **41**, 3137-3141 (2002).
- <sup>118</sup> Y. J. Cho, N. V. Nguyen, C. A. Richter, J. R. Ehrstein, B. H. Lee, and J. C. Lee, Appl. Phys. Lett. **80**, 1249-1251 (2002).
- <sup>119</sup> D. E. Aspnes, "The Accurate Determination of Optical Properties by Ellipsometry," in *Handbook of Optical Constants of Solids; Vol. 1*, edited by E. D. Palik ( Academic Press, Orlando, 1985), p. 89-112.
- <sup>120</sup> E. D. Palik, *Handbook of Optical Constants of Solids* (Academic Press, Orlando, FL, 1985-1998).
- <sup>121</sup> L. Manchanda, M. D. Morris, M. L. Green, R. B. van Dover, F. Klemens, T. W. Sorsch, P. J. Silverman, G. Wilk, B. Busch, and S. Aravamudhan, Microelectron. Eng. **59**, 351-359 (2001).
- <sup>122</sup> D. H. Kuo and C. H. Chien, Thin Solid Films **429**, 40-45 (2003).
- <sup>123</sup> K. Goedicke, J.-S. Liebig, O. Zywicki, and H. Sahm, Thin Solid Films **377-378**, 37-42 (2000).

- <sup>124</sup> W. K. Chim, T. H. Ng, B. H. Koh, W. K. Choi, J. X. Zheng, C. H. Tung, and A. Y. Du, *J. Appl. Phys.* **93**, 4788-4793 (2003).
- <sup>125</sup> S. Chatterjee, S. K. Samanta, H. D. Banerjee, and C. K. Maiti, *Bull. Mat. Sci.* **24**, 579-582 (2001).
- <sup>126</sup> T. Go, N. Hara, and K. Sugimoto, *J. Jpn. Inst. Met.* **57**, 1041-1046 (1993).
- <sup>127</sup> R. C. Garvie, *J. Phys. Chem.* **82**, 218-224 (1978).
- <sup>128</sup> J.A. Woollam Co., Inc., *Easy-to-Use Acquisition/Analysis Software for Spectroscopic Ellipsometry (EASE<sup>TM</sup>) Manual* (Software Manual published by J.A. Woollam Co., Inc.).
- <sup>129</sup> B. Johs, J. Hale, N. J. Ianno, C. M. Herzinger, T. Tiwald, and J. A. Woollam, "Recent Developments in Spectroscopic Ellipsometry for in situ Applications," in *Proc. SPIE; Vol. 4449*, edited by SPIE (The Society of Photo-Optical Instrumentation Engineers, Bellingham, Washington, 2001), p. 41-57.
- <sup>130</sup> Y. Z. Hu, D. J. Diehl, Q. Liu, C. Y. Zhao, and E. A. Irene, *Appl. Phys. Lett.* **66**, 700-702 (1995).
- <sup>131</sup> R. W. Collins and B. Y. Yang, *J. Vac. Sci. Technol. B* **7**, 1155-1164 (1989).
- <sup>132</sup> Z. Song, L. M. Sullivan, and B. R. Rogers, *J. Vac. Sci. Technol. A* **23**, 165-176 (2005).
- <sup>133</sup> D. E. Aspnes, *J. Vac. Sci. Technol.* **18**, 289-295 (1981).
- <sup>134</sup> R. D. Geil, B. R. Rogers, Z. Song, and R. A. Weller, *J. Vac. Sci. Technol. A* **22**, 1129-1133 (2004).
- <sup>135</sup> R. A. Weller, "General purpose computational tools for simulation and analysis of medium energy backscattering spectra," in *Application of Accelerators in Research and Industry : Proceedings of the Fifteenth International Conference, Denton, Texas, November 1998; Vol. 1*, edited by J. L. Duggan and I. L. Morgan (American Institute of Physics, Woodbury, N.Y., 1999), p. 596-599.
- <sup>136</sup> W.-K. Chu, J. W. Mayer, and M.-A. Nicolet, *Backscattering Spectrometry* (Academic Press, New York, 1978).
- <sup>137</sup> A. K. Livesey and G. C. Smith, *J. Electron Spectrosc. Relat. Phenom.* **67**, 439-461 (1994).
- <sup>138</sup> <http://www.webelements.com>.
- <sup>139</sup> Z. Song, B. R. Rogers, and N. D. Theodore, *J. Vac. Sci. Technol. A* **22**, 711-718 (2004).

- <sup>140</sup> N. V. Edwards, in *Status and Prospects For VUV Ellipsometry (Applied to High K and Low K Materials)*, Austin, Texas, March 24-28, 2003 (American Institute of Physics), p. 723.
- <sup>141</sup> "Front End Process," in *International Technology Roadmap for Semiconductors (2004 Update)*, 2004 ed. (International SEMATECH, Austin, TX, 2004).
- <sup>142</sup> H. S. P. Wong, IBM J. Res. Dev. **46**, 133-168 (2002).